Politecnico di Torino

Politecnico di Torino

Laurea Magistrale in Ingegneria Matematica

Sessione di Laurea Marzo 2026

ANALYSIS OF THE PROPELLER WAKE OF VSP IN RESTRICTED FLOW FIELDS

Propeller-induced hydrodynamic loads and detailed analysis of scale effects

Relatori:
Luca Bruno
Jannes Berndt

Candidati:
Rachele Valcalda

Abstract

The Voith-Schneider propeller is a widely adopted cycloidal propulsion system made of four to six blades that rotate around the vertical axis of their circular support and around their own vertical axis at the same time. Its operational mechanism makes it particularly fitted for vessels that require high maneuverability at low speeds, such as ferries and tugboats. Numerous investigations analyze the parameters that directly involve the efficiency of the propeller; however, very little is found regarding its potential erosive effect on the harbour structures and seafloors. This thesis addresses this problem by analyzing the impact of a VSP that operates first in the open sea and later in a confined environment. Two existing ferry geometries equipped with VSPs are examined using an Improved Delayed Detached Eddy Simulation (IDDES) turbulence model combined with an overlapping grid technique, used to reproduce the propeller rotation relative to the ferries' hull. The simulations are run using the Froude similarity, which ensures consistency for the hydrodynamic phenomena dominated by gravity. Different wall and seabed clearances are considered, in addition to the open-sea reference case. The different propeller wakes obtained are compared, considering, in particular, the velocity field, the pressure on the quay wall and the shear stress on the seabed. From the analysis, the distance from the quay wall appears to be the parameter that influences the erosion the most, and moving the vertical wall away results in a significant decrease of the load on that wall, as well as a reduction of the seafloor scour. An in-depth analysis of the frequencies detected below the propeller and in its wake is also carried out, for both restricted and unrestricted cases. Finally, the implications of using scaled geometries under a Froude similarity are discussed, in particular regarding frictional forces. Two seabed roughness coefficients are tested in full-scale simulations. However, neither of them provides a satisfying match with the model scale results.

Acknowledgements

First of all, I would like to acknowledge the support of Voith for granting access to the VSP data and the hull geometries used in this thesis.
I am sincerely grateful to Jannes not only for the invaluable help and guidance he provided throughout the development of this thesis, but also for being a point of reference during my stay in Hamburg. His availability and encouragement made this experience both enjoyable and extremely formative.
Lastly, I would like to thank Professor Bruno for the opportunity to work on this project and for his valuable and useful advice.

Contents

List of Tables

List of Figures

Chapter 1

Introduction

1.1 Historical background: screw propellers

The first evidence of the concept of a screw used to move water dates back to the 7th century B.C. in an Assyrian text and was later confirmed by the Greek author Strabo when he described the Hanging Gardens [1]. Conventionally, however, the origin of the screw propeller traces back to Archimedes' screw, used to lift water for irrigation; yet for over a millennium, no significant improvements were made. In 1681, Robert Hooke modified a horizontal watermill into a four-blade screw propeller that he used to measure water currents, acknowledging the potential that it had to move boats if properly powered. In 1752, Daniel Bernoulli won one of the prizes the *Académie des Sciences* in Paris offered for theoretical studies that could lead to significant developments in naval architecture, designing a propeller wheel that used inclined planes. However, a major debate persisted regarding the best configuration for marine propellers, and a few years later Paucton suggested using Archimedes' screw to propel ships. In 1785, Joseph Bramah patented a vertical wheel with inclined blades attached to the stern, intended to move a ship forward and backward, although he never tested it. The following decades were characterized by some actual physical attempts that gradually led to a large development of marine propeller technology. For example, Edward Shorter applied a variation of Bramah's patent to the ship *Doncaster* in 1802, achieving a velocity of 2.4 km/h. In 1832, the Canadian John Patch built and successfully tested a wooden shaft with two fans at the end, and two years later, Captain Robert Kelley adopted the propeller for his vessel. On a trip, while other traditional boats could not move when the wind stopped, Kelley's one kept going. The year of the breakthrough in naval architecture is 1836, when both Francis Pettit Smith and John Ericsson took out two separate patents for their screw propellers, marking a huge progress in water navigation, transforming the experiments of the previous centuries into practical applications. Ericsson was a Swedish engineer living in London, and his propeller consisted of two underwater cylinders rotating at different speeds in opposite directions, equipped with short inclined plates (Figure 1.1a). After successful model tests, he built a 14-meter ship named *Francis B. Ogden* and tried his propulsion system on the Thames. Despite reaching the velocity of 16 km/h, his invention was not considered to be innovative, so Ericsson left for the USA, where he designed the Navy's first screw-propelled vessel, the *Princeton*. Smith was an English farmer and his invention consisted of an Archimedean screw with two full turns, but placed differently from the Swedish engineer, and he tested it in his farm pond (Figure 1.1b). He later demonstrated it on the Paddington Canal on a ship named after him; however, the vessel had an accident and half of the propeller broke. Smith discovered that this accidental alteration had increased the speed and accordingly he set up the propeller to only have

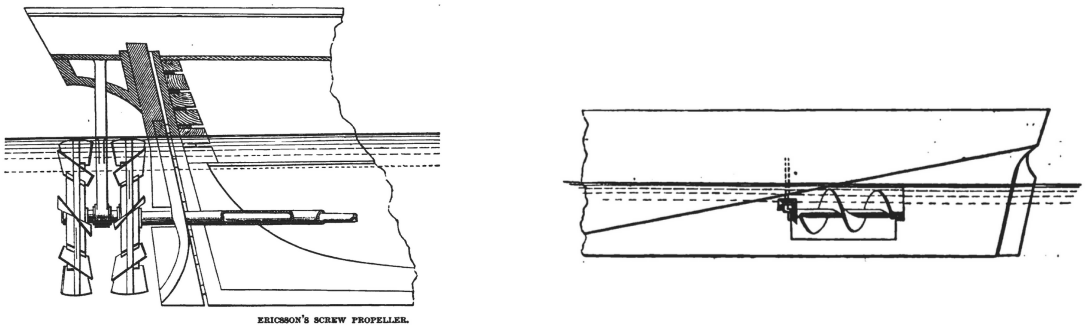

(a) Ericsson's propeller **(b)** Smith's propeller

Figure 1.1: Early screw propeller designs: Smith's (a) and Ericsson's (a) propellers [2].

one turn. It was the British Navy on this occasion that got interested in using a screw propeller, and in 1839 a larger ship called *Archimedes* was laid down; a year later, it circumnavigated Great Britain [3][4][5]. When it arrived in Bristol, this new discovery amazed Isambard Kingdom Brunel and made him change the propulsion system of his iron-made ship *Great Britain*, replacing the paddle wheels with screw propellers. The adoption of this system made *Great Britain* the first screw-propelled steamship to cross the Atlantic Ocean [6]. In the following years, the screw propellers were optimized and, along with them, new types of marine propulsion were developed, such as the Voith-Schneider propellers, whose history is explained in detail in Section 1.3.

1.2 Types of marine propellers

Different types of propellers were developed to meet each ship's specific need and purpose. The Fixed Pitch Propeller (FPP) in Figure 1.2a has a fixed blade angle, and the thrust generated by the rotation is aligned with the longitudinal axis of the ship. This type of propeller is robust and reliable, and has low maintenance costs. For these reasons, it is used mainly on conventional trading vessels, where manoeuvrability is not a primary requirement since, for this type of propeller, only the rotational speed and its direction can be controlled. A more versatile evolution of the FPP is the Controllable Pitch Propeller (CPP), in which the blade angle can be adjusted for different loads and speeds (Figure 1.2b), hence the engine can maintain its most efficient rotational regime while increasing or reducing the thrust, or even changing its direction. The greater manoeuvrability of CCPs, though, comes with higher costs and they require more maintenance. The Azimuth Thruster (Figure 1.3a) can rotate around the vertical axis (in some cases, a full revolution is possible), making the boat more manoeuverable and the rudder unnecessary. It is usually installed on small vessels and special-purpose ships such as tugs, ferries, cruise ships or offshore supply vessels, and can be either non-ducted or ducted. In general, for ducted propellers, the thrust is generated more efficiently and the losses caused by water being pushed away from the expected path are reduced: in these cases (Figure 1.3b), the blades are specifically designed to take into account the duct and its influence on the wake. However, for this kind of propeller, the performance decreases if the ship velocity grows, limiting their adoption only to slow, powerful boats. A particular type of ducted propeller, used especially in shallow water, is the Pump Jet thruster. Its quietness made it highly valued for military operations, where it is mainly employed. In some cases, two propellers are assembled in line on a single shaft, rotating in opposite directions (Figure 1.4a). For this reason, this configuration is called Contra Rotating Propeller (CRP); the second propeller neutralizes the torque generated by

(a) Fixed Pitch Propeller [7]

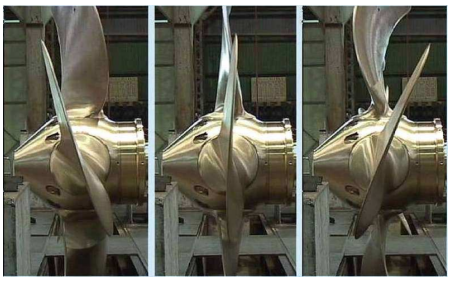

(b) Controllable Pitch Propeller with different blade pitch angles [8]

Figure 1.2: Examples of (a) a FPP and (b) a CPP.

(a) Azimuth Thruster [9]

(b) Ducted Propeller [10]

Figure 1.3: Examples of (a) an azimuth thruster and (b) a ducted propeller.

a single propeller and recovers part of the rotational energy that would otherwise be lost in the wake. Instead of conventional propellers, high-speed ships use Water Jet Propulsion, shown in Figure 1.4b: in this type of propulsion system, seawater is collected through a hole in the hull and directed to an adjustable nozzle, where it is accelerated. Unlike traditional propellers, Water Jets do not have cavitation problems and maintain high performance even at high speeds, generating less vibration and noise. The water flow trajectory can also be adjusted, even reversed, making the system very flexible. At the same time, though, they are heavier and more voluminous, limiting their use to certain types of vessels.

1.2.1 Cycloidal Propellers

In cycloidal propellers (Fig. 1.5), four to six blades attached to a circular support rotate around a vertical axis under the hull. Each blade performs two types of rotation, coordinated by the gear system inside the propeller: a main rotation, around the vertical axis passing through the center of the propeller, with an angular velocity equals to the propeller's rotation rate, and a pitch rotation, related to the pitch angle, where the blade rotates around its own vertical axis [14]. To a

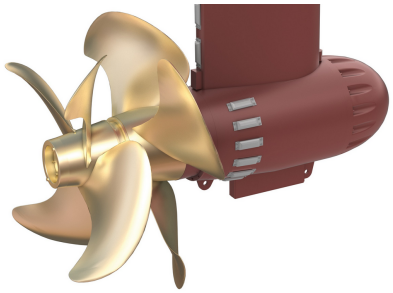

(a) Contra Rotating Propeller [11]

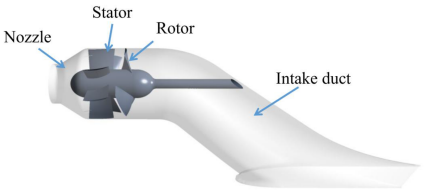

(b) Water Jet Propulsion [12]

Figure 1.4: Examples of (a) a CRP and (b) a Water Jet.

Figure 1.5: Two cycloidal propellers [13].

stationary observer, the blade's path traces a cycloid curve (hence the name of the propeller). Due to the rotation of the propeller, the inflow velocity changes continuously, producing an unsteady flow; therefore, the thrust of each blade is a function of the time. Despite being less efficient than a normal propeller [9], this type of propulsion makes the ships that use it highly maneuverable, allowing rapid changes in thrust magnitude and in every direction without changing the main rotation speed. The value of eccentricity e classifies them into three categories: trochoidal (e>1), which has a high hydrodynamic efficiency and can work at high-speed, true cycloidal (e=1) and epicycloidal (e<1), [15] [16]. The low-speed maneuvering requirements in harbors, though, led to a major development of epicycloidal propellers [17]. The Voith-Schneider propellers fall into this category.

1.3 Voith-Schneider Propeller

The Voith-Schneider propellers are a low-pitch cycloidal propeller derived from the modification of the Austrian engineer Ernst Leo Schneider (1894–1975) to the fixed low-pitch aircraft propeller, originally developed by Kurt Kirsten [18]. Following a fortunate encounter with a Voith engineer, during which he had the opportunity to explain the working principle of the propeller, he was granted financial support from the company, and in 1926 he registered the patent [19]. After working in St. Pölten and Heidenheim, he successfully tested the propeller in Rotterdam, on a boat called *Torqueo*, and at the beginning of the 1930s the propeller was working on a ferry in Lake Constance [20]. Schneider's idea came after reading an article regarding the motion of marine swimmers. Figure 1.6 shows the similarities between the two movements: for eccentricity e > 1, the trajectories would be the same. The VSP differs from the other cycloidal propellers because

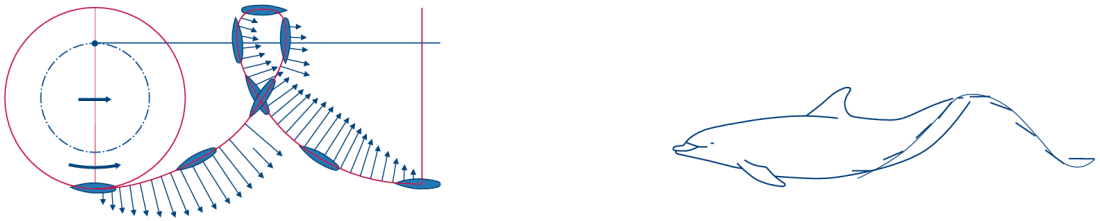

(a) Path of a VSP [21] **(b)** Dolphin motion [21]

Figure 1.6: Similarities between (a) a VSP path and (b) the movement of a dolphin's tail.

it uses a rod-crank mechanism (Fig .1.7), and due to its functioning mode, it was nicknamed *eggbeater* in the 1950s [22]. The VSPs may fit different boats, such as tugs, double-ended ferries,

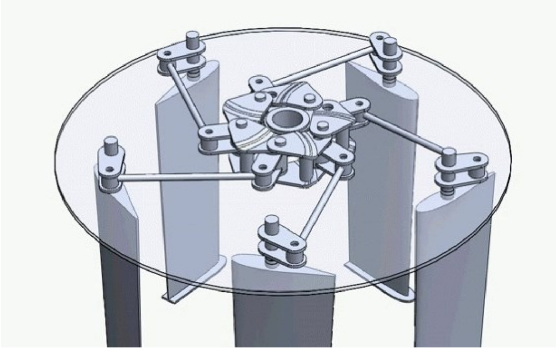

Figure 1.7: Rod-crank mechanism of a VSP [23].

fire-fighting boats, offshore support vessels, water tractors and mine countermeasures vessels [24]. For this reason, each VSP might differ in the number of blades and orbit diameter (varying from 1.2 to 3.6 meters), and the maximum propeller input power can reach up to 3900 kW [25]. A VSP usually works at low rotational speed, which is the reason why they do not require frequent maintenance and can live a long life [24]. Figure 1.8 shows the components inside a VSP: the rotor casing is upheld by a thrust plate and centered by a roller bearing, while the blade shafts are supported by gland bearings; all the pieces are lubricated by the flanged-on oil pump. The rotor casing receives the power through the reduction and bevel gears, and it is responsible for the rotation around the vertical axis of the propeller. The steering, on the contrary, is transmitted to the blades by the control rod (which can vary the magnitude and direction of the thrust) and by the two servomotors: the *propulsion* one is responsible for the longitudinal thrust, while the *rudder* one for the transverse thrust. Consequently, it is possible to change the speed of the propeller while varying its angle of propulsion by 360 degrees [21]. Usually, the ships equipped with VSPs are powered by diesel engines. The rapid adaptation of the propeller to diverse loads makes it possible to best use this type of motor also under different weights [26]. As already stated in Section 1.2.1, each blade draws a cycloid; during a complete revolution, the propeller moves of $\lambda D\pi$ (Fig. 1.10a), where D is the diameter of the propeller and $\lambda = \dfrac{V_A}{u}$, with V_A the advance velocity, u the circumferential velocity $u = \pi Dn = \omega R$ and n the rotational speed of the propeller [24]. The product $\lambda\dfrac{D}{2}$ is called rolling radius of the cycloid. The biggest advantage of

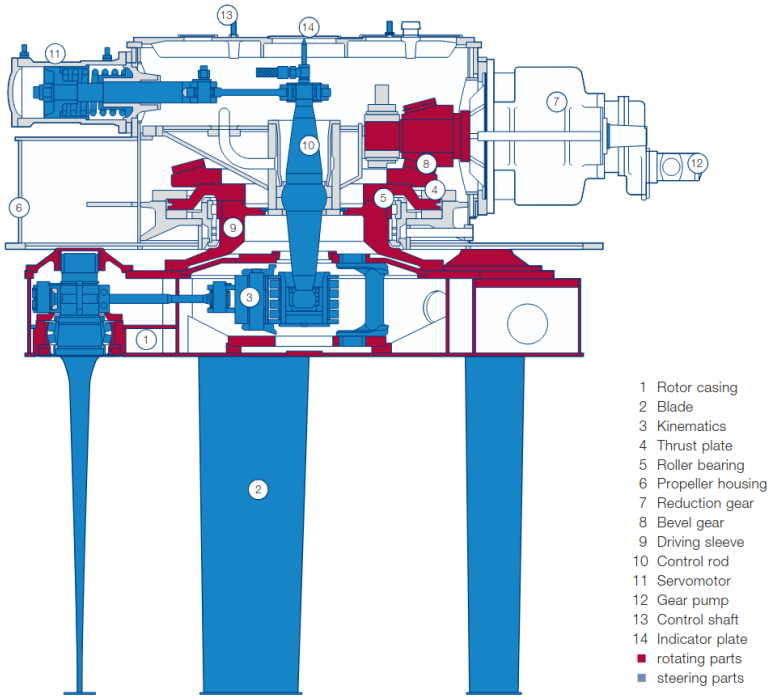

Figure 1.8: Longitudinal section of a and its components [21].

the VSP is that its thrust can vary in magnitude and direction without changing the propeller direction or speed [26][27]. To do so, it is simply necessary to change the steering center of the propeller. In Figure 1.9, it is shown how the different positions of the steering center N', the point where the perpendicular of the chord's profiles intersects, impact the direction and magnitude of the thrust. When $N' \equiv O$, no thrust is generated. Figure 1.10b shows how the

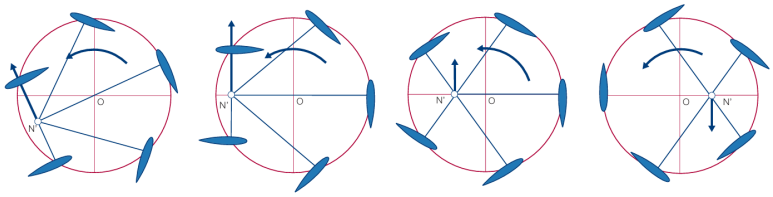

Figure 1.9: Impact that the position of the steering center N' has on the thrust [21].

thrust is generated, taking into account only two blades: when the steering center is moved from N to N' and the angle of attack α is created, two forces are generated, the hydrodynamic lift A and the drag force W, which together form the resulting force R. The components perpendicular to the direction of the thrust cancel each other, so only the ones acting along the thrust direction are left, and thus they sum up. By varying α, which means changing the steering center N', a thrust can be generated in any direction [24][21][26]. For a certain rotation angle θ, the thrust T

(a) Blade path **(b)** Forces on the blades

Figure 1.10: Path of the cycloid considering only one blade (a) and forces on the blades (b) [21].

and torque Q can be calculated as the sum of T and Q in every blade for that θ:

$$T(\theta) = \sum_{i=1}^{N} T_i(\theta), \qquad Q(\theta) = \sum_{i=1}^{N} Q_i(\theta) \tag{1.1}$$

where N is the number of blades and Q is given by the sum of the torque of the propeller rotation and the blade rotation around its axis. To obtain the average T and Q, Eq.1.1 are averaged and calculated over each revolution:

$$T_{average} = \frac{\int_0^{2\pi} T(\theta)d\theta}{\int_0^{2\pi} d\theta}, \qquad Q_{average} = \frac{\int_0^{2\pi} Q(\theta)d\theta}{\int_0^{2\pi} d\theta} \tag{1.2}$$

From these values, it is possible to calculate the thrust and torque coefficient:

$$k_T = \frac{T_{average}}{\frac{1}{2}\rho L D u^2} \qquad k_Q = \frac{2Q_{average}}{\frac{1}{2}\rho L D^2 u^2} \tag{1.3}$$

where ρ is the water density, L is the blade length, D is the diameter of the VSP and u is the circumferential velocity. The open water efficiency of a VSP η_0 is defined as the ratio of the propulsion power Tv_a and the delivered power $Q\omega$:

$$\eta_0 = \frac{Tv_a}{Q\omega} = \frac{v_a k_T}{\frac{1}{2} D\omega k_Q} = \lambda \frac{k_T}{k_Q} \tag{1.4}$$

There are numerous parameters that influence the efficiency of a VSP and they can be studied to optimize it. Some of them can be modified, such as the angle of attack or the position of the blades, while others are imposed by the design of the propeller, for example the thickness of the blades and their geometry, or the rotor's diameter [24].

1.4 State of art and purpose of this work

Numerous investigations have been made regarding the scour on the seabed produced by traditional propellers in constrained conditions, studying, for example, the influence of the characteristics of the propeller [28] or the quay wall clearance [29][30]. Some empirical formulas were also proposed to predict the propeller-induced erosion, for both restricted and unrestricted cases [31][32]. However, while numerous articles discuss the functioning of a VSP and study the influence of each parameter on the efficiency of the propeller, very little is found regarding the

loads that this type of propeller causes on the harbor structures and seafloors. In a Dutch report from 1982 [33], a comparison was made between a single-deck ferry equipped with two traditional screw propellers and a double-deck ferry with two VSPs. The article states that the VSPs cause less erosion compared to the traditional propellers in normal conditions: the maximum velocity at the seabed for a screw propeller is calculated to be up to 3.0 m/s, while for a VSP it is around 0.6 m/s and reaches 2 m/s only at a depth of 2 m. The current guidelines given by PIANC [9] calculate the outflow velocity of a VSP as an empirical relationship function of the propeller geometry and power, while the formula for the flow distribution is found using the one for the thruster propeller, in which the wall clearance is the main variable.
In this Master's thesis, a further analysis of the loads produced by VSPs in restricted conditions on quay walls and seabeds is carried out, considering two different ferries. In Chapter 2.2, a detailed explanation of the finite volume method is provided, along with the derivation of the main equations. In Chapter 3, the imported geometries are described and the set-up of the simulations is explained, in addition to an analysis of the Froude similarities. In Chapter 4, the results show how the distance from the boundaries influences the velocity distribution, as well as the values of pressure and shear stress on the walls. Moreover, a comparison between a scaled model and a full scale simulation is made, changing the roughness height of the seabed. Finally, a summary of the work is given in Chapter 5, along with some recommendations for further investigations.

Chapter 2

Methodology

2.1 Finite volume method

The finite volume method (FVM) is a numerical approach used to approximate solutions of partial differential equations that describe conservation laws. It achieves this by reformulating those equations into a set of algebraic expressions and applying them to small and finite volumes. First, the geometry of the domain is divided into distinct, non-overlapping control volumes; then, each governing equation is integrated over an individual control volume, and subsequently converted into an algebraic equation, whose resolution provides the values of the unknown variables for each volume. Some terms of the equations become face fluxes and, since the flux that leaves a volume is the same that enters into the neighbor volume, this method is conservative.
As an example to explain this method, the general transport equation is chosen, since all conservation equations can be traced back to it:

$$\frac{d}{dt}\int_V \rho\phi dV + \int_A \rho\mathbf{v}\phi \cdot d\mathbf{a} = \int_A \Gamma\nabla\phi d\mathbf{a} + \int_V S_\phi dV \tag{2.1}$$

where V is a control volume and A its area, ϕ is a scalar quantity, $d\mathbf{a}$ is the surface vector, ρ is the density of the fluid and $\mathbf{v}$ its velocity, $\nabla\phi$ is the gradient of the scalar quantity, Γ is the diffusion coefficient and S_ϕ the volumetric source term. The term $\frac{d}{dt}\int_V \rho\phi dV$ is the *transient term*, which represents the change of ϕ over time inside V, $\int_A \rho\mathbf{v}\phi \cdot d\mathbf{a}$ is the *convective flux*, that is the transport of ϕ due to convection, $\int_A \Gamma\nabla\phi d\mathbf{a}$ is ϕ net rate due to diffusion, called *diffusive flux*, and $\int_V S_\phi dV$ is the *source term*.

Source term

The surface integrals can be expressed, using the second-order midpoint rule, as the values of the variable at the corresponding location on the element face:

$$\int_A \mathbf{J}^\phi \cdot d\mathbf{a} \approx \sum_f \mathbf{J}_f^\phi \cdot \mathbf{a}_f \tag{2.2}$$

where $\mathbf{J}^{\phi}$ is the convective or diffusive flux, and the subscript f is adopted to indicate the quantities with respect to the face of the cell. Meanwhile, the source term, that is a volume integral, can be rewritten as the product of the source mean value and the volume of the cell:

$$\int_V S_\phi dV \approx S_{\phi_0} V_0 \tag{2.3}$$

S_{ϕ_0} is the mean value of the source term calculated at the center of the cell and V_0 is the volume of the cell. Eq. 2.1 becomes:

$$\frac{d}{dt}(\rho\phi V)_0 + \sum_f [\rho\phi(\mathbf{v}\cdot\mathbf{a})]_f = \sum_f (\Gamma\nabla\phi\cdot\mathbf{a})_f + (S_\phi V)_0 \tag{2.4}$$

where the subscript 0 means that the quantity is evaluated for the volume of the cell while f is for the quantity on the face cell.

Convective term

The terms of the equation can be discretized. Starting from the convective term, it can be rewritten using the mass flow at the face $\dot{m}_f$:

$$(\rho\phi\mathbf{v}\cdot\mathbf{a})_f = (\dot{m}\phi)_f = \dot{m}_f\phi_f \tag{2.5}$$

To compute the product $\dot{m}_f\phi_f$, the value of the property ϕ at the face is calculated by interpolating the cell-center values. Many interpolation methods are available, and some are explained below.

- **Central differencing scheme (CDS)**
  This scheme calculates the value in the center of the cell face using a linear interpolation, providing a second-order accuracy. The convective flux becomes:

  $$(\dot{m}\phi)_f = \dot{m}_f[f\phi_0 + (1-f)\phi_1] \tag{2.6}$$

  where f is the interpolation factor calculated as $f = \dfrac{V_1}{V_0 + V_1}$, where the subscript 0 refers to the starting cell, and the subscript 1 refers to the adjacent cell. Despite being simple and second-order accurate, this scheme, in some cases (especially for high Reynolds and Péclet numbers), produces dispersive error.

- **First-order upwind (FOU)**
  The cell face center value of ϕ_f depends on the mass flow direction, and it is calculated as:

  $$(\dot{m}\phi)_f = \begin{cases} \dot{m}_f\phi_0 & \text{for } \dot{m}_f \geq 0 \\ \dot{m}_f\phi_1 & \text{for } \dot{m}_f < 0 \end{cases} \tag{2.7}$$

  This is a first-order accuracy scheme and it requires a very fine grid to avoid numerical diffusion; however, it is an unconditionally stable scheme.

- **Second-order upwind (SOU)**
  A more precise version of the previous scheme is the second-order upwind scheme, which takes the accuracy from first to second order. In comparison with the FOU, in the SOU the face values of the property are calculated for each side, $\phi_{f,0}$ and $\phi_{f,1}$, as: where $\mathbf{s}_i = \mathbf{x}_f - \mathbf{x}_i$, $i = 0{,}1$ and $(\nabla\phi)_{r,i} = \alpha\nabla\phi$, with α as the scaled factor. Therefore, the scheme is written as:

  $$(\dot{m}\phi)_f = \begin{cases} \dot{m}_f\phi_{f,0} & \text{for } \dot{m}_f \geq 0 \\ \dot{m}_f\phi_{f,1} & \text{for } \dot{m}_f < 0 \end{cases} \tag{2.8}$$

Diffusive term

For the diffusive flux $D_f = (\Gamma \nabla\phi \cdot \mathbf{a})_f$, the face gradient of the property $\nabla\phi_f$ is expressed as:

$$\nabla\phi_f = (\phi_1 - \phi_0)\boldsymbol{\alpha} + \overline{\nabla\phi} - (\overline{\nabla\phi} \cdot \mathbf{ds})\boldsymbol{\alpha} \tag{2.9}$$

where $\boldsymbol{\alpha} = \dfrac{\mathbf{a}}{\mathbf{a} \cdot \mathbf{ds}}$, $\mathbf{ds} = \mathbf{x}_1 - \mathbf{x}_0$, and $\overline{\nabla\phi} = \dfrac{(\nabla\phi_0 + \nabla\phi_1)}{2}$. The diffusive flux thus becomes:

$$D_f = \Gamma_f[(\phi_1 - \phi_0)\boldsymbol{\alpha} \cdot \mathbf{a} + \overline{\nabla\phi} \cdot \mathbf{a} - (\overline{\nabla\phi} \cdot \mathbf{ds})\boldsymbol{\alpha} \cdot \mathbf{a}] \tag{2.10}$$

Transient term

For unsteady flows, the integration in time is also needed, and the total time is divided into time-steps. To progress in the resolution of the equations, the solution of the previous time step is necessary; therefore, time-stepping schemes are employed for this purpose. These time schemes are divided into explicit and implicit methods: the explicit ones are simpler and have a lower computational cost at every time step, but they need a small time step for stability reasons; the implicit ones are unconditionally stable and can tolerate longer time steps, but they require the solution of a system of equations for every time step, meaning a higher computational cost. In the following simulations, a second-order implicit scheme is used; in particular, the backward differentiation formula (BDF2) is used:

$$f(t_{n+1}, y_{n+1}) = \frac{3y_{n+1} - 4y_n + y_{n-1}}{2\Delta t} \tag{2.11}$$

where Δt is the time step size, $n+1$ is the current time level and n and $n-1$ are the previous ones.

2.1.1 Segregated flow

The discretization method discussed above can be applied to the expressions in the form of transport equations. However, the pressure, which appears in the source term, does not fit in this form and it requires a different approach.
For the case of compressible fluids, the problem is bypassed using the density as a dependent variable, so that the pressure can be determined through the equation of state. For incompressible flow, however, this mechanism is not applicable, and other alternatives are explored. One option is given by the segregated flow solvers, which calculate the equations for the pressure and the velocity separately. In comparison to coupled solvers, where the equations are solved simultaneously, they require less memory and are easier to implement; however, their convergence is slower and can become unstable for some applications, such as highly compressible fluids or a high Mach number. In this solver, a pressure-velocity coupling algorithm uses a pressure-correction equation, obtained from the momentum and continuity equations. This relationship returns a pressure value that is used to correct the velocity, making it fulfill the continuity equation. For this algorithm, the continuity equation is in the form:

$$\sum_f \dot{m}_f = \sum_f (\dot{m}_f^* + \dot{m}_f') = 0 \tag{2.12}$$

where $\dot{m}_f'$ is the mass flow correction and $\dot{m}_f^*$ is the uncorrected face mass flux, calculated as:

$$\dot{m}_f^* = \rho_f \mathbf{a} \cdot \left(\frac{\mathbf{v}_0^* + \mathbf{v}_1^*}{2}\right) - \Upsilon_f \tag{2.13}$$

where ρ_f is the density at the face, $\mathbf{a}$ is the surface area vector, $\mathbf{v}_0^*$ and $\mathbf{v}_1^*$ are the cell velocities after the discrete momentum equations have been solved, and Υ_f is an artificial numerical damping that prevents the numerical instability. The discrete pressure-correction equation becomes:

$$p'_p + \sum_n a_n p'_n = r \tag{2.14}$$

where p'_i $i = p, n$ is the pressure correction at the cell p and at its neighbour cell n, a_n is the momentum coefficient for cell n and r is the residual calculated as $r = \sum_n \dot{m}_f^*$. In this study, the SIMPLE algorithm is used: it is an iterative method that hypothesizes an initial pressure field (usually from the last time step), solves the momentum and continuity equations and finds an approximated velocity $\mathbf{v}^*$; a mass imbalance $\dot{m}_f^*$ is produced due to the velocity not being the exact solution of the continuity equation, and that quantity is used to solve the pressure-correction equation. The corrected pressure returns a new value of the velocity: if the velocity does not satisfy the momentum equation, the procedure is repeated till it does. A detailed explanation of the steps can be found in Section 3.5.1.

In this section, the following sources were studied: [34][35][36].

2.2 Derivation of model equations

The study of a fluid can be conducted in different ways: the Eulerian description studies what happens in fixed point of the domain, the Lagrangian one follows the single particles, while other types of approaches focus on a bigger portion of the fluid. For the latter, in particular, two types of descriptions are possible: in closed systems, a quantity of matter remains constant, its boundaries can be fixed or change in time, but no mass can cross them; in control volumes, a portion of space is defined, and mass can cross it, boundaries can be fixed or moving. To switch from one description to another, the Reynolds transport theorem (RTT) is used: given an extensive property B and the corresponding intensive property b, such that $B = \int_V \rho b dV$, where ρ is the density of the fluid and dV is an infinitive volume, the theorem states that the rate of change of an extensive property for the closed system is equal to the time rate of change of that property within the control volume CV plus the net rate of flux of the property through the control surface CS:

$$\frac{dB_{sys}}{dt} = \int_{CV} \frac{\partial}{\partial t}(\rho b) dV + \int_{CS} \rho b \mathbf{u} \cdot \mathbf{n} dA \tag{2.15}$$

where t is the time, $\mathbf{u}$ is the velocity vector, dA is the infinitive area and $\mathbf{n}$ is its unit outward normal vector. The derivative over time of the mass in the closed system M is 0 by definition. Choosing M as B, it follows that $b = 1$, so for the RTT:

$$\frac{dM}{dt} = \int_{CV} \frac{\partial \rho}{\partial t} dV + \int_{CS} \rho \mathbf{u} \cdot \mathbf{n} dA = 0 \tag{2.16}$$

For the divergence theorem:

$$0 = \int_{CV} \frac{\partial \rho}{\partial t} dV + \int_{CS} \rho \mathbf{u} \cdot \mathbf{n} dA = \int_{CV} \frac{\partial \rho}{\partial t} dV + \int_{CV} \nabla \cdot (\rho \mathbf{u}) dV = \int_{CV} \left(\frac{\partial \rho}{\partial t} + \nabla \cdot (\rho \mathbf{u}) \right) dV \tag{2.17}$$

The CV is arbitrary, so:

$$\frac{\partial \rho}{\partial t} + \nabla \cdot (\rho \mathbf{u}) = 0 \tag{2.18}$$

If the fluid considered is incompressible, then:

$$\nabla \cdot \mathbf{u} = 0 \tag{2.19}$$

Eq. 2.19 is called continuity equation.
If the momentum $\mathbf{Q} = \int \rho \mathbf{u} dV$ is taken as the extensive property, $b = \mathbf{u}$, and the momentum equation is obtained:

$$\frac{d\mathbf{Q}}{dt} = \int_{CV} \frac{\partial}{\partial t}(\rho \mathbf{u}) dV + \int_{CS} (\rho \mathbf{u}) \mathbf{u} \cdot \mathbf{n} dA \tag{2.20}$$

A generic body is affected by two types of forces: body forces, acting throughout the entire body, and surface forces, acting on its surface. The fluid studied in this analysis (water) is considered continuous, viscous, Newtonian and incompressible; it has mass m, volume V and density ρ. To study its behaviour, a certain control volume is chosen, and it is assumed that the only body force acting is its weight, so:

$$d\mathbf{F}_b = dm\mathbf{g} \tag{2.21}$$

where $\mathbf{g}$ is the acceleration of gravity. The total body forces acting on the element are:

$$\sum \mathbf{F}_b = m\mathbf{g} = \int_{CV} \rho \mathbf{g} dV \tag{2.22}$$

Surface forces are the result of the interaction of the element with the nearby body parts, acting on its area A. These forces $\mathbf{F}_s$ can be decomposed into three components, one normal to the area F_n and two parallel to the area and orthogonal to each other, F_1 and F_2. The stress tensor $\boldsymbol{\sigma}$ is used to describe these forces. In particular, the diagonal components called the normal stresses σ_{ii} are responsible for F_n, while the off-diagonal components, the shear stresses τ_{ij}, are responsible for F_1 and F_2. The total forces $\mathbf{F}_s$ acting on the area are:

$$\sum \mathbf{F}_s = \int_{CS} \sigma_{ij} \mathbf{n} dA \tag{2.23}$$

where $\mathbf{n}$ is the vector normal to the infinitive area dA. The stress tensor σ_{ij} can be written as:

$$\sigma_{ij} = \begin{pmatrix} \sigma_{xx} & \tau_{xy} & \tau_{xz} \\ \tau_{xy} & \sigma_{yy} & \tau_{yz} \\ \tau_{xz} & \tau_{yz} & \sigma_{zz} \end{pmatrix} \tag{2.24}$$

The total force on the element are therefore:

$$\sum \mathbf{F} = \sum \mathbf{F}_b + \sum \mathbf{F}_s = \int_{CV} \rho \mathbf{g} dV + \int_{CS} \sigma_{ij} \cdot \mathbf{n} dA \tag{2.25}$$

The derivative $\frac{d\mathbf{Q}}{dt}$ corresponds to $\mathbf{F} = m\mathbf{a} = \frac{d\mathbf{Q}}{dt}$, so equating 2.28 to 2.25 brings to:

$$\int_{CV} \rho \mathbf{g} dV + \int_{CS} \sigma_{ij} \cdot \mathbf{n} dA = \int_{CV} \frac{\partial}{\partial t}(\rho \mathbf{u}) dV + \int_{CS} (\rho \mathbf{u}) \mathbf{u} \cdot \mathbf{n} dA \tag{2.26}$$

From the divergence theorem:

(2.27)so Eq. 2.26 becomes:

$$\int_{CV} \left[\frac{\partial}{\partial t}(\rho \mathbf{u}) + \nabla \cdot (\rho \mathbf{u}\mathbf{u}) - \rho \mathbf{g} - \nabla \cdot \sigma_{ij}\right] dV = 0 \tag{2.28}$$

The control volume is arbitrary, so that the expression inside the brackets must be true for every CV. Eq. 2.28 becomes:

$$\frac{\partial}{\partial t}(\rho \mathbf{u}) + \nabla \cdot (\rho \mathbf{u}\mathbf{u}) = \rho \mathbf{g} + \nabla \cdot \sigma_{ij} \tag{2.29}$$

and it is also called Cauchy equation. The stress tensor can be written as the sum of a hydrostatic part and a deviatoric one:

$$\sigma_{ij} = \begin{pmatrix} \sigma_{xx} & \tau_{xy} & \tau_{xz} \\ \tau_{xy} & \sigma_{yy} & \tau_{yz} \\ \tau_{xz} & \tau_{yz} & \sigma_{zz} \end{pmatrix} = \begin{pmatrix} -p & 0 & 0 \\ 0 & -p & 0 \\ 0 & 0 & -p \end{pmatrix} + \begin{pmatrix} \tau_{xx} & \tau_{xy} & \tau_{xz} \\ \tau_{xy} & \tau_{yy} & \tau_{yz} \\ \tau_{xz} & \tau_{yz} & \tau_{zz} \end{pmatrix} \tag{2.30}$$

For the hypothesis on the fluid, the stresses of the deviatoric part are linearly related to the rates of deformation, so:

$$\sigma_{ij} = -p\delta_{ij} + 2\mu\varepsilon_{ij} \tag{2.31}$$

where μ is the the dynamic viscosity and ε_{ij} are the components of the strain tensor $\boldsymbol{\varepsilon}$:

$$\boldsymbol{\varepsilon} = \begin{bmatrix} \varepsilon_{xx} & \varepsilon_{xy} & \varepsilon_{xz} \\ \varepsilon_{yx} & \varepsilon_{yy} & \varepsilon_{yz} \\ \varepsilon_{zx} & \varepsilon_{zy} & \varepsilon_{zz} \end{bmatrix} = \begin{bmatrix} \frac{\partial u_x}{\partial x} & \frac{1}{2}\left(\frac{\partial u_x}{\partial y} + \frac{\partial u_y}{\partial x}\right) & \frac{1}{2}\left(\frac{\partial u_x}{\partial z} + \frac{\partial u_z}{\partial x}\right) \\ \frac{1}{2}\left(\frac{\partial u_y}{\partial x} + \frac{\partial u_x}{\partial y}\right) & \frac{\partial u_y}{\partial y} & \frac{1}{2}\left(\frac{\partial u_y}{\partial z} + \frac{\partial u_z}{\partial y}\right) \\ \frac{1}{2}\left(\frac{\partial u_z}{\partial x} + \frac{\partial u_x}{\partial z}\right) & \frac{1}{2}\left(\frac{\partial u_z}{\partial y} + \frac{\partial u_y}{\partial z}\right) & \frac{\partial u_z}{\partial z} \end{bmatrix} \tag{2.32}$$

The new formulation of σ_{ij} substituted in 2.29 returns the Navier-Stokes equations:

$$\frac{D\mathbf{u}}{Dt} = \frac{\partial \mathbf{u}}{\partial t} + \mathbf{u} \cdot \nabla \mathbf{u} = -\frac{1}{\rho}\nabla p + \nu \nabla^2 \mathbf{u} + \mathbf{g} \tag{2.33}$$

where $\nu = \mu/\rho$ is the kinematic viscosity.

2.2.1 Initial and boundary conditions

The system that describes an incompressible fluid using the Navier-Stokes equation is:

$$\begin{cases} \dfrac{\partial \mathbf{u}}{\partial t} + \mathbf{u} \cdot \nabla \mathbf{u} = -\dfrac{1}{\rho}\nabla p + \nu \nabla^2 \mathbf{u} + \mathbf{g}, & \mathbf{x} \in \Omega,\ t > 0 \\ \nabla \cdot \mathbf{u} = 0, & \mathbf{x} \in \Omega,\ t > 0 \end{cases} \tag{2.34}$$

where Ω is a domain $\Omega \subset \mathbb{R}^d$, with $d = 2{,}3$. Initial and boundary conditions are needed for the well-posedness of the problem. At the instant $t = 0$, the velocity $\mathbf{u}$ has to satisfy the following equation:

$$\mathbf{u}(0, \mathbf{x}) = \mathbf{u}_0(\mathbf{x}), \qquad \mathbf{x} \in \Omega \tag{2.35}$$

Two different boundary conditions are used for this problem: the Dirichlet boundary conditions, applied to a portion of the boundary Γ_D, and the Neumann boundary conditions, which specify the value of a derivative applied on the boundary Γ_N, such that $\Gamma_D \cup \Gamma_N = \partial\Omega$ and $\Gamma_D \cap \Gamma_N = \emptyset$:

$$\begin{cases} \mathbf{u}(\mathbf{x},t) = \varphi(\mathbf{x},t), & \mathbf{x} \in \Gamma_D \\ \left(\nu\dfrac{\partial \mathbf{u}}{\partial \mathbf{n}} - p\mathbf{n}\right)(\mathbf{x},t) = \psi(\mathbf{x},t), & \mathbf{x} \in \Gamma_N \end{cases} \tag{2.36}$$

where φ and ψ are the vector functions. The Dirichlet conditions set a velocity on the inflow boundary, or are used when a solid boundary moves using a prescribed velocity. The case for which $\mathbf{u} = 0$ is called *no-slip* boundary condition, because the fluid is forced to adhere to the wall, while the condition $\mathbf{u} \cdot \mathbf{n} = 0$, with $\mathbf{n}$ outer normal vector on $\partial\Omega$, imposes the *impermeability* of the boundary. For the latter, if the boundary Γ_N is a plane, a Neumann condition can be applied to the pressure in the form of $\dfrac{\partial p}{\partial \mathbf{n}} = \mathbf{g} \cdot \mathbf{n}$.

2.2.2 Turbulence models

In most cases, the flow is turbulent, and the viscous forces prevail over the inertial ones, making the case complicated to study. The engineering approach focuses on studying the average quantities of the equations to simplify the problem. To do so, it is helpful to decompose each variable into an ensemble-averaged component and a fluctuation term. The velocity and pressure hence become $u_i = \langle u_i \rangle + u_i' = \bar{u}_i + u_i'$ and $p = \langle p \rangle + p' = \bar{p} + p'$. Applying the ensemble average and its properties on the continuity and the Navier-Stokes equations, the results are:

$$\begin{gathered} \frac{\partial \bar{u}_i}{\partial x_i} = 0 \\ \frac{\partial \bar{u}_i}{\partial t} + \bar{u}_j\frac{\partial \bar{u}_i}{\partial x_j} + \frac{\partial \langle u_i' u_j' \rangle}{\partial x_j} = -\frac{1}{\rho}\frac{\partial \bar{p}}{\partial x_i} + \nu\frac{\partial^2 \bar{u}_i}{\partial x_j \partial x_i} - g\delta_{i3} \end{gathered} \tag{2.37}$$

The second member of the Navier-Stokes equation can also be rewritten as:

$$-\frac{1}{\rho}\frac{\partial \bar{p}}{\partial x_i} + \nu\frac{\partial^2 \bar{u}_i}{\partial x_j \partial x_i} - g\delta_{i3} = -\frac{1}{\rho}\frac{\partial}{\partial x_i}\langle \tau_{ij} \rangle - g\delta_{i3} \tag{2.38}$$

where $\langle \tau_{ij} \rangle$ is a term that comprehends $\bar{p}\delta_{ij} - \mu\left(\dfrac{\partial \bar{u}_i}{\partial x_j} + \dfrac{\partial \bar{u}_j}{\partial x_i}\right) + \rho\langle u_i' u_j' \rangle$, also written as $\bar{p}\delta_{ij} - \tau_{lam} - \tau_{turb}$. The turbulent part of the expression is much bigger than the laminar one, thus it cannot be neglected. Moreover, it introduces new variables. As a result, it is not possible to solve this system of equations; only an approximate solution can be found. One of the most famous solutions for this issue is the Boussinesq closure, which introduces a turbulent viscosity μ_T:

$$\tau_{turb} = -\mu_T\left(\frac{\partial \bar{u}_i}{\partial x_j} + \frac{\partial \bar{u}_j}{\partial x_i}\right) \tag{2.39}$$

Different approximations to solve the Reynolds Averaged Navier-Stokes equations (RANS) were proposed after Boussinesq. The most popular ones are:

- $k - \varepsilon$ Turbulence Model
  This model was first introduced by Launder and Spalding in 1974 [37] and uses the turbulence kinetic energy k and the rate of dissipation of turbulence kinetic energy ε to describe the

turbulent viscosity $\mu_T = \rho C_\mu \dfrac{k^2}{\varepsilon}$, where $C_\mu = 0.09$. The equations for k and ε are computed as:

$$\frac{\partial(\rho k)}{\partial t} + \nabla \cdot (\rho k \bar{\mathbf{u}}) = \nabla \cdot \left[\left(\mu + \frac{\mu_t}{\sigma_k} \right) \nabla k \right] + P_k - \rho(\varepsilon - \varepsilon_0) + S_k \tag{2.40}$$

$$\frac{\partial(\rho \varepsilon)}{\partial t} + \nabla \cdot (\rho \varepsilon \bar{\mathbf{u}}) = \nabla \cdot \left[\left(\mu + \frac{\mu_t}{\sigma_\varepsilon} \right) \nabla \varepsilon \right] + \frac{1}{T_e} C_{\varepsilon 1} P_\varepsilon - C_{\varepsilon 2} f_2 \rho \left(\frac{\varepsilon}{T_e} - \frac{\varepsilon_0}{T_0} \right) + S_\varepsilon \tag{2.41}$$

where P_k and P_ε are production terms, f_2 is a dumpling function, $\sigma_\varepsilon, \sigma_k, C_{\varepsilon 1}, C_{\varepsilon 2}$ are model coefficients, and they all depend on the $k - \varepsilon$ variant used. T_e is the large eddy time scale and T_0 is a specific time scale, S_k and S_ε are source terms, ε_0 is the ambient turbulence value in the source terms that counteracts turbulence decay. This is a simple model, used for flows that develop far from the walls since it is less accurate in the boundary layer; its simplicity translates into a lower computational cost.

- $k - \omega$ Turbulence Model
  A decade later, a new significant model was proposed by Wilcox [38]. His model, on the contrary to $k - \varepsilon$, performs quite well for flow with a strong pressure gradient and internal flow, and it can be applied throughout the boundary layer, including the viscous region, without any other modifications. Rather than ε, a new variable is employed, the specific dissipation rate ω, still connected to ε as $\omega \propto \varepsilon / k$. Here the turbulent viscosity is $\mu_T = \dfrac{k}{\omega}$ and the equations for k and ω are:

$$\frac{\partial(\rho k)}{\partial t} + \nabla \cdot (\rho k \, \bar{\mathbf{u}}) = \nabla \cdot [(\mu + \sigma_k \mu_t) \nabla k] + P_k - \rho \beta^* f_{\beta^*} (\omega k - \omega_0 k_0) + S_k \tag{2.42}$$

$$\frac{\partial(\rho \omega)}{\partial t} + \nabla \cdot (\rho \omega \, \bar{\mathbf{u}}) = \nabla \cdot [(\mu + \sigma_\omega \mu_t) \nabla \omega] + P_\omega - \rho \beta f_\beta \left(\omega^2 - \omega_0^2 \right) + S_\omega \tag{2.43}$$

  where σ_k, σ_ω, $C_{\varepsilon 1}$, and $C_{\varepsilon 2}$ are model coefficients, P_k and P_ω are production terms, f_{β^*} and f_β are respectively the free-shear modification factor and the vortex-stretching modification factor, S_k and S_ω are the source terms, and k_0 and ω_0 are the ambient turbulence values that counteract turbulence decay. A problem encountered when applying this model, though, is its high sensitivity to free-stream conditions.

- SST $k - \omega$ Turbulence Model
  A good compromise between the two models explained above was found by Menter in 1994 [39]: the Shear Stress Transport (SST) $k - \omega$ model. The transport equations are the same as the ones seen for the $k - \omega$ turbulence model; however, the coefficients used this time hide a blending function F_1 that is related to the distance from the wall and to a cross-diffusion coefficient containing the dot product $\nabla k \cdot \nabla \omega$, which activates if far from the wall. In this way, the SST $k - \omega$ model gives results almost identical to the $k - \varepsilon$ one in the free stream. Furthermore, the turbulent viscosity is calculated differently, depending also on the distance from the wall

$$\mu_T = \rho k \, \min\left(\frac{\alpha *}{\omega}, \frac{a_1}{S F_2} \right) \tag{2.44}$$

  where F_2 is another blending function, $\alpha *$ depends on F_1 and $a_1 = 0.31$ and S is the module of the mean strain rate tensor.

There are some cases for which a higher accuracy is required. In RANS equations, the flow is statistically steady, hence they are not able to reproduce some peculiar phenomena of the turbulence, such as vortex shredding and wakes. On the contrary, the direct numerical

simulation (DNS) is the most precise solution: it solves the Navier-Stokes equations for all the motions without approximations, encompassing all the turbulence scales. Obviously, it gives the most complete analysis of a flow; however, its computational cost is extremely high and high-performance computational centers are required. For this reason, it is only used for extensive research on the nature of the turbulent flow. A good balance between the two approaches is the large eddy simulation (LES), since it solves only the larger eddies while it averages the smaller ones. A comparison between the three methods is shown in Figure 2.1. The computational cost

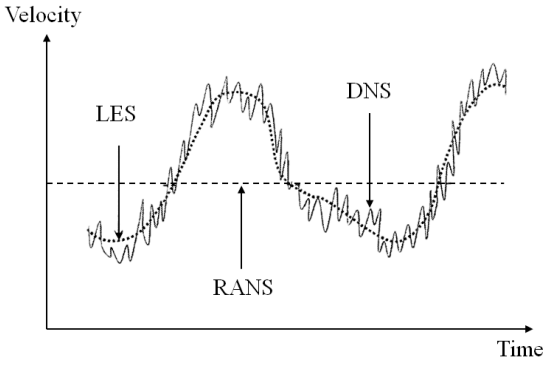

Figure 2.1: Comparison between RANS, LES and DNS [40].

remains high; however, being the smallest eddies the most expensive ones, this solution is able to save a large portion of resources while keeping a very high accuracy. To do so, a length scale of the grid is chosen as reference, and the eddies bigger than the scale are solved, while the others are filtered and, consequently, approximated. The principle is the same used to get RANS equations: the variables are decomposed into a filtered value ($\tilde{\mathbf{u}}$, $\tilde{\mathbf{p}}$) and into a sub-grid value that is not considered in the new model. The equations obtained and the RANS equations are very similar:

$$\frac{\partial \tilde{u}_i}{\partial x_i} = 0 \tag{2.45}$$

$$\frac{\partial \tilde{u}_i}{\partial t} + \frac{\partial \widetilde{u_i u_j}}{\partial x_j} = -\frac{1}{\rho}\frac{\partial \tilde{p}}{\partial x_i} + \nu \frac{\partial^2 \tilde{u}_i}{\partial x_j \partial x_i} - g\delta_{i3} \tag{2.46}$$

The term $\widetilde{u_i u_j}$ is difficult to calculate; for this reason, the residual stress tensor τ_{ij}^R is introduced, such that $\tau_{ij}^R = \widetilde{u_i u_j} - \tilde{u}_i \tilde{u}_j$. Eq. 2.46 becomes:

$$\frac{\partial \tilde{u}_i}{\partial t} + \tilde{u_j}\frac{\partial \tilde{u}_i}{\partial x_j} = -\frac{1}{\rho}\frac{\partial \tilde{p}}{\partial x_i} + \nu \frac{\partial^2 \tilde{u}_i}{\partial x_j \partial x_i} - \frac{\partial \widetilde{u_i u_j}}{\partial x_i} - g\delta_{i3} \tag{2.47}$$

The closure of the equations is achieved by modeling τ_{ij}^R. The approximation happens for scales that are smaller than the mesh size, which can become very fine when trying to capture the details. This procedure, of course, translates into a higher computational cost. The detached eddy simulation (DES) was born with the intent to cut down those costs by using RANS in the boundary layers, where the flow is still attached, and LES in the detached regions to capture the flow separation (where the grid is fine enough). A blending function determines the switch from one model to the other. A variant of DES is the delayed detached eddy simulation (DDES), which addresses the problem of an early switch to LES model when the mesh refinement leaves the model to be used uncertain. To do so, it delays the entry of LES till a specific degree of turbulent

intensity is reached. Another variation is the IDDES (Improved Delayed DES), for which the wall distance influences the length of the scale used. The new modification applies the RANS model to a thinner region, where the distance from the wall is smaller than the boundary-layer thickness. The IDDES model is the one used in this study. Figure 2.2 is a frame taken from one of the simulations, and it shows the blending function at a certain time: where the blending function is equal to 1, it means that the SST k-ω model is used; otherwise, if it is equal to 0, the LES turbulence model is used.

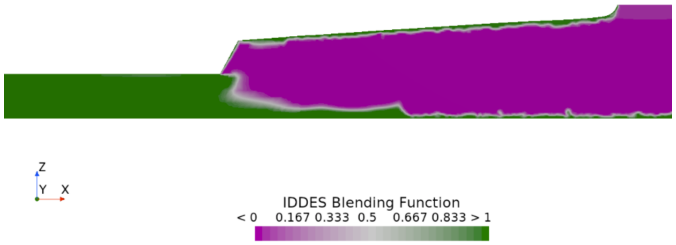

Figure 2.2: Blending function range.

Chapter 3

Set-up

This chapter describes the set-up of the simulations. It contains a description of the imported geometry, how the mesh was computed and the definition of *overset mesh*, the initial and boundary conditions used for each case, and the stopping criteria chosen for this study. Moreover, a section is dedicated to the explanation of the *scale effect*: which similarity is chosen and the reason behind it, how it is applied to the simulations, and the problems that can occur.

3.1 Geometry

The simulations were run using two different ships. The first one is a double-end ferry named *Lodi* that operates on Lake Constance, connecting the city of Konstanz with Meersburg and transporting up to 700 passengers and 64 cars for each trip. It started its service in 2010, substituting the *Fritz Arnold* ferry, and it is named after the Italian city of Lodi, to honor the partnership between the two towns. So far, it is the largest boat that operates for the municipality: it has a length of 82.37 m and a width of 13.40 m, reaching a speed of 12 knots (Figure 3.1a). Two diesel engines MTU series 4000 of 746 kW each are adopted, and the vessel is equipped with a total of two propellers, one on each side of the ferry [41] [42]. Table 3.1 shows some characteristic parameters of the ferry and the VSP. The second ferry operates in the German island of Rügen,

Ferry parameters	Value [m]	VSP parameters	Value
Length over all	82.37	N. of blades	5
Length between perpendiculars	82.37	Orbital diameter	2.1 m
Breadth on water level	13.00	Blade length	1.1 m
Height of ship sides from keel	3.50	Inclination	3.9°
Draft	2.09	Rotation rate	9.57 rad/s

Table 3.1: Lodi: boat parameters (left) and VSP parameters (right).

connecting its central part to the peninsula of Wittow in its narrowest point through a 350 m canal that the ship crosses in less than 20 minutes, avoiding the 60 km road necessary by car. The route has been adopted for more than a century; at the beginning, locomotives and wagons were also transported through it. The current ferry has been in use since 1996: it is 42.5 m long and 11.6 m wide and can reach the velocity of 8 knots (Figure 3.1b). It is powered by three 245

kW diesel engines that move the two 1.2 m diameter VSP, one at each end of the boat [43][44]. More details in Table 3.2.

For the case studied, the boats are motionless while the propellers are rotating. For this reason,

Ferry parameters	Value [m]	VSP parameters	Value
Length overall	38.0	N. of blades	5
Length between perpendiculars	38.0	Orbital diameter	1.2 m
Breadth on water level	11.6	Blade length	0.75 m
Height of ship sides from keel	2.6	Inclination	1.3°
Draft	1.3	Rotation rate	16.7 rad/s

Table 3.2: Wittow: boat parameters (left) and VSP parameters (right).

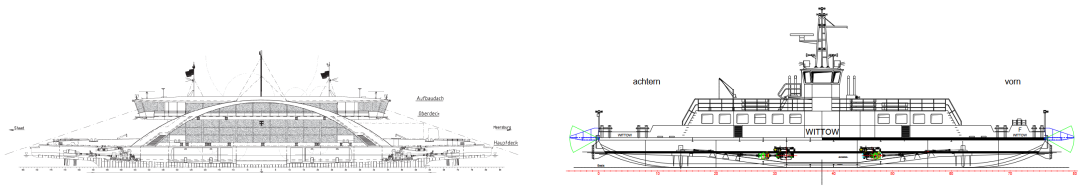

(a) Lodi ferry **(b)** Wittow ferry

Figure 3.1: Drawing of (a) Lodi and (b) Wittow ferry.

only half of the geometry is considered (therefore only one VSP), the one next to the quay wall (Figure 3.2). Around the geometry, a fluid volume shaped as a rectangular prism is defined as the

(a) Lodi **(b)** Wittow

Figure 3.2: Side view of the geometries of the ferries.

domain over which the simulation is run. The measurements used are described in Figure 3.3. The center of the propeller, chosen as the reference point, is located in the middle of the orbital diameter and at half of the blade length. The symbols D_L and D_W represent the diameters of the two ferries, whose values can be found in Table 3.1 and 3.2. The measurement x_{qu} and h_p are respectively the distance from the center of the propeller to the quay wall and to the seabed. The triangular prism with a vertex in the reference point, an edge on the quay wall and the base on the seabed corresponds to the VSP wake refinement (more details in Figure 3.3). For the unrestricted cases, the wake ends at a distance of $x = 15D_L$ and $z = -0.6D_L$ from the reference point for the Lodi ferry (Figure 3.4), and $x = 23D_W$ and $z = -1.2D_W$ for the Wittow ferry. Six different cases are analyzed for both boats:

- Open-sea:

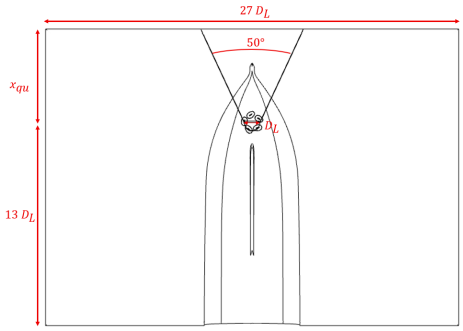

(a) Lodi: top view.

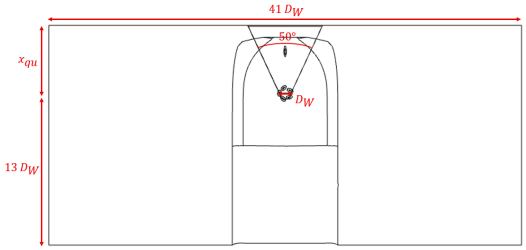

(b) Lodi: front view.

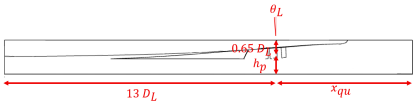

(c) Wittow: top view.

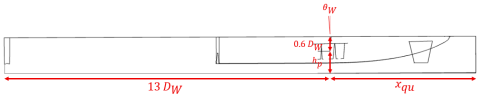

(d) Wittow: front view.

Figure 3.3: Orthogonal projections of Lodi ferry (left) and Wittow ferry (right).

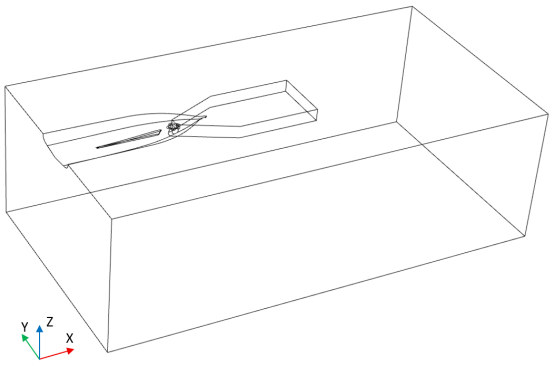

Figure 3.4: Outline of the domain for the Lodi ferry: unrestricted case.

→ Lodi: $x_{qu} = 38D_L$, $h_p = 15D_L$

→ Wittow: $x_{qu} = 46D_W$, $h_p = 16D_W$

- $x_{qu} = 6D$, $h_p = 0.9D$
- $x_{qu} = 8D$, $h_p = 0.9D$
- $x_{qu} = 11D$, $h_p = 0.9D$
- $x_{qu} = 6D$, $h_p = 1.8D$
- $x_{qu} = 6D$, $h_p = 2.7D$

The case "open-sea" simulates the condition where there are no walls; for this reason, the distance from the restriction is very far, so that the wake is not influenced by the restrictions. For the confined case, D is equal to D_L for the Lodi ferry and to D_W for the Wittow one. The ratios were decided according to the literature: the distances chosen from the propeller to the quay

wall (6D, 8D, 11D) and to the seafloor (0.9D, 1.8D, 2.7D) are included in the range typical of publications regarding propeller-induced scour (some examples: [45][30][46][47][48]).
In the simulations, the surface of the water is plane and does not change its form when the propeller runs. This is because the accuracy of the results obtained using a multiphase flow model did not sufficiently justify the associated increase in computational costs. However, if the boat is moving, the influence of the waves must be taken into account.

3.2 Meshing

The mesh is computed on each part differently, finding a balance between the accuracy that is needed for the simulation and the computational costs. Different meshers are used in the simulation:

- *Surface remesher*: it retriangulates a surface to improve its quality and optimize the shapes of its cells. It is controlled mainly by a user-defined target edge length, with optional features that include refinement based on curvature and surface proximity. It is possible to choose which surfaces or boundaries to include and whether to localize refinements with the proximity refinement; this feature is used in particular for close surfaces by stating the direction of the refinement. This process, if specified, can also create aligned meshes that better fit the curvature of the CAD.
- *Trimmed cell mesher*: this technique generates a hexahedral mesh, aligned with the coordinate system defined and refined near the edges (Figure 3.5). The result of this operation is a mesh mainly created by hexahedral cells and trimmed polyhedral cells near the borders, which has a low skewness (the lower the skewness, the closer the cell is to an equilateral cell), a good overall quality, and is generated faster compared to other types of mesh, although it might be less accurate. The refinement depends on the base size, and it can be modified

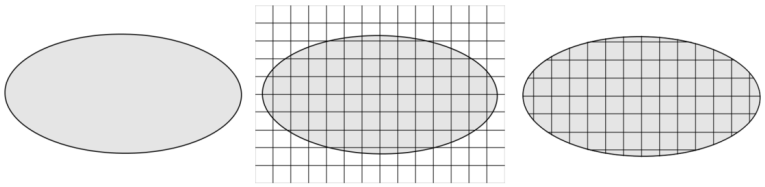

Figure 3.5: Working principle of the trimmed cell mesher [35]

  through the definition of growth factors, that controls the transition from small to larger size, and of minimum and maximum cell size. The trimmer cell mesher is used in particular to represent a fluid moving mostly in a specific direction, usually aligned with the geometry, and for external flows.
- *Prism layer mesher*: creates a prismatic cell layer. It is used near the walls to capture, completely or partly, the boundary layer (the thin region where the fluid is characterized by viscous and thermal gradients and rapid changes of the fluid variables due to the interaction solid-fluid). Since this phenomenon is difficult to describe, the mesh should be chosen accurately and according to how the flow is expected to behave. Three main parameters are defined:
  - Number of prism layers: how many layers are used to divide the boundary layer.

– Prism layer stretching: growth rate of successive prism layers.

– Prism layer total thickness: the total overall thickness of prism layers, chosen according to the physical model.

It is possible to divide the turbulent boundary layer into two main parts: the outer layer, closer to the free stream, dominated by turbulent effects, and the inner layer. The inner layer, at the same time, is split into three parts: *viscous sublayer*, *buffer layer* and *log layer* (Figure 3.6). The viscous sublayer is the closest to the wall and it is characterized by viscous

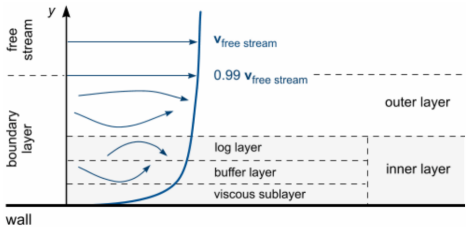

(a) Velocity profile of a turbulent boundary layer [35]

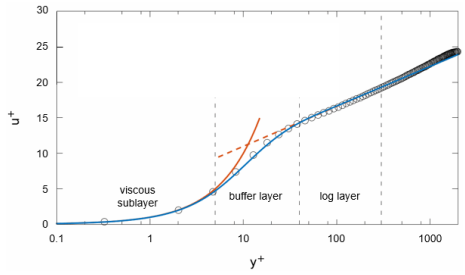

(b) Definitions of wall functions [35]

Figure 3.6: Details of the inner layer.

effects. The relationship between the dimensionless wall distance y^+ and the dimensionless velocity u^+ is very simple for this part:

$$u^+ = y^+ \tag{3.1}$$

For this region, $y^+ < 5$. The buffer layer represents a transition between the viscous and the log layer, and its wall distance is included between 5 and 30. The log layer is influenced equally by viscosity and turbulence. Its law is:

$$u^+ = \frac{1}{\kappa} \ln y^+ + C^+ \tag{3.2}$$

where κ is the Von Karman constant and C^+ is a constant. Here $30 < y^+ < 300$.
To calculate the prism layer total thickness, it is necessary to choose a value for the wall function: in the simulations, it is hypothesized to be $y^+ = 100$ (log layer); it is later verified that the wall function value remains in the range $30 < y^+ < 300$. First, the thickness of the first cell layer y_0 is calculated as $y_0 = \dfrac{y^+ \nu}{u_\tau}$, where ν is the kinematic viscosity and u_τ is the shear velocity $u_\tau = \sqrt{\dfrac{\tau_w}{\rho}}$. The wall shear stress is estimated through an empirical relationship $\tau_w = 0.5 C_f \rho U^2$, C_f is the skin friction here given by the Schlichting formula $C_f = (2 \log Re - 0.65)^{-2.3}$. After calculating the first layer, the total thickness δ, given the stretching factor k and the number of layers N, is:

$$\delta = y_0 \sum_{i=1}^{i=\mathrm{N}} k^i \tag{3.3}$$

For this study, two different meshes are used, one that encompasses the geometrical domain and the bottom of the ship (called here *background mesh*), and one just for the blades of the VSP (*blade mesh*). For the blade mesh, the cell base size BS is calculated as $BS = D/53 \times BSF$, where BSF is the base size factor equal to $1\sqrt{2}$, while for the background mesh it is $BS_B = BS \times 32$. The detailed values of the parameters used are displayed in Appendix A.1, as well as some mesh refinements. Moreover, in the background mesh, two more refinements are included: the area near the VSP, called *rotor casing vicinity*, and the area where the majority of the propeller wake is expected to develop. These refinements are necessary to capture the eddies that otherwise could

(a) Lodi mesh **(b)** Wittow mesh

Figure 3.7: Numerical grid of two of the confined geometries.

not be visible with a coarser grid. Moreover, a surface wrapper was necessary for the Wittow ferry to improve the quality of the imported mesh. The surface wrapper settings are shown in Appendix A.1. The resulting meshes for the two geometries are illustrated in Figure 3.7.

Overset mesh

The coupling between the rotor casing vicinity mesh and the rotating blades mesh is done using the overset mesh (Figure 3.8): when two or more independent grids overlap, usually including a fixed, coarser background grid, and one or more finer moving meshes, this technique is adopted. This method is applied when there is a background mesh that forms the main domain and that does not move, while the overset mesh involves the body or the parts of the body that move. When the two meshes overlap, the cells of the background region become *inactive*, so the equations in this hole are not solved (hole-cutting method). However, the cell adjacent to the hole no longer receives data from neighbouring cells; thus, it becomes an *acceptor* cell and receives values from *donor* cells located at the same position but in the other mesh with respect to the acceptor cell's centroid. If the donor cells identified are *active* cells (where the equations are solved), an interpolation between the cell that contains the centroid of the acceptor and the nearby donors is carried out. Figure 3.9 shows an example of an acceptor and the corresponding donors. In the same way, the cells at the border of the body mesh do not have neighbouring cells from which to extract the values. In this case, the cells at the end of the body mesh become acceptors, and the corresponding cells located in the background mesh become donors. Figure 3.10 shows how the cells are divided in each region, where region 0 corresponds to the background and region 1 to the overlapping body. After the identification of the donors, the values of the variables in the acceptor cell ϕ_A are calculated as:

$$\phi_A = \sum_{i}^{N_D} \omega_i \phi_{D_i} \tag{3.4}$$

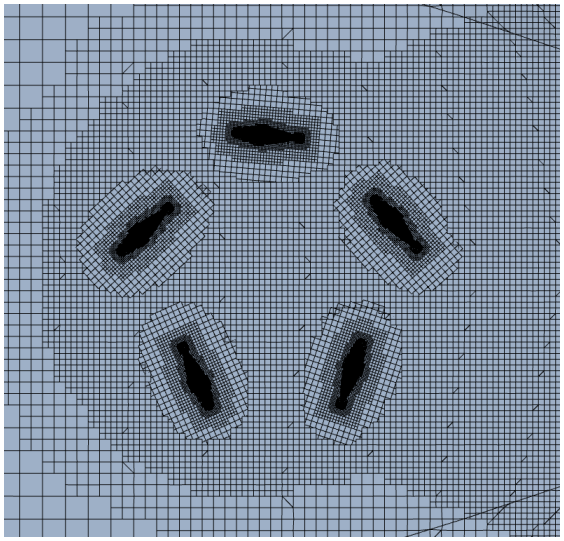

Figure 3.8: Detail of the overset mesh of one of the simulations.

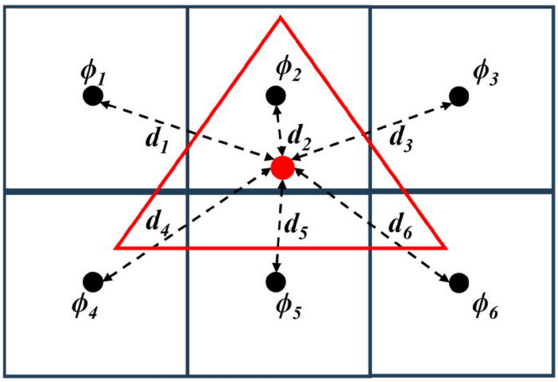

Figure 3.9: Acceptor cell (in red) and its corresponding donor cells (in black) [49].

where N_D is the number of donor cells, ω_i are the interpolation weights and ϕ_{D_i} are the values of the donors' variables. At every time step, the process is repeated: for the new acceptors, the corresponding donors are identified and the new interpolation weights are calculated.

3.3 Initial and Boundary Conditions

For the whole domain, the initial velocity is $\mathbf{u}_I = (0,0,0)$ and the initial pressure is $p_I = 0$ (relative to the reference pressure $p_{ref} = 101325\ Pa$). There are two different kinds of boundary conditions used for these simulations:

- Pressure outlet: the value of the variable is not known exactly, so it is approximated. For this reason, the boundary where this type of condition is used should be placed far from the zone of interest.
- Wall: a boundary where this condition is applied means an impermeable surface, usually

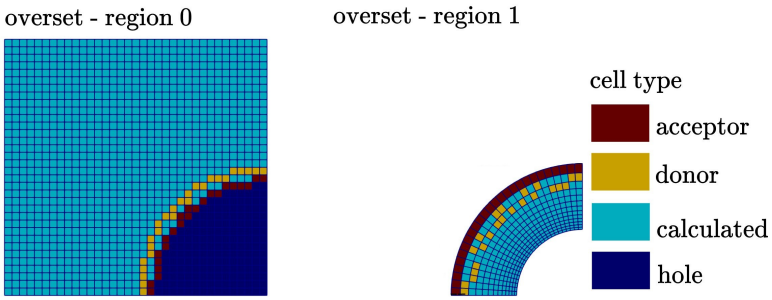

Figure 3.10: Distribution of the different cell types for the two regions [50].

confining with a solid. In this simulation, two different kinds of wall conditions are applied:

- Slip: no traction on the surface.
- No-slip: for viscous flow, it means that the velocity of the fluid relative to the wall is zero. So, for example, the fluid near the blade (that has a no-slip condition) moves with the same velocity as the blade, but near the restriction walls the velocity is zero for the flow (because the wall is not moving). Moreover, for this condition, the wall surface specification can be modified; to simulate the material on the seabed, the surface here is supposed to be rough, with a roughness height r of 0.8 mm. The other surfaces do not need this clarification and are thus chosen smooth.

All the surfaces belonging to the ferries and the blade surfaces have a wall condition, and in particular a no-slip condition. The other information regarding the boundary conditions for the domain of both restricted and unrestricted case are shown in Figure 3.11. These conditions are valid for both ferries.

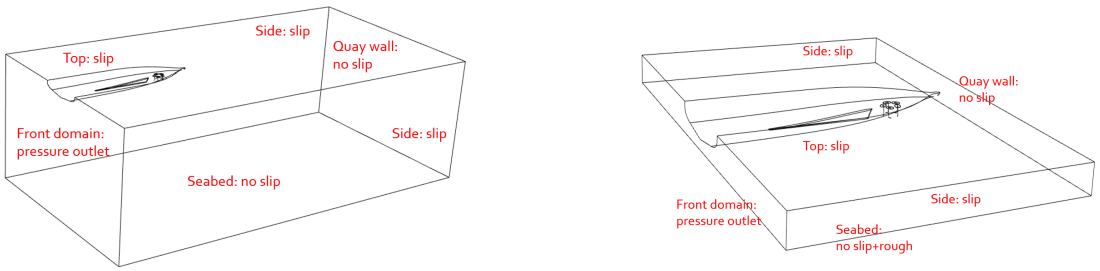

(a) Unrestricted case **(b)** Restricted case

Figure 3.11: Boundary conditions for (a) unrestricted and (b) restricted cases.

3.4 Scale effect

In this study, all six cases cited in Section 3.1 are run in model scale 1:16, and to do so, the Froude similarity is used. Using the Froude similarity means choosing the adimensional Froude

number Fr for the model equal to the full-scale one:

$$\begin{aligned} Fr_M &= Fr_F \\ \frac{U_M}{\sqrt{gL_M}} &= \frac{U_F}{\sqrt{gL_F}} \end{aligned} \tag{3.5}$$

where U is the flow velocity $[m/s]$, g is the gravity $[m/s^2]$ and L is the characteristic length $[m]$. Physically, it represents the ratio between the inertial forces and external forces (gravity):

$$\frac{F_I}{F_E} \propto \frac{\rho U^2 L^2}{\rho g L^3} = \frac{U^2}{gL} = Fr^2 \tag{3.6}$$

The scale factor λ is defined as $\lambda = \dfrac{L_F}{L_M}$. From Eq. 3.5, it is possible to calculate the relationship also for the other variables, and the results are shown in Table 3.3. In this study, $\lambda = 16$. From

Physical quantity	Measurement unit	Scale factor
Length	m	λ^1
Time	s	$\lambda^{0.5}$
Velocity	m/s	$\lambda^{0.5}$
Acceleration	m/s^2	λ^0
Mass	kg	λ^3
Density	kg/m^3	λ^0
Force	N	λ^3
Pressure	N/m^2	λ^1
Frequency	s^{-1}	$\lambda^{-0.5}$

Table 3.3: Scale factors for Froude similarities.

Table 3.1 and 3.2, using the scale factors from Table 3.3, the parameters for the model simulations are obtained. The new values of the diameter and propeller rotation rate are shown in Table 3.4. Froude similarities are usually employed for problems where gravity plays an important role, for

Ferry	Diameter [m]	Rotation rate [rad/s]
Lodi	0.13125	38.29
Wittow	0.07500	67.02

Table 3.4: Parameters for the model scale.

example in hydraulic models (as in this case). However, it does not account for viscous forces (in problems where these forces are predominant, the Reynolds similarities are used). For this reason, a comparison between the results of a model scale and full scale is made in Section 4.2. For reference, the case used is $x_{qu} = 6D_L$ and $h_p = 0.9D_L$, and the comparison is carried out only for the Lodi ferry. In this simulation, the part of the domain where the viscous forces are prevalent is near the seabed, where the surface is rough. Therefore, the roughness height r is changed to see the influence it has on the scaling effect. The comparison is made between:

- Lodi ferry, model scale: $x_{qu} = 6D_L$, $h_p = 0.9D_L$, $r = 0.8\ mm$
- Lodi ferry, full scale: $x_{qu} = 6D_L$, $h_p = 0.9D_L$, $r = 0.8\ mm$
- Lodi ferry, full scale: $x_{qu} = 6D_L$, $h_p = 0.9D_L$, $r = 12.8\ mm$

First, it is studied what happens when the roughness height is kept the same; then, also the r is scaled using the factor $\lambda = 16$. Both cases are physically valid: the former means that the seabed is made of fine sand, the latter that it is made of rocks.

3.5 Solvers

To solve the fluid equations, the flow segregated solver is used, meaning that the governing equations are solved in a sequential approach: the non-linear equations are iterated one after the other and solved for velocity and pressure. It uses an algorithm that couples pressure and velocity: at every iteration, the solver uses a pressure-correction equation to calculate the velocity components, and then it verifies if the velocity field obtained satisfies the mass conservation equation, which, for incompressible fluids (as the one studied), corresponds to the continuity equation. This technique is valid for incompressible and mildly compressible flows, but it is not suitable for high Rayleigh or Mach numbers.

3.5.1 SIMPLE algorithm

For this problem, the pressure-velocity coupling algorithm used is called SIMPLE (Semi-Implicit Method for Pressure-Linked Equations) since the momentum and pressure correction equations are solved implicitly, but the velocity correction is solved explicitly. The algorithm, at every time step, can be schematized as follows:

1. Boundary conditions are set.
2. Reconstruction gradients of velocity and pressure are calculated, as well as their gradients.
3. Discretized momentum equation is solved and an approximated velocity field $\mathbf{v}^*$ is obtained.
4. Uncorrected mass flux at face $\dot{m}_f^*$ is calculated as in Eq. 2.13.
5. The pressure correction p' is calculated using the pressure correction equation found in Eq. 2.14.
6. Pressure field is updated using the under-relaxation factor ω
$$p^{n+1} = p^n + \omega p' \tag{3.7}$$
7. Boundary pressure corrections p'_b are updated.
8. The mass fluxes are corrected
$$\dot{m}_f^{n+1} = \dot{m}_f^* + \dot{m}'_f \tag{3.8}$$
9. The cell velocities are corrected
$$\mathbf{v}_p^{n+1} = \mathbf{v}_p^* - \frac{V \nabla p'}{\mathbf{a}_p^v} \tag{3.9}$$
where $\nabla p'$ is the gradient of pressure corrections, $\mathbf{a}_p^v$ is the vector of central coefficients for the discretized velocity equation, and V is the cell volume.

The steps are repeated till the solution converges.

3.5.2 Stopping criteria

An implicit unsteady scheme is adopted, with a 2nd order temporal discretization. For each physical time-step, several inner iterations run till the solution converges or the maximum number of inner iterations is hit (in the simulation it is set to 5). Every time step corresponds to 1° rotation of the propeller, calculated as:

$$t_{\text{time step}} = BSF \times \frac{\text{degree per time step}}{n_p \; 180/\pi} = \sqrt{2} \times \frac{1}{n_p \; 180/\pi} \tag{3.10}$$

Table 3.5 shows the value of the time step for the three different cases. The simulation ends when

Case	Time step [s]
Lodi ferry, model scale	$6.444988717837322 \times 10^{-4}$
Wittow ferry, model scale	$3.682847818679936 \times 10^{-4}$
Lodi ferry, full scale	0.0025779954871349288

Table 3.5: Time step value.

the propeller makes 100 full rotations, calculated as:

$$t_{\text{max}} = 100 \times t_{\text{full rotation}} = 100 \times \frac{1}{n_p/(2\pi)} \tag{3.11}$$

The results from the calculation are given in Table 3.6.

Case	Time step [s]
Lodi ferry, model scale	16.406262817392825
Wittow ferry, model scale	9.375000000000000
Lodi ferry, full scale	65.6250512695713 s

Table 3.6: Time step value.

The sources used for this chapter are: [51][52][53][54][55][35][56][57][58][36][59][60].

Chapter 4

Results

In this chapter, the influence of wall clearance and seabed clearance (respectively, the distance from the centre of the propeller to the vertical and horizontal wall) on the wake is investigated, with a particular focus on the velocity, as well as the values of shear stress and pressure calculated on the walls. An in-depth investigation is made to predict the area of the seafloor where the erosion is most likely to happen. Then, a detailed study is carried out on the detected VSP frequencies for both restricted and unrestricted cases, placing probes next to the propeller and in its wake. Finally, a comparison between the model scale and full scale is made, and it is examined how the value of roughness height influences the flow stream due to the scale effect.

4.1 Influence of walls on the propeller wake

As already stated in Chapter 2.2, the first part of the study only refers to the model scale of the two ferries, using $\lambda = 16$. Six different cases are run:

- Open-sea
- $x_{qu} = 6D$, $h_p = 0.9D$
- $x_{qu} = 8D$, $h_p = 0.9D$
- $x_{qu} = 11D$, $h_p = 0.9D$
- $x_{qu} = 6D$, $h_p = 1.8D$
- $x_{qu} = 6D$, $h_p = 2.7D$

where D is equal to D_L for the Lodi ferry and to D_W for the Wittow one.
In this part, only the results from the comparisons between the cases are shown; more detailed results are in Appendix AA. At first, the general influence of the refinement on the propeller stream is studied through the analysis of the velocity field. In the second part, the intensity of the pressure on the quay wall and of the shear stress on the seabed are displayed, revealing that the farther the wall is from the propeller, the lower the values of the variables are, as expected. In the last part of the section, the Fast Fourier transforms of the pressure for different points in the domain are calculated, both for a restricted and unrestricted case.

4.1.1 Velocity field

The main variable studied in this section is the maximum intensity of the velocity in both directions. This choice was made because the maximum intensity is associated with greater loads on the walls; therefore, it results in being the most significant aspect of velocity to analyze. In particular, the maximum value of the time mean velocity is studied, defined as the time mean starting from the 10th rotation of the propeller (to avoid the influence of the instability of the first rotations) till the end of the simulation (100th rotations). In general, the time mean quantities in this study are calculated as:

$$\bar{x} = \frac{1}{N}\sum_{i=1}^{N} x_i \tag{4.1}$$

where x_i is the function value at step i, and N is the number of time-steps or iterations for which data has been collected. In particular, the time step at which the counting starts is calculated as:

$$t_{\text{time mean start}} = 10 \times \frac{t_{\text{full rotation}}}{t_{\text{time step}}} \tag{4.2}$$

where the formulation of $t_{\text{full rotation}}$ and $t_{\text{time step}}$ are shown in Eq. 3.10 and 3.11. This formulation is also valid for the time mean pressure and the time mean longitudinal shear stress.

From now on, the term *mean* and the symbol $\bar{x}$ will be used to refer to time mean quantities starting from ten rotations of the propeller.

To reduce the number of variables to study, a consideration about the longitudinal component of the velocity is made: in a volume right behind the propeller, defined as a rectangular prism with measurements $x \in [0.75D, 7.5D]$, $y \in [-1.5D, 1.5D]$, $z \in [-0.6875, 0.6875]$, the maximum values of the absolute velocity and the maximum values of the longitudinal velocity found in that volume are computed (Figure 4.1). In the graph, the velocity is adimensionalized dividing by $U = n_p \frac{D}{2}\frac{1}{\sqrt{\lambda}} = 2.51\ m/s$ and t_{ad}, the non-dimensional time calculated as $t_{ad} = t\ \frac{U}{D}$. Figure 4.1

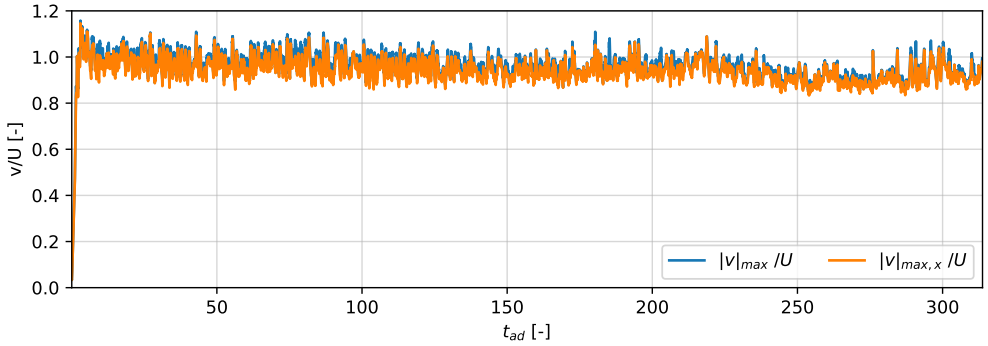

Figure 4.1: Maximum absolute and longitudinal component of the velocity found in the defined volume.

is obtained from the Lodi ferry, for $x_{qu} = 6D_L$, $h_p = 0.9D_L$, but similar results are achieved for all the cases, as well as for the Wittow ferry. As shown, the longitudinal component of the velocity is the main contributor to the absolute velocity, making the other two components negligible; for this reason, from now on, the study is focused mainly on this component. By doing so, it is possible to analyze where the velocity is negative, meaning where the backflow is.

From now on, the longitudinal component of the velocity, in particular the longitudinal component of the *mean* velocity $\bar{v}_x$, is considered and abbreviated as *mean longitudinal velocity* $\bar{v}_{x_{max}}$.

To understand how the flow behaves right below the propeller and the influence of that the presence of walls has, the domain is divided into x-sections, equally spaced by D, starting from $x = 1D$ and ending one diameter D before the quay wall, resulting in five x-section if $x_{qu} = 6D$, seven if $x_{qu} = 8D$ or ten if $x_{qu} = 8D$. For every x-section, the point with the maximum value of the mean longitudinal velocity is found, and the y-coordinate corresponding to that point is locked; so for those fixed values of x and y, the velocity profile along the z-axis is drawn. The results are shown in Figure 4.2, and the symbol • represents where the maximum value of the mean longitudinal velocity is, and the dash-dot black line in every section defines where $\bar{v}_{x_{max}} = 0$. The points with the maximum value of the longitudinal velocity are really close to each other

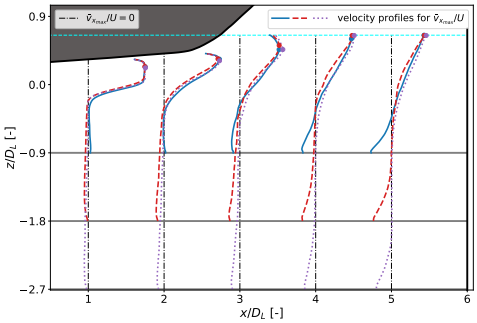

(a) Lodi ferry

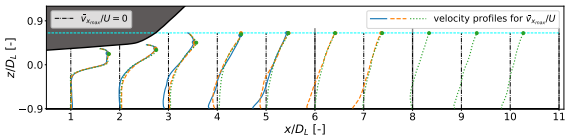

(b) Lodi ferry

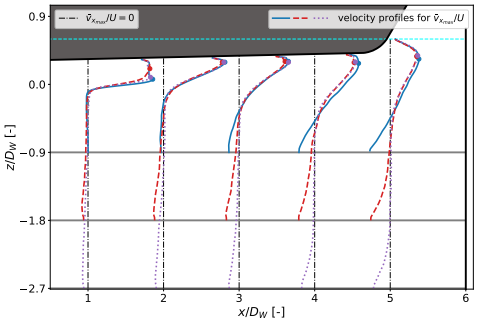

(c) Wittow ferry

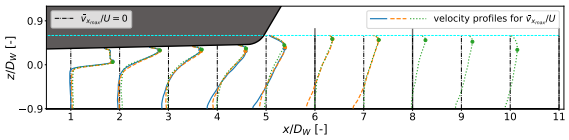

(d) Wittow ferry

Figure 4.2: Velocity profiles of the mean longitudinal velocity for the different cases. Figures (a) and (c) show the cases where $x_{qu}/D = 6$, figures (b) and (d) show the cases where $h_p/D = 0.9$.

in every configuration, meaning that the difference between every case for the same x-section is very small, and they follow an ascending trajectory along the z-axis: none of them is located below the centre of the propeller in (0,0,0). For this reason, the higher values of the pressure load on the quay wall are expected to be in the upper part of its area. Moreover, the analysis of the longitudinal component of the velocity makes it possible to see where the backflow is stronger. Predictably, the case with the walls closer to the propeller displays a more prominent backflow (that means higher negative velocity at the toe of the vertical wall). The figures also show the influence that the geometry of the hull has on the flow: Lody ferry has a linear hull profile, while Wittow's hull has a hollow (visible in Figure 3.1b) that holds back the flow. This feature results in a more turbulent flow while it is below the Wittow's hull, but as soon as the flow leaves behind the

boat, its kinetic energy decreases, translating into a lower maximum velocity. This phenomenon and the comparison between the two ships regarding the maximum values of the longitudinal mean velocity for every section are seen in detail in Figure 4.4. The graphs show that all the cases

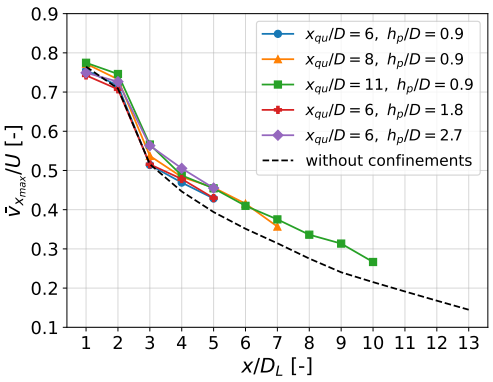

(a) Lodi ferry

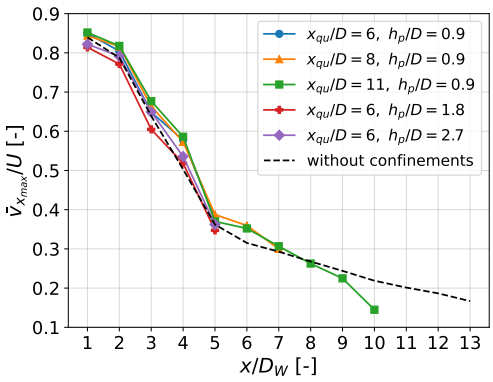

(b) Wittow ferry

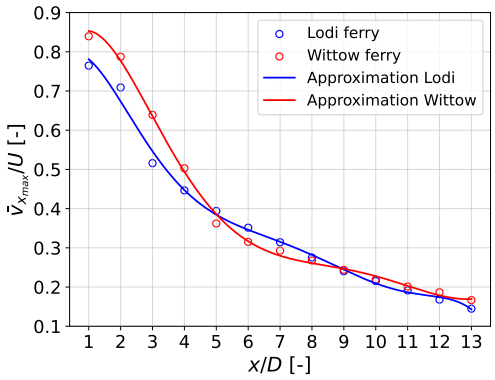

(c) Unrestricted case comparison

Figure 4.3: Comparison of the maximum values of the mean longitudinal velocity for different x/D sections for (a) Lodi ferry, (b) Wittow ferry and (c) a direct comparison using the unrestricted cases and the approximation polynomials.

(including the unconstrained ones) follow the same trend regarding the maximum value of the longitudinal mean velocity. For the Lodi ferry, the unrestricted case reaches lower values of $\bar{v}_{x_{max}}$ compared to the restricted cases, especially when the x-sections no longer contain the Lodi's underwater hull (that means from section $x/D_L = 4$ on, as shown in Figure 4.2). Regarding the second vessel, the overlapping is more evident; however, as for the previous description, the curves of the constrained simulations are well approximated by the open-sea case while the hull is underwater (it means till the x-section $x/D_W = 5$ Figure 4.2). Additionally, Figure 4.3c shows the direct comparison between the two boats for the unrestricted case and the influence that the shape of the hull has on the flow. The approximation polynomials for this case are written in Table 4.1. As explained above for the restricted cases in Figure 4.2, the shape of Wittow's hull results in higher maximum velocities than the Lodi ship for sections that encompass its underwater part. Right after Wittow's hull, corresponding to section $x/D = 5$, $\bar{v}_{x_{max}}$ related to Wittow ferry

Ship	$\frac{\bar{v}_{x_{max}}}{U} = f\left(\frac{x}{D}\right)$	
Lodi	$-7.61 \times 10^{-06}\left(\frac{x}{D_L}\right)^6 + 3.33 \times 10^{-04}\left(\frac{x}{D_L}\right)^5 - 2.24 \times 10^{-03}\left(\frac{x}{D_L}\right)^4$ $+4.50 \times 10^{-02}\left(\frac{x}{D_L}\right)^3 - 1.68 \times 10^{-01}\left(\frac{x}{D_L}\right)^2 + 1.56 \times 10^{-01}\left(\frac{x}{D_L}\right) + 7.53 \times 10^{-01}$	0.9956
Wittow	$-2.54 \times 10^{-06}\left(\frac{x}{D_W}\right)^6 + 1.52 \times 10^{-04}\left(\frac{x}{D_W}\right)^5 - 3.44 \times 10^{-03}\left(\frac{x}{D_W}\right)^4$ $+3.67 \times 10^{-02}\left(\frac{x}{D_W}\right)^3 - 1.80 \times 10^{-01}\left(\frac{x}{D_W}\right)^2 + 2.55 \times 10^{-01}\left(\frac{x}{D_W}\right) + 7.45 \times 10^{-01}$	0.9983

Table 4.1: Equations for the approximation polynomials and their R^2.

drops. After the drop, starting from $x/D = 9$, the influence of the hull is no longer detected and the two curves overlap. The two curves may be helpful when working with the two ferries: since the maximum value of the velocity is directly related to higher loads, from Figure 4.3c it is possible to predict the smaller wall clearance that the ship can reach creating no to little harm to the harbour structure, choosing a valid maximum velocity threshold based on the material of the wall. In the same way as Figure 4.3, the minimum values (corresponding to the maximum values in the negative x direction) of the longitudinal mean velocity $\bar{v}_{x_{min}}$ were calculated for each x-section, and the results are shown in Figure 4.4. The negative values mean that the flow is going in the opposite direction from the x-axis (in other words, where the flow is coming back). In these graphs, unlike $\bar{v}_{x_{max}}$, the effect of the wall clearance is clear: for the unrestricted case,

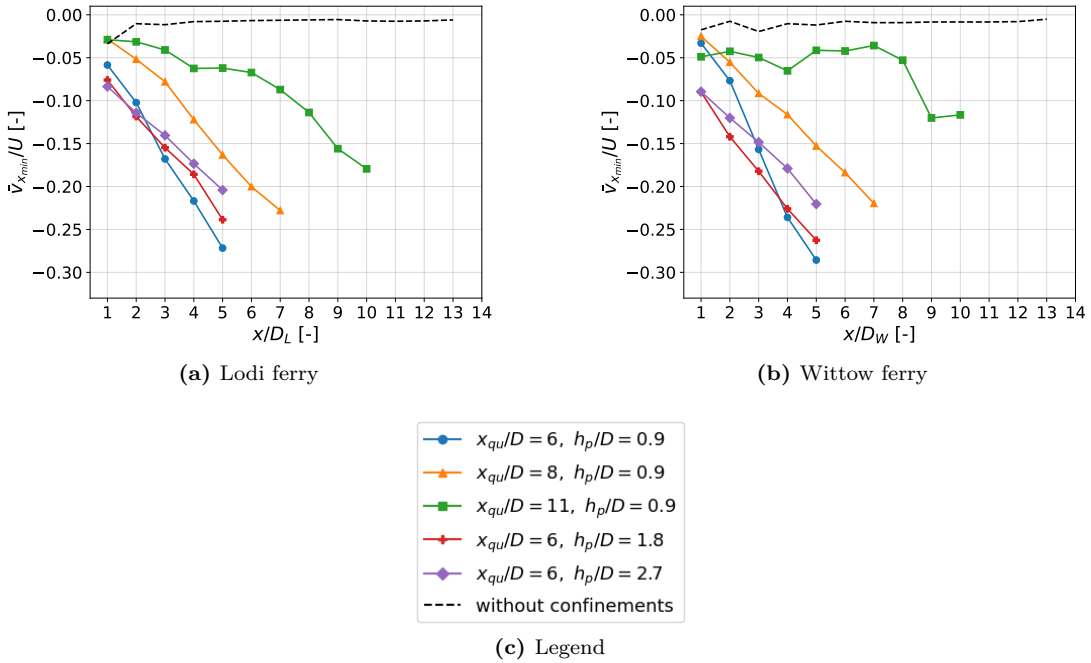

(a) Lodi ferry

(b) Wittow ferry

(c) Legend

Figure 4.4: Comparison of the minimum values of the mean longitudinal velocity for different x/D sections, for (a) Lodi ship and (b) Wittow ship.

as expected, the minimum velocity is closer zero and it is slightly lower when approaching the propeller, due to the greater turbulence that is created. However, when restrictions to the domain are applied, the $\bar{v}_{x_{min}}$ reaches lower values because of the friction created by the roughness of the seabed, which leads to a deceleration of the fluid near that wall (see Figure 4.4). It is possible already to notice a trend that will be seen in detail later: for the cases where the quay wall is farther from the propeller (case $x_{qu} = 8D$ $h_p = 0.9D$ in yellow and $x_{qu} = 11D$, $h_p = 0.9D$ in green) the minimum values of the longitudinal mean velocity of each x-section are higher than the ones where the seabed is farther (case $x_{qu} = 6D$ $h_p = 1.8D$ in red and $x_{qu} = 6D$, $h_p = 2.7D$ in purple). That means that, at the moment, the wall clearance is the leading parameter compared to the seafloor clearance when looking at the destructive events that occur when a VSP is in action: if just the seabed is moved lower, the effects will not be as beneficial as moving exclusively the quay wall away from the propeller. Figure 4.5 shows the positions in the x-z plane where the points with the minimum and maximum values of the $\bar{v}_x$ are located for every x-section starting from $x/D = 1$ to the position of the quay walls. The figures make it clearer what was

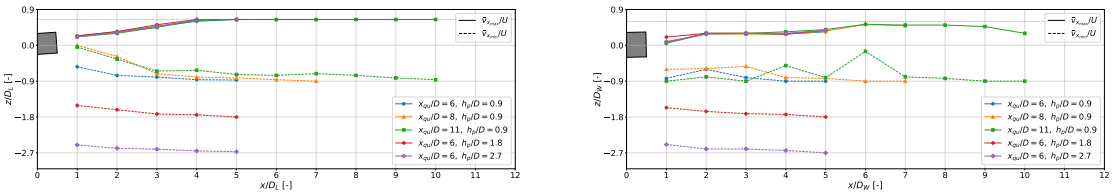

(a) Lodi ferry **(b)** Wittow ferry

Figure 4.5: Section of the x-z plane showing the position of the points with the maximum and minimum values of the mean longitudinal velocity in different x/D sections.

already discussed above: the values of $\bar{v}_{x_{max}}$ start in $x/D = 1$ from above the centre of the VSP in (0,0,0) and their z-coordinate values quickly grow till reaching the surface. This, for the Lodi ferry, happens at $x/D_L = 4$ for all the cases; the five alternatives have the almost exact value of $\bar{v}_{x_{max}}$ in every x-section, and right before the quay wall the value of $\bar{v}_{x_{max}}$ coincides with a point of the water surface. For this reason, the maximum value of the pressure on the quay wall is expected to be in the area right below the water surface. For the Wittow ferry instead, since its hull is longer compared to the Lodi one, the points corresponding to $\bar{v}_{x_{max}}$, only after the cases with $x_{qu}/D_W = 6$ reach the surface. The cases $x_{qu} = 8D_W$ $h_p = 0.9D_W$ in yellow and $x_{qu} = 11D_W$ $h_p = 0.9D_W$ in green do not reach the surface, but they get very close to it for the x-section $x/D_W = 6$. After that threshold, the values of the z-coordinates of the points decrease, in contrast to what happens with the first vessel. This could be explained by the fact that the flux follows a different trajectory because it has been deviated by the hollow in the hull, and it does not have the linear trajectory that is seen for the Lodi ferry. Regarding the location of the points $\bar{v}_{x_{min}}$, they follow the opposite trend than $\bar{v}_{x_{max}}$: starting from the center of the propeller, their z-coordinates decrease till they lay down on the seabed due to the friction created on the bottom, as already explained above. The $\bar{v}_{x_{min}}$ points locations go almost immediately close to the seafloor for the cases in which $x_{qu} = 6$ for both ships, and this is because their values, shown in Figure 4.4, are lower. This is related to the fact that the backflow is stronger for them; therefore, the locations of the points of $\bar{v}_{x_{min}}$ will be closer to the bottom, where the backflow is experienced. However, there are some points corresponding to the cases $x_{qu} = 11D$ $h_p = 0.9D$ in both boats that are not located on the seabed. The main explanation for those points is that, since the case $x_{qu} = 11D$ $h_p = 0.9D$ is the one that has the values of $\bar{v}_{x_{min}}$ closer to zero compared to the others (Figure 4.4), it is possible to find those values in other z-coordinates not

connected to the backflow. For this case, the phenomenon is weaker, especially away from the quay wall, where those "unpredicted" values are found. This is even clearer for the Wittow ferry, where the $\bar{v}_{x_{min}}$ values are closer to zero than the ones from the Lodi simulation.

To conclude the study on the longitudinal mean velocity, in every simulation a x-y plane is located at a height along the z-axis corresponding to 1/100th of the distance from the seabed to the centre of the propeller. On these planes, the maximum absolute values of the longitudinal mean velocity are computed, which is directed to the negative direction of the x-axis, since close to the bottom the maximum absolute values are imposed by the backflow, as explained above. This value is addressed as $|\bar{v}|_{b_{max}}$, and it is directed towards the negative x direction. Table

h_p/D [-]	Lodi: $\lvert\bar{v}\rvert_{b_{max}}/U$ [-]	Difference with case $h_p = 0.9D$ [%]	Wittow: $\lvert\bar{v}\rvert_{b_{max}}/U$ [-]	Difference with case $h_p = 0.9D$ [%]
0.9	0.291	-	0.296	-
1.8	0.257	-11.7	0.275	-7.09
2.7	0.224	-23.0	0.233	-21.3

Table 4.2: Comparison of the maximum absolute values of the longitudinal mean velocity near the seabed for $x_{qu}/D = 6$ and different seabed distances.

4.2 shows the values obtained from the simulations where $x_{qu}/D = 6$, for both ferries. The results are in accordance with Figure 4.5, which tells that the minimum value of the longitudinal velocity is located near the seabed, and Figure 4.4, which says that the shorter the distance of the seabed from the propeller, the lower the values of the velocity are. In the table, the differences in percentage with the case $h_p/D = 0.9$ are shown, calculated with the formula:

$$\frac{\text{difference between the two cases}}{\text{value for } h_p = 0.9D} \times 100 \tag{4.3}$$

The benefits of enlarging the seabed clearance are evident: for the Lodi ship, by duplicating the distance, a decrease of -11.7% is obtained, and by triplicating it, the $|\bar{v}|_{b_{max}}$ is reduced by almost a quarter. The same trend is seen for the Wittow ferry, even if attenuated: the difference stops at -7.09% for the doubled distance and it is about than a fifth when tripled. The same quantity

x_{qu}/D [-]	Lodi: $\lvert\bar{v}\rvert_{b_{max}}/U$ [-]	Difference with case $x_{qu} = 6D$ [%]	Wittow: $\lvert\bar{v}\rvert_{b_{max}}/U$ [-]	Difference with case $x_{qu} = 6D$ [%]
6	0.291	-	0.296	-
8	0.254	-12.7	0.229	-22.6
11	0.191	-34.4	0.148	-50.0

Table 4.3: Comparison of the maximum absolute values of the longitudinal mean velocity near the seabed for $h_p/D = 0.9$ and different quay wall distances.

$|\bar{v}|_{b_{max}}$ is evaluated in Table 4.3, but for $h_p/D = 0.9$, changing the distances of the quay wall from the propeller. The percentages here are calculated as:

$$\frac{\text{difference between the two cases}}{\text{value for } x_{qu} = 6D} \times 100 \tag{4.4}$$

As already noted for the minimum longitudinal mean velocities in Figure 4.4, the advantages of moving the quay wall away are greater than those obtained by moving the seabed. Again,

this is even more evident for the Wittow ferry: for the Lodi ship, going from $x_{qu}/D = 6$ to $x_{qu}/D = 8$ means reducing $|\bar{v}|_{b_{max}}$ of -12.7%, while for the second boat the reduction is of -22.6%, so while the percentage of the Lodi case is similar to the one in Table 4.2, for the Wittow case the percentage is about three time larger. Moving from $x_{qu}/D = 6$ to $x_{qu}/D = 11$ instead produces a $|\bar{v}|_{b_{max}}$ smaller than -34.4% for the first boat, and halves it for the second boat.

4.1.2 Pressure and Shear Stress

This section is dedicated to the study of the time mean pressure, referred to as *mean pressure* $\bar{p}$, and of the time mean longitudinal component of the shear stress, called *mean longitudinal shear stress* $\overline{\tau_x}$, on the walls of the simulations. In particular, for the geometry used, the flux hits the quay wall perpendicularly, and for this reason the pressure is studied on the quay wall, while the shear stress is associated with the seabed due to the backflow in the lower part of the domain. The reference pressure p_0 is defined as:

$$p_0 = \frac{1}{2}\rho_w U^2 = 3150\ Pa \tag{4.5}$$

where ρ_w is water density $\rho_w = 1000\ kg/m^3$ and U is the circumferential velocity $U = 2.51$ m/s. Some considerations regarding where to expect the higher values of the mean pressure to be were already formulated previously in Section 4.1.1, specifically when explaining, in Figure 4.2 and Figure 4.5, the trajectory of $\bar{v}_{x_{max}}$ connected to the geometry of the hulls. In accordance with what is expected from the study of the velocity, Figure 4.6 shows that the highest values of $\bar{p}$ are located in the area right below the water surface, and they distribute homogenously in a convex shape. For the values in the upper area of the wall, no big differences among the highest values

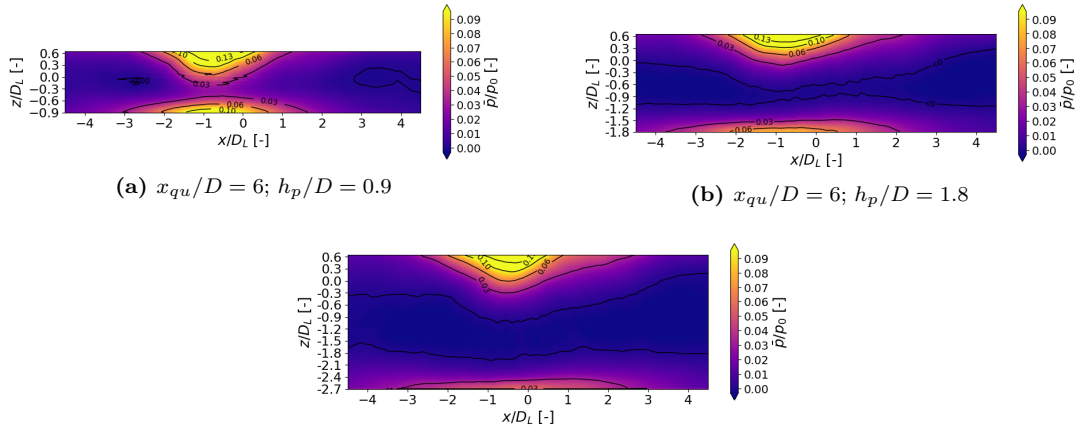

(a) $x_{qu}/D = 6$; $h_p/D = 0.9$

(b) $x_{qu}/D = 6$; $h_p/D = 1.8$

(c) $x_{qu}/D = 6$; $h_p/D = 2.7$

Figure 4.6: Lodi: contour of the mean pressure on the quay wall for different seabed distances.

seem to occur when changing the distance of the seabed (detailed values in the tables below). Comparing the case $h_p/D = 0.9$ to $h_p/D = 1.8$, the region where the pressure is higher than $\bar{p}/p_0 = 0.03$ increases, and this area grows even more when analyzing $h_p/D = 2.7$. Moreover, what the study of the velocity did not anticipate is the increment of the mean pressure also in the lowest part of the quay wall. In this part, on the contrary of what was said above, the values of the maximum mean pressure decrease when the bottom is lower. This could happen because,

when the seafloor level is lower, the flow arrives at the bottom with less intensity, therefore it produces a smaller pressure gradient. Regarding the mean pressure on the quay wall for different seabed distances for the Wittow ferry (Figure 4.7), according to what was found in Section 4.1.1, the highest values are found slightly under the water surface because of the deviation of the Wittow's hull. As for Figure 4.6, two different areas containing the peaks of the mean pressure

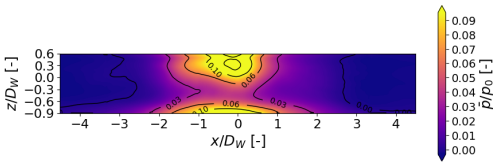

(a) $x_{qu}/D = 6$; $h_p/D = 0.9$

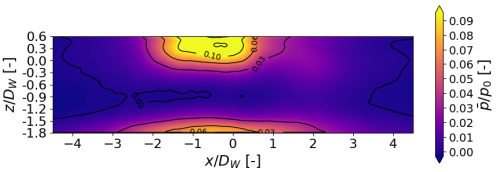

(b) $x_{qu}/D = 6$; $h_p/D = 1.8$

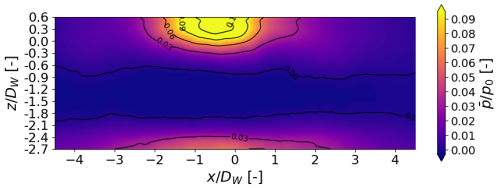

(c) $x_{qu}/D = 6$; $h_p/D = 2.7$

Figure 4.7: Wittow: contour of the mean pressure on the quay wall for different seabed distances.

are found, one at the top of the wall and one at the bottom. Again, in the upper part, no constant decrease in the value of the maximum mean pressure is found when moving away from the seabed, while for the lower part, the decrease is evident. Table 4.4 shows the comparison between the maximum value of the mean pressure over the quay wall. As seen in the previous images, duplicating or triplicating the distance from the VSP to the seabed does not bring any advantages: the maximum values oscillate around the reference values, without showing a trend.

h_p/D [-]	Lodi: $\bar{p}_{max}/p_0$ [-]	Difference with case $h_p/D = 0.9$ [%]	Wittow: $\bar{p}_{max}/p_0$ [-]	Difference with case $h_p/D = 0.9$ [%]
0.9	0.178	-	0.138	-
1.8	0.182	+2.25	0.130	-5.80
2.7	0.164	-7.87	0.146	+5.80

Table 4.4: Comparison of the maximum values of the mean pressure on the quay wall for Lodi and Wittow ferries for $x_{qu}/D = 6$ and different seabed distances.

Figure 4.8 and 4.9 show the pressure distribution for different wall clearances. Since the mean pressure is calculated on the quay wall, it was expected that, when moving that wall, the values would be lower than those obtained when moving the seabed. The pressure distribution is the same got for Figure 4.6 and 4.7, with two separated zones with the highest mean pressure: for the Lodi ferry one in the upper part of the wall and one wider but less intense in the lower, for the Wittow ferry one in the upper-central part and one weaker but more extended near the bottom. For the second boat, the case $x_{qu}/D = 11$ $h_p/D = 0.9$ is the one with the lowest values of the pressure, which does not even reach $\bar{p}/p_0 = 0.06$. Table 4.5 shows the comparison between the

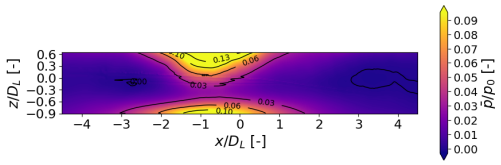

(a) $x_{qu}/D = 6$; $h_p/D = 0.9$

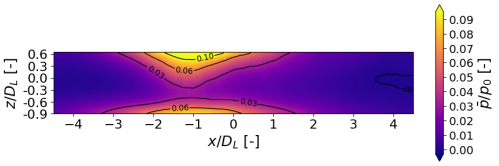

(b) $x_{qu}/D = 8$; $h_p/D = 0.9$

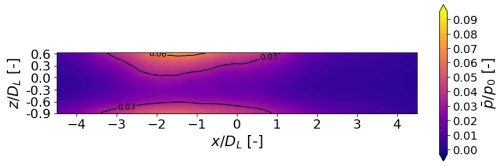

(c) $x_{qu}/D = 11$; $h_p/D = 0.9$

Figure 4.8: Lodi: contour of the mean pressure on the quay wall for different quay wall distances.

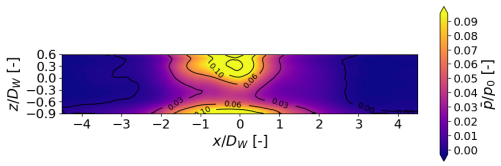

(a) $x_{qu}/D = 6$; $h_p/D = 0.9$

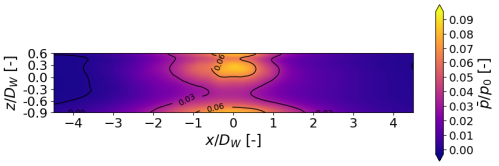

(b) $x_{qu}/D = 8$; $h_p/D = 0.9$

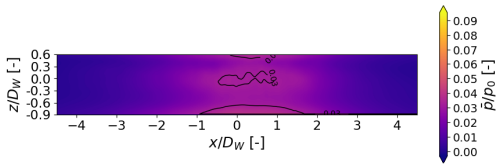

(c) $x_{qu}/D = 11$; $h_p/D = 0.9$

Figure 4.9: Wittow: contour of the mean pressure on the quay wall for different quay wall distances.

maximum value of the mean pressure for different distances from the quay wall. This time, the trend is evident: the maximum values can decrease up to -58.4 % for the Lodi ship and -71.7 % for the Wittow ship.

x_{qu}/D [-]	Lodi: $\bar{p}_{max}/p_0$ [-]	Difference with case $x_{qu}/D = 6$ [%]	Wittow: $\bar{p}_{max}/p_0$ [-]	Difference with case $x_{qu}/D = 6$ [%]
6	0.178	-	0.138	-
8	0.125	-29.7	0.083	-39.9
11	0.074	-58.4	0.039	-71.7

Table 4.5: Comparison of the maximum values of the mean pressure on the quay wall for Lodi and Wittow ferries for $h_p/D = 0.9$ and different quay wall distances.

The same kind of analysis was made for the distribution of the mean longitudinal shear stress on the seabed. This time, however, the adimensionalization was made by dividing for the threshold value for the erosion, equal to $|\tau_0| = 0.43\ Pa$ (the absolute value means that the direction depends on the flow stream); in this way, it is easier to understand where the scour happens. Since the flow is moving to the negative direction of the x-axis near the seabed, the direction of the longitudinal shear stress is mainly negative; therefore, the value of the erosion threshold is chosen as negative $\tau_0 = -0.43\ Pa$. The red line represents the contour for which $\overline{\tau_x} = \tau_0$, meaning that the area confined by this line is where the deterioration happens. The dashed black line is the location of the VSP. First, different bottom clearances are analyzed, maintaining the same distance from the quay wall. It is noticed that the higher values of $\overline{\tau_x}$ are located close to the vertical wall (Figure 4.10 and 4.11) because this region is where the backflow impacts. For both Lodi and Wittow ferries, for the case $x_{qu}/D = 6$ $h_p/D = 0.9$, there is a large area where the mean longitudinal shear stresses reach values higher than five times the threshold (more details on the maximum value in the tables below). For the Wittow ferry, however, the area

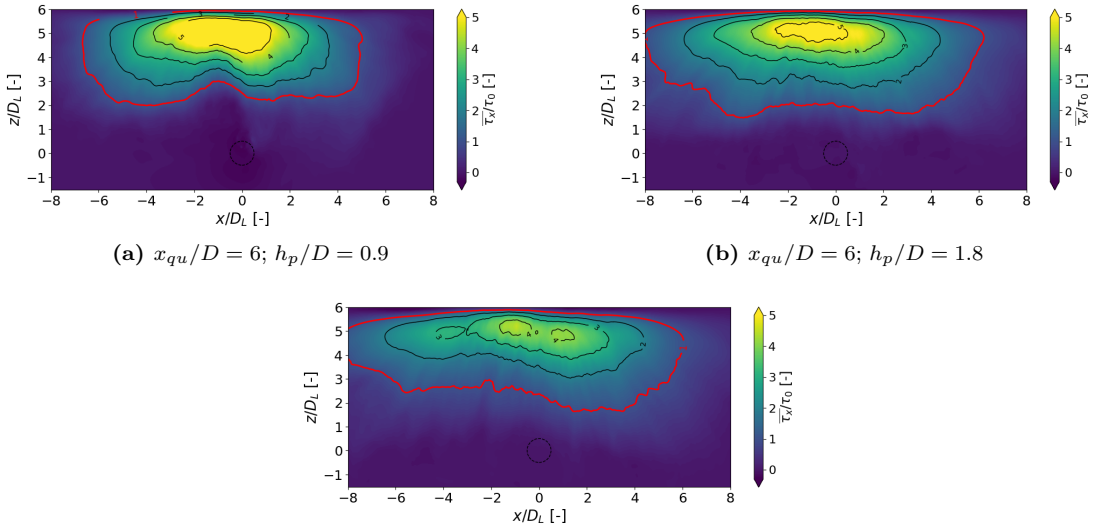

(a) $x_{qu}/D = 6$; $h_p/D = 0.9$

(b) $x_{qu}/D = 6$; $h_p/D = 1.8$

(c) $x_{qu}/D = 6$; $h_p/D = 2.7$

Figure 4.10: Lodi: contour of the mean longitudinal shear stress on the seabed for different seabed distances.

where the erosion happens is smaller than in the Lodi case. This could be associated, again, with the hollow in Wittow's hull, which confines the turbulent fluid to a smaller region. When moving away the seabed, the intensity of $\overline{\tau_x}$ diminishes, as expected. Table 4.6 shows the maximum value of the mean longitudinal shear stress $|\overline{\tau}_x|_{max}$ on the seabed (the absolute value is used because, since the direction is opposite compared to the x-axis, the values are negative, and the research would actually be for the minimum values). For the maximum values of $|\overline{\tau}_x|_{max}$, a decreasing trend can be seen for the Lodi ferry, but not so evident for the Wittow ferry, where only by triplicating the distance h_p/D a decrease of the maximum value is seen. However, when the seabed clearance increases to $h_p/D = 1.8$, the values get smaller, but the area affected by deterioration enlarges. The reason behind this could be that, by moving the seabed away, the turbulent flow has more space to develop, and, if its kinetic energy is still high, this could lead to a wider erosion of the seafloor. Table 4.7 shows the value of the area confined by the red line

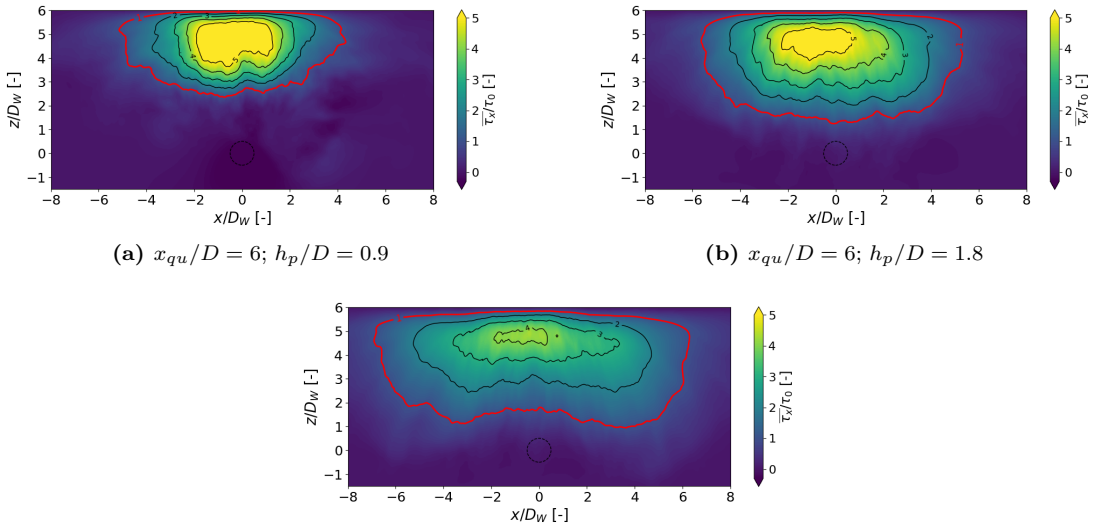

(a) $x_{qu}/D = 6$; $h_p/D = 0.9$

(b) $x_{qu}/D = 6$; $h_p/D = 1.8$

(c) $x_{qu}/D = 6$; $h_p/D = 2.7$

Figure 4.11: Wittow: contour of the mean longitudinal shear stress for different seabed distances.

h_p/D [-]	Lodi: $\lvert\overline{\tau_x}\rvert_{max}/\tau_0$	Difference with case $h_p/D = 0.9$ [%]	Wittow: $\lvert\overline{\tau_x}\rvert_{max}/\tau_0$	Difference with case $h_p/D = 0.9$ [%]
0.9	7.23	-	5.96	-
1.8	5.85	-19.1	6.06	+1.68
2.7	4.48	-38.1	4.30	-27.8

Table 4.6: Comparison of the maximum values in the negative x-direction of the mean longitudinal shear stress on the seabed for Lodi and Wittow ships for $x_{qu}/D = 6$ and different seabed distances.

(the region affected by the erosion). For the Lodi ferry, comparing the case $h_p/D_W = 1.8$ to

h_p/D [-]	Lodi: A/D_L^2 [-]	Difference with case $h_p/D = 0.9$ [%]	Wittow: A/D_W^2 [-]	Difference with case $h_p/D = 0.9$ [%]
0.9	38.3	-	25.3	-
1.8	49.0	+27.9	41.7	+64.8
2.7	43.1	+12.5	51.9	+105.1

Table 4.7: Comparison of the dimensions of the area affected by erosion for $x_{qu}/D = 6$ and different seabed distances.

$h_p/D_W = 2.7$, the area actually diminishes (the increase from $h_p/D_W = 0.9$ goes from +27.9% to +12.5%), but for the Wittow ferry, it keeps increasing, and the affected area doubles with respect to $h_p/D_W = 0.9$. Yet, the maximum values of the mean longitudinal shear stresses decrease.

When the bottom is kept at $h_p/D = 0.9$ and the wall clearance is increased, something unexpected happens: while calculating the mean pressure on the vertical wall, it was predictable that, when moving that wall, more effective results would have been obtained compared to the

shifting of the seabed. Here, however, still better values are obtained when moving the quay walls and not the bottoms, which is counterintuitive since $\overline{\tau_x}$ is analyzed on the bottom. Figure 4.8 and 4.9 show clearly this phenomenon, which happens regardless of the geometry of the hull. Again,

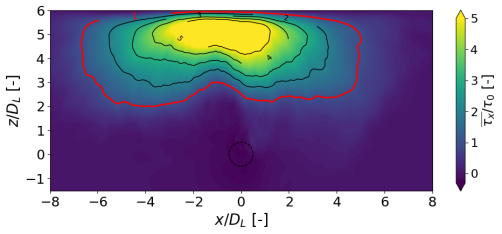

(a) $x_{qu}/D = 6$; $h_p/D = 0.9$

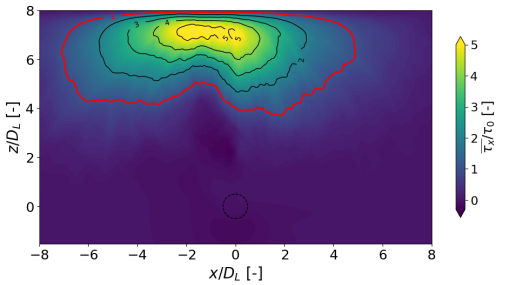

(b) $x_{qu}/D = 8$; $h_p/D = 0.9$

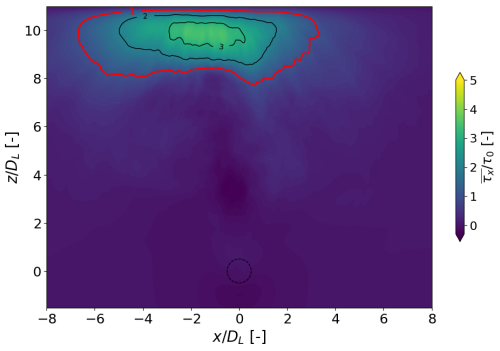

(c) $x_{qu}/D = 11$; $hp/D = 0.9$

Figure 4.12: Lodi: contour of the mean longitudinal shear stress on the seabed for different quay wall distances.

smaller overall values are obtained for the second ship, and the case $x_{qu}/D_W = 11$ $h_p/D_W = 0.9$ is the one with the smallest erosion area among all the combinations studied. Table 4.8 shows the maximum value of the mean longitudinal shear stress for different quay wall distances. For

x_{qu}/D [-]	Lodi: $\lvert\overline{\tau_x}\rvert_{max}/\tau_0$	Difference with case $x_{qu}/D = 6$ [%]	Wittow: $\lvert\overline{\tau_x}\rvert_{max}/\tau_0$	Difference with case $x_{qu}/D = 6$ [%]
6	7.23	-	6.96	-
8	5.53	-23.5	4.40	-34.2
11	3.53	-51.2	2.01	-70.0

Table 4.8: Comparison of the maximum values in the negative x-direction of the mean longitudinal shear stress on the seabed for Lodi and Wittow ships for $h_p/D = 0.9$ and different quay wall distances.

this case, a coherent decrease of the values is experienced, and it is even more marked for the Wittow ferry, reaching a diminution of -70.0%. Table 4.9 displays clearly the benefit that moving the quay walls has; while in Table 4.7 the areas were increasing for all the combinations, for this

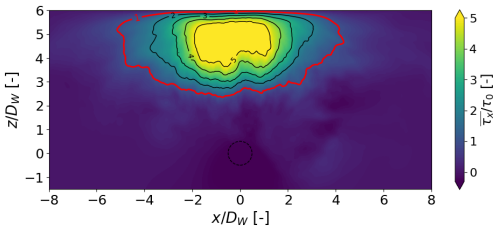

(a) $x_{qu}/D = 6$; $h_p/D = 0.9$

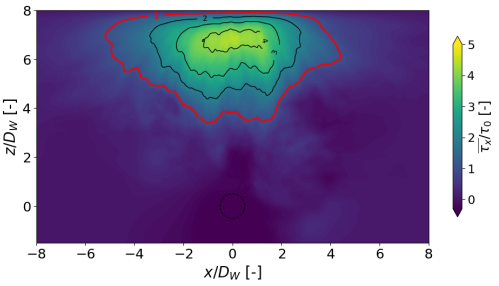

(b) $x_{qu}/D = 8$; $h_p/D = 0.9$

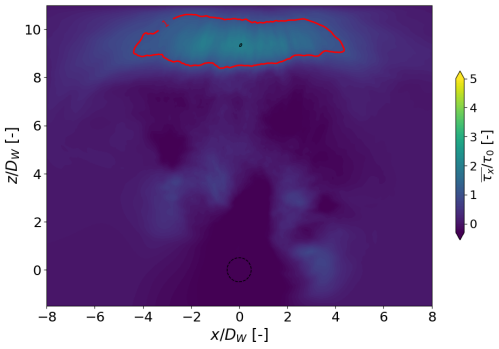

(c) $x_{qu}/D = 11$; $h_p/D = 0.9$

Figure 4.13: Wittow: contour of the mean longitudinal shear stress on the seabed for different quay wall distances.

case a small increment is seen when passing from $x_{qu}/D = 6$ to $x_{qu}/D = 8$ (only +0.52% for the Lodi ferry), and a significant decrease for the case $x_{qu}/D = 11$ is experienced, underling once again the benefit of choosing the wall clearance as the main parameter for the analysis of the erosion caused by this type of propellers.

x_{qu}/D [-]	Lodi: A/D_L^2 [-]	Difference with case $x_{qu}/D = 6$ [%]	Wittow: A/D_W^2 [-]	Difference with case $x_{qu}/D = 6$ [%]
6	38.3	-	25.3	-
8	38.5	+0.52	29.1	+15.0
11	23.5	-38.6	13.4	-47.0

Table 4.9: Comparison of the maximum values of the mean pressure on the quay wall for Lodi and Wittow ferries for $h_p/D = 0.9$ and different quay wall distances.

4.1.3 Fourier transforms of the pressure

When studying the frequencies that a marine propeller produces, variations of the propeller field might lead to destructive phenomena such as noise, vibrations and cavitation. This type of analysis translates the pressure from the time domain into the frequency domain, so it is possible to identify the dominant frequencies, which can be dangerous for the ship structure. The Fast Fourier Transform (FFT), an algorithm that computes the Discrete Fourier Transform (DTF), is used for this purpose, reducing the number of operations from $O(N^2)$ of the DTF to $O(N \log(N))$. To calculate the FFT of the pressure, six probes are positioned:

- *below propeller*: (0.0, 0.0, $-\lambda L_{B,L}$), where L_B corresponds to the length of the blade (1.1 m for Lodi ferry 3.1) and λ is the scale factor
- 1D: (λD, 0.0, 0.0), where D is the orbital diameter of the VSP
- 2D: ($2\lambda D$, 0.0, 0.0)
- 3D: ($3\lambda D$, 0.0, 0.0)
- 4D: ($4\lambda D$, 0.0, 0.0)
- 5D: ($5\lambda D$, 0.0, 0.0)

The probes were positioned for the Lodi ferry simulations, in particular for the unrestricted case and for the case $x_{qu}/D_L = 6$ $h_p/D_L = 0.9$. Figure 4.14 shows the position of the probes for

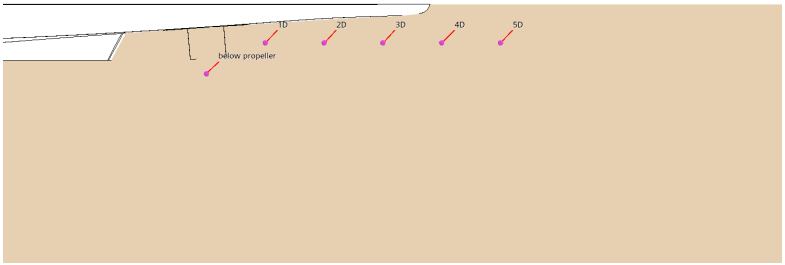

Figure 4.14: Probes location for the unrestricted case.

the case without restriction, but the locations remain the same also for the confined case. The simulations were then run for 20 more full rotations of the propeller.
For this analysis, the FFTs are computed for the pressure, which varies, together with the shear stress, responsible for the surface forces (Eq. 2.23 and 2.31), and for the propagation of acoustic waves. In this section, the instantaneous pressure is calculated for each probe in relation to the time, and then this relationship is translated, using the FFT, into a correlation between the pressure amplitude and its constituent frequency. Two important frequencies are expected to be seen (as well as their harmonics):

- *Fundamental Shaft Frequency (FSF)*: represents the rotation of the VSP and depends only on the rotation rate n_p. It is calculated as:

$$f_s = \frac{n_p}{2\pi} = 6.095 \ s^{-1} \tag{4.6}$$

- *Blade Passing Frequency (BPF)*: frequency with which the blades pass in front of a probe. It is a function of the number of blades:

$$f_{BPF} = 5 \times \frac{n_p}{2\pi} = 30.475 \ s^{-1} \tag{4.7}$$

Unrestricted Case

First, the results for the open-sea simulation of the Lodi ferry are analyzed. Figure 4.15 shows the dimensional outcome from the probes' records. Below the propeller, the pressure reaches peak

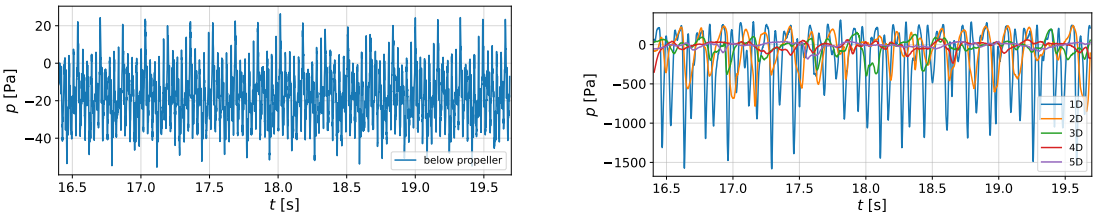

(a) Probe below the propeller

(b) Probes 1D, 2D, 3D, 4D, 5D

Figure 4.15: Pressure over time calculated for (a) a probe below the propeller and (b) probes at different distances from the propeller.

values of 20 Pa, while the inferior values go as low as -50 Pa, and both extremes repeat themselves with a period of 0.17 s circa (corresponding to the FSF $1/0.17 \approx f_s$), while the smallest peaks have a period of about 0.033 s (corresponding to $1/0.033 \approx f_{BPF}$). Meanwhile, for the probes far from the VSP, the pressure reaches lower peaks much smaller than the previous case. As expected, the closer the data extrapolated are to the propeller, the smaller the values become: the lowest pressure values of the 1D probe are twice smaller than the 2D probe, and the 5D probe, compared to the 1D, has values very close to 0. For this data, in the first second, the period for the 1D and 2D probes seems to be similar to the below propeller probe; however, as the simulation proceeds, a period is not detected anymore. To translate the simulation results, the data are transformed using the Fast Fourier transform. The outcome, in Figure 4.16, shows that the amplitude of the signal depends on the frequency. For the below propeller probe, the amplitudes, in accordance with the previous figure, are small. The first peak, at 0 Hz, the highest one, represents the average pressure field generated by the propeller, equal to -17.5 Pa (it is negative because Fig. 4.15 shows that the average value is negative). The second highest peak is the BPF Eq. 4.7, and the amplitudes shown in between are the FSF at 6 Hz Eq. 4.6 and its harmonics. The peaks after the BPF are the harmonics of the FSF and of the BPF (at 60 Hz and 90 Hz). The multiples derive from the non-linearity of the hydrodynamic load, and if their amplitudes reach high values, they can be dangerous as well. The main purpose of studying these frequencies is to avoid destructive phenomena from happening: if the frequencies correspond to the natural frequency of one of the ship components, the structural resonance can occur and amplify the vibrations; pressure oscillations can lead to cavitation phenomena and consequently wear and tear of metals; for discrete frequencies, the noise produced can travel for long distances under water, and can interfere with the passengers' comfort or not satisfying the underwater noise regulations. The low frequencies can travel far more, but the high frequencies (the harmonics) involve high energy levels and more concentrated forces. For the probe below the propeller, the amplitudes are small, therefore not concerning; however, for the probes in the VSP wake, the values they reach are very high and can cause problems. As expected, the flow is more chaotic

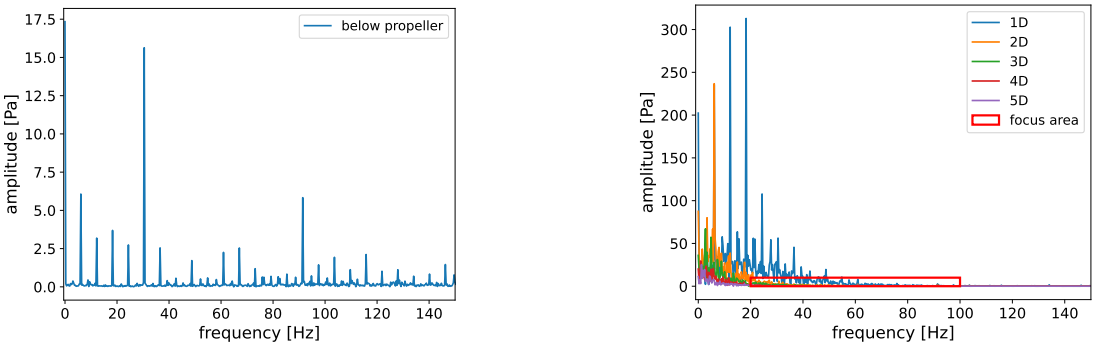

(a) Probe below the propeller

(b) Probes 1D, 2D, 3D, 4D, 5D

Figure 4.16: Fourier transform of the pressure for (a) a probe below the propeller and (b) probes at different distances from the propeller.

in the wake and consequently less repetitive, as shown in the Figure 4.16b. For the 1D probe, the average pressure is about -200 Pa, for the 2D probe, it is around -90 Hz and it gets closer to zero for the farther probes. In this case, the FSF harmonics are prevalent: the yellow peak is exactly the FSF, and the following blue spikes correspond to 2FSF, 3FSF, and 4FSF. The irregular spectrum for the lower frequencies appears because the flow is turbulent; therefore, different frequencies are displayed, especially for the data obtained close to the propeller. For farther measurements, the interference is less evident. The BPF does not emerge at first glance; however, the zoomed section shown in Figure 4.17 shows that its multiples appear, but with very low intensity. The trend in Figure 4.17 can be explained by the fact that for lower frequencies,

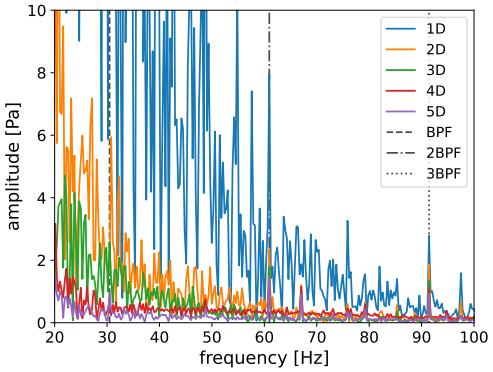

Figure 4.17: Zoomed section of Figure 4.16.

where the value of BPF is, the turbulence of the flow has a strong impact on the spectrum, while the higher frequencies survive, even if with small amplitudes. In the turbulent field, however, the frequencies of the propeller dominate, reaching dangerous values; therefore, more attention needs to be paid to them.

Restricted case: $x_{qu}/D_L = 6$ $h_p/D_L = 0.9$

For the restricted case, the same procedure is applied, and Figure 4.18 shows the result obtained from pressure measurements. In contrast to Figure 4.15, for the below propeller probe, no higher

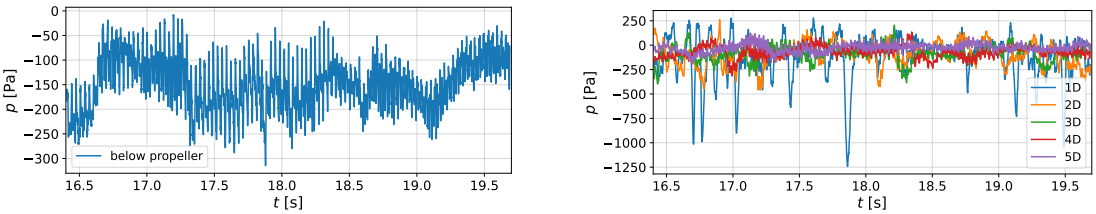

(a) Probe below the propeller

(b) Probes 1D, 2D, 3D, 4D, 5D

Figure 4.18: Pressure over time calculated for (a) a probe below the propeller and (b) probes at different distances from the propeller.

peaks prevail (Figure 4.18a, and the period of the spikes with similar amplitude corresponds to circa 0.033 s, which, as seen before, is related to the BPF. In this case, the lowest value reaches -300 Pa and the pressure calculated at this point is never positive; therefore, a lower average pressure is expected. In Figure 4.18b, for the probes near the VSP, no clear period is detected; however, for the 4D and 5D probes, the period corresponding to BPF is seen, and therefore it is expected to be seen also in the FFT graph. Again, the frequency of the FSF is not shown. The 1D probe has the most diverse values, reaching up to -1250 Pa, while the range of the other probes goes from -400 Pa to 250 Pa. The outcome of the FFT, in Figure 4.19, shows that the FSF, as anticipated above, is not detected in any of the probes, and the BPF and its harmonics are well defined. Below the propeller (Figure 4.19a), the average pressure is around -150 Pa. After that

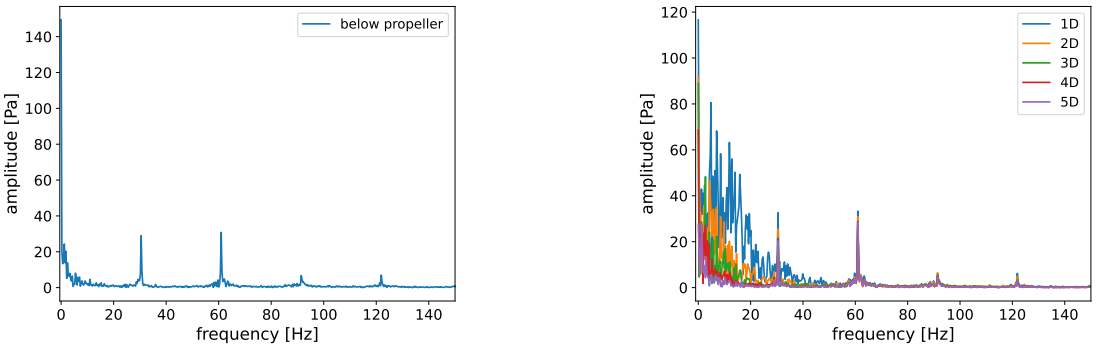

(a) Probe below the propeller

(b) Probes 1D, 2D, 3D, 4D, 5D

Figure 4.19: Fast Fourier transform of the pressure for (a) a probe below the propeller and (b) probes at different distances from the propeller.

peak, two others emerge: the BPF and 2BPF, with amplitudes of approximately 30 Pa. Also, the 3BPF and 4BPF are seen, but their amplitudes are lower than 10 Pa. Compared to Figure 4.16a, the values are generally much higher, and that could be because the flow, due to the walls, comes back, so the turbulence influences also this point in the space, that in the case without

restrictions was not touched by the wake. In Figure 4.19b, a similar pattern is recognized, and the amplitudes of the peaks decrease as the data are taken farther from the VSP. Moreover, as in Figure 4.16b, a disturbance for lower frequencies is seen, and it reduces when the measurements are distant from the propeller. The difference between the FFTs of the two cases, specifically the fact that for the restricted case only the BPF is seen, might be explained by the fact that the presence of the walls reflects the flow back, and by doing so they break the symmetry of the flow field. The pressure detected by the probes in this case is given by the sum of the direct flow and the reflected flow, and might lead to a cancellation of the FSF and to higher values of the BPF. Consequently, the lower frequencies are not detected anymore (the FSF and its harmonics), and only the BPF and its multiples are visible. However, to validate these hypotheses, more simulations need to be run, with different parameters, for example changing the positions of the walls and of the probes, using another rotation rate or a different number of blades.
For this type of analysis as well, a direct comparison with the literature regarding the frequencies produced by VSPs or cycloidal propellers in general is not possible, since no material is found on this matter. However, some publications treat a similar investigation but for other kinds of propellers: Wei and Chiew [61] identify the dominant frequency of a fixed pitch propeller using different wall clearances, Nazeer et al. [62] studied the impact that the BPF and its harmonics have on flow separation for a fixed pitch propeller, and Feng and Lu [63] showed that a probe above the propeller contains the first the harmonics of the BPF, while a probe on the wake captures only the BPF.

4.2 Scale effect

It is well known that, when choosing the non-dimensional number with respect to which to do a fluid dynamics similarity, not all physical quantities are correctly scaled. For this reason, a thoughtful choice is needed, and the motivations behind the Froude similarity are explained in Section 3.4. In this part of the analysis of the results, the roughness height r of the seabed is changed to study whether better outcomes are obtained by increasing its value; in particular, the comparison is carried out between the same value of r of the model scale, and the value obtained by scaling r as a length, multiplying it by the scale factor $\lambda = 16$. In this section, only the case $x_{qu} = 6D_L$ $h_p = 0.9D_L$ of the Lodi ferry is used, so that the simulations analyzed are:

- Model scale 1:16: $r = 0.8\ mm$
- Full scale: $r = 0.8\ mm$
- Full scale: $r = 0.8\lambda = 12.8\ mm$

This study follows the same outline as Section 4.1: first, the velocity field is investigated, with particular focus on values near the bottom; subsequently, the mean pressure on the quay wall and the longitudinal mean shear stress are investigated.

4.2.1 Velocity field

Figure 4.20 shows the velocity profiles drawn, for the $x/D_L \in \{1,2,3,4,5\}$, taking the y-coordinate of the point for that x-section where the maximum value of the *mean longitudinal velocity* is found. For each point individuated, then, its profile is drawn along the z-axis. The full scale lengths are divided by $D_L = 2.1\ m$ and the velocities by $U = 10.05\ m/s$, while the model scale results are obtained by dividing the length by the scaled diameter $D_L/\lambda = 0.13125\ m$ and the velocities by $U\lambda^{0.5} = 2.51\ m/s$, with $\lambda = 16$. In this way, it is possible to put all the results in

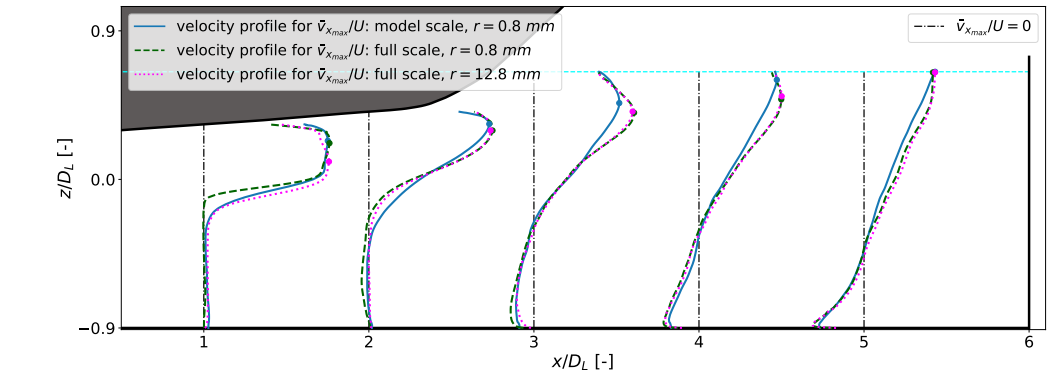

(a) Velocity profiles

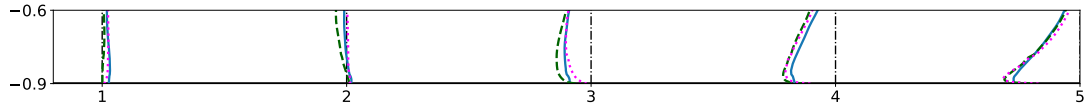

(b) Zoomed section

Figure 4.20: (a) Velocity profiles of the mean longitudinal velocity for the different seafloor roughness and (b) a zoomed picture near the seabed.

the same graph. In Figure 4.20, the full scale simulation profile for $r = 12.8\ mm$ is closer to the model scale profiles for the section $x/D_L = 1$; however, when looking at the z-coordinate of the point with the maximum velocity, the value is nearer to the full scale case with $r = 0.8\ mm$. For the profiles of the other x-sections, the two full scale results evolve together, marking a noticeable difference with the model scale. Nevertheless, since the roughness height of the seabed changes, the distinctions in the velocities are expected to be in the lower part of the domain, and this is the reason why a close-up of the velocity near the bottom is made. From the zoomed-in view in Figure 4.20b, it is clear that the full scale $r = 12.8\ mm$ case is the one that better matches the model scale, especially for the x-sections $x/D_L = 1$, $x/D_L = 2$ and $x/D_L = 3$. When the profiles get closer to the quay wall, the two full scale simulations give almost the same results, so it cannot be said which one is better. Figure 4.21 shows the minimum and maximum values that the mean longitudinal velocity $\bar{v}_x$ reaches for every considered x-section. The values obtained for the two full scale simulations are, as expected, very similar: in the graph with the maximum values Figure 4.21a, both of them show a discrepancy with the model scale; however, $r = 12.8\ mm$ is slightly lower than $r = 0.8\ mm$ and therefore it better approximates it. For the section $x/D_L = 5$, the $\bar{v}_{x_{max}}$ are very close, but this is because the points with the maximum values are all on the water surface. In the graphs with the minimum values in Figure 4.21b, however, all the three simulations get very close numbers, and they have the same linear decreasing trend, meaning that the strength of the backflow is similar for the three cases. Figure 4.22 shows the positions of the points with the maximum and minimum value of $\bar{v}_x$ in the x-z plane. Here again, the case $r = 12.8\ mm$ seems to be closer to the model case, especially when looking at the locations of $\bar{v}_{x_{min}}$ for the x-sections $x/D_L = 1$, $x/D_L = 2$ and $x/D_L = 3$, while in sections $x/D_L = 4$ and $x/D_L = 5$ the three points are overlapping. The points of the full scale simulations associated to $\bar{v}_{x_{max}}$ follow the almost same path, apart from section $x/D_L = 1$, where the case $r = 0.8\ mm$ is closer to the model scale, and section $x/D_L = 4$, where the case $r = 12.8\ mm$ is marginally closer

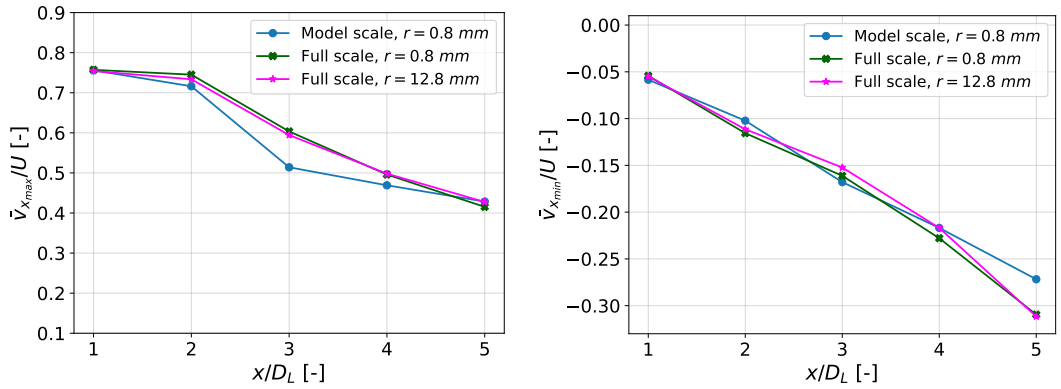

(a) Maximum values **(b)** Minimum values

Figure 4.21: Maximum (a) and minimum (b) values of the mean longitudinal velocity for different x/D sections.

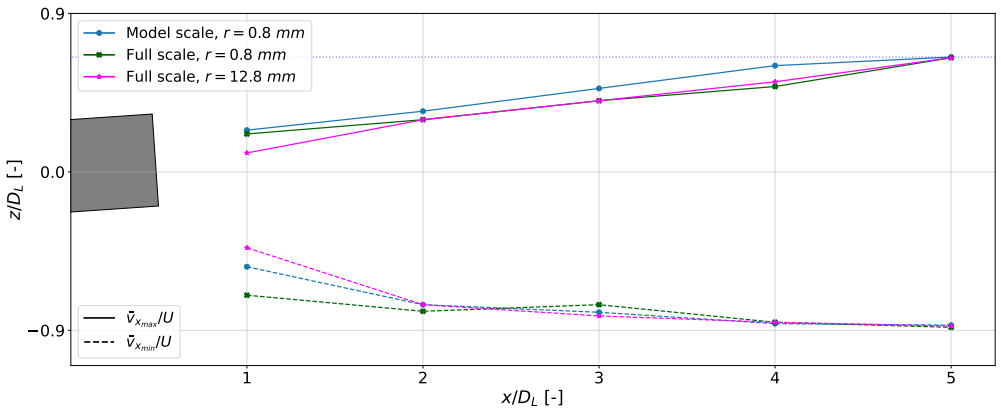

Figure 4.22: Section of the x-z plane showing the position of the points with the maximum and minimum values of the mean longitudinal velocity in different x/D sections.

to the model scale. Consequently, the maximum absolute values of the longitudinal mean velocity are studied, calculated on a x-y plane located at one hundredth of the distance from the seabed to the centre of the propeller above the seabed (Table 4.10). For the full scale simulations, the velocities are normalized with respect to their value of U, as well as the model scale velocities for their reference velocity. From the table, it is clear that the model scale simulation overestimates the real $|\bar{v}|_{b_{max}}/U$, for both the roughness heights used. In fact, a higher r brings to a bigger gap between the model and the full scale, and this could be due to the fact that a higher roughness is associated with a greater attenuation of the backflow. So, while from the previous images, the $r = 12.8\ mm$ case appeared to better match the velocity field, from Table 4.10 the choice seems not to be so obvious.

Case	$\lvert\bar{v}\rvert_{b_{max}}/U$ [-]	Difference with the model [%]
Model scale, $r = 0.8\ mm$	0.291	-
Full scale, $r = 0.8\ mm$	0.236	-18.9
Full scale, $r = 12.8\ mm$	0.216	-25.8

Table 4.10: Comparison of the maximum absolute values of the longitudinal mean near the seabed.

4.2.2 Pressure and Shear Stress

The mean pressures on the quay walls are compared. Figure 4.23 shows the contours obtained by dividing the mean pressure by the reference pressure, which is p_0 for the full scale and p_0/λ for the model scale. The results show that the two full scale simulations display higher values of

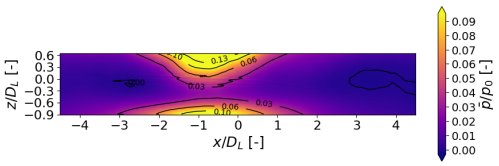

(a) Model scale, $r = 0.8\ mm$

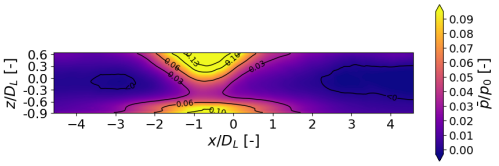

(b) Full scale, $r = 0.8\ mm$

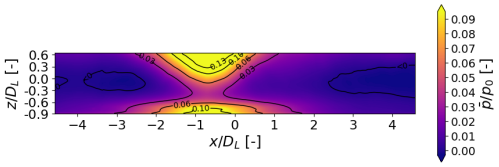

(c) Full scale, $r = 12.8\ mm$

Figure 4.23: Contour of the mean pressure on the quay wall for (a) model scale simulation and (b)(c) full scale simulations.

the mean pressure overall, and this is evident especially when looking at the center of the wall contour line for which $\bar{p}/p_0 = 0.03$, and at the top of the wall for the black line corresponding to $\bar{p}/p_0 = 0.13$, meaning that the area where the values are the highest is wider for the full scale. No big differences are noticed when comparing the two full-scale simulations, apart from the area where the pressure is negative and the one near the bottom, where $\bar{p}/p_0 = 0.10$. This was expected, since the only thing that changes between the two simulations concerns the seabed and not the quay wall directly. Figure 4.24 shows the plot of the longitudinal mean shear stresses $\overline{\tau_x}$ on the seabed. The τ_0, for the full scale, was calculated as the value used for the model scale $\tau_0 = 0.43\ Pa$ multiplied by $\lambda = 16$. The model scale contour reveals a larger scour zone compared to the full scale, and, in general, higher values of $\overline{\tau_x}$, and this can be seen by comparing how big the areas enclosed by every level are. When studying $\overline{\tau_x}$, the comparison between the two model scale simulations can also be made, and it shows that the shear stresses obtained for $r = 12.8\ mm$ are larger than the ones for $r = 0.8\ mm$, as well as the area affected by the erosion is larger (Table

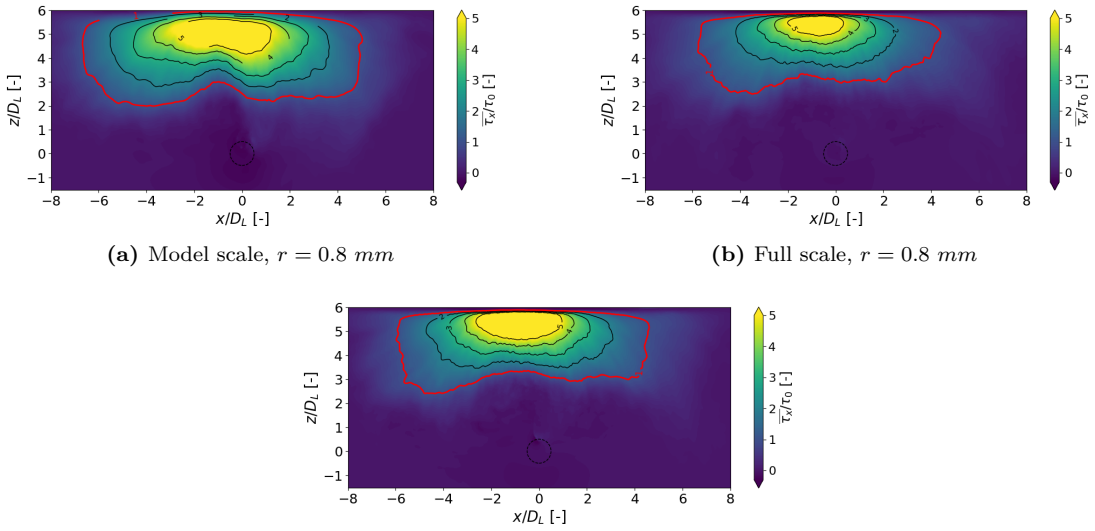

(a) Model scale, $r = 0.8\ mm$

(b) Full scale, $r = 0.8\ mm$

(c) Full scale, $r = 12.8\ mm$

Figure 4.24: Contour of the mean longitudinal shear stress on the seabed for (a) model scale simulation and (b)(c) full scale simulations.

4.12 for more details). This could happen because a stronger roughness height coefficient creates higher shear stresses; therefore, it is easier for them to reach the threshold and generate erosion. The comparison between the maximum value of the mean pressure on the quay wall $\bar{p}_{max}$ and of the longitudinal mean shear stress $|\overline{\tau_x}|_{max}$ is shown in Table 4.11. Regarding $\bar{p}_{max}$, no big

Case	$\bar{p}_{max}/p_0$ [-]	Difference with the model [%]	$\lvert\overline{\tau_x}\rvert_{max}/\tau_0$	Difference with the model [%]
Model scale, $r = 0.8\ mm$	0.178	-	7.23	-
Full scale, $r = 0.8\ mm$	0.177	-0.56	6.98	-3.46
Full scale, $r = 12.8\ mm$	0.185	+3.93	9.23	+27.7

Table 4.11: Comparison of maximum mean pressure on the quay wall and of the maximum values in the negative x-direction of the mean longitudinal shear stress on the seabed.

differences are shown: the case $r = 0.8\ mm$ has almost same value as the model scale. However, the $r = 12.8\ mm$ case does not differ more than +4% from it, so that the approximation is still completely acceptable. Yet, when looking at $|\overline{\tau_x}|_{max}$, the difference is evident: while the value of the case $r = 0.8\ mm$ is close to the model scale, the value of $r = 12.8\ mm$ is bigger than one fourth compared to it. Table 4.12 compares the dimensions of the region affected by erosion for the three cases: for both cases, as seen in Figure 4.24, the area of the model scale simulation is bigger than that of the full scale simulations, with slightly better results for $r = 12.8\ mm$. However, it needs to be taken into consideration that, for $r = 12.8\ mm$, the reference value τ_0 was scaled as a pressure, even if the scaling applied to Froude similarities does not work for viscous

Case	A/D_L^2 [-]	Difference with the model [%]
Model scale, $r = 0.8\ mm$	38.3	-
Full scale, $r = 0.8\ mm$	25.7	-32.9
Full scale, $r = 12.8\ mm$	28.6	-25.3

Table 4.12: Comparison of the maximum absolute values of the longitudinal mean near the seabed.

forces. Therefore, the results obtained should not be taken as proof that one roughness height works better than the other.

This analysis was made in the hope of finding a solution to the scale problem regarding the friction forces in the Froude similarity. Two different roughness height were use, but at the end, none of them shows significantly better results than the other: regarding the velocities profiles of the longitudinal mean velocity, the points with its maximum value in the x/D_L sections, the shear stresses contours, and the area affected by erosion, the case $r = 12.8\ mm$ has the results closer to the model scale; meanwhile, when looking at the maximum values of the velocity near the bottom, the pressure on the quay wall, and the shear stress on the seabed, the case $r = 0.8\ mm$ is the best one. Therefore, simply changing the roughness of a surface does not make the scale effect disappear; however, this study can be useful if a specific parameter is analyzed, and not the whole fluid dynamic study.

Chapter 5

Conclusions

Voith-Schneider propellers are a marine propulsion system commonly used in many different types of vessels. However, the consequence of their use regarding the erosion they could generate is not yet properly addressed.
In this study, two real operating ferries, equipped with VSPs, are taken as models to analyze the destructive effect that this type of marine propeller has on the quay walls and seafloors. To do so, a CFD analysis is conducted, using an IDDES turbulence model and an overlapping grid technique to simulate the rotation of the propeller mesh over the hull mesh. The simulations are run using a Froude similarity, which is the most appropriate for these types of problems. Three different wall clearances and seafloor clearances are taken into account, resulting in a total of five different combinations, as well as the open-sea case.
The analysis of the velocity field shows that the geometry of the hull plays an important role, deflecting the fluid when a hollow in the hull is present. Dividing the domain into equally spaced vertical sections, the maximum positive values of the velocity are located on the water surface, while the maximum negative values appear right above the seabed, due to the flow coming back after hitting the vertical wall. The maximum positive velocity in each vertical section is not affected by the presence of the walls, whereas the maximum negative velocity is influenced by them. Lower absolute values of the negative velocity are observed in regions where the confinements are located closer to the propeller. When the walls are further from the VSP, the maximum negative value of the velocity near the bottom gets smaller, especially for high wall clearances, meaning that the vertical restriction is the one that mostly impacts the backflow.
The predominant influence of the wall clearance over the seabed clearance is confirmed when studying the pressure on the vertical wall and the shear stresses on the horizontal wall: in both cases and for both ships, smaller values of the two variables are obtained when the quay wall gets further away, rather than the seafloor. Also, the maximum value of the pressure on the quay wall is not affected by the distance from the bottom, while the maximum value of shear stress in the negative direction on the seafloor is more influenced by the vertical rather than the horizontal wall distance. Lastly, the area affected by erosion diminishes only when the quay wall is moved away from the VSP while the seafloor remains in the same position: if only the seabed clearance is increased, the turbulent flow impacts a larger surface, thus the eroded region is wider. It needs to be taken into consideration that the values used for x_{qu}/D are much bigger than the ones of h_p/D, therefore the prevalence of the distance to the quay wall might be strictly related to the larger space. Consequently, further analysis should be carried out to confirm or deny the predominance of one parameter over the other. The articles discussing this matter for other types of propellers (for example [64][30][45]) suggest a reference case in which only the seabed clearance

is considered, without any vertical walls involved. The comparison between the restricted and unrestricted cases was also carried out by computing the pressure in different parts of the domain. For the same position of the probes, the unconfined simulation shows the FSF, as well as the BPF, while for the confined domain, only the BPF is detected. The reason behind that was found in the reflection of the flow caused by the walls, which might cancel the FSF and enhance the amplitude of the BPF.
The decision of using a scaled geometry (and therefore the Froude similarity) inevitably brings some complications when addressing the friction forces. For this reason, two different roughness coefficients are examined on the seabed for the full-scale simulation. The comparison is made following the same pattern as above. However, none of them shows an overall better match with the model scale simulation; therefore, significant attention has to be paid when using the model scale.

5.1 Future work suggestions

Even if the distances from the walls are chosen in accordance with the literature, more intermediate lengths can be selected for a more accurate study. Moreover, other variables can be investigated, such as the instantaneous value of the velocity and pressure, the vorticity, and the turbulent kinetic energy, whose information can provide more details on the internal mechanism of the fluid, rather than looking at its mean value. Moreover, simulations that use different types of sediments should be run to add to the study other relevant quantities, such as the maximum scour depth and the maximum deposition height. Finally, with a more complete understanding of the problem, empirical relationships to predict the scour might be discovered, and they may substitute the current correlations used when working with these propellers.
Regarding the scale effect, the best solution would be to run the full-scale simulations directly. However, this solution is often not applicable because a greater computational cost is required. An option to overcome the problem could be to test different wall functions and turbulence models to find the best combination.

Appendix A

Set Up

A.1 Mesh

A.1.1 Lody ferry, full scale

Table A.1: Background domain mesh, default controls.

Base Size	1.810193359837562 m
Target Surface Size	100% of Base Size
Minimum Cell Size	100% of Base Size
Number of Prism Layers	12
Prism Layers Stretching	1.3
Prism Layer Total Thickness	0.11194275029503913 m
Default/Surface Growth Rate	2 Growth Layers
Maximum Cell Size	100% of Base Size

Table A.2: Blades mesh, default controls.

Base Size	0.05656854249492381 m
Target Surface Size	100% of Base Size
Minimum Cell Size	100% of Base Size
Number of Prism Layers	5
Prism Layers Stretching	1.3
Prism Layer Total Thickness	0.010625645177781421 m
Default/Surface Growth Rate	2 Growth Layers
Maximum Cell Size	100% of Base Size

Table A.3: Number of cells, faces and vertices for both simulations $x_{qu} = 6D_L$, $h_p = 0.9D_L$, $r = 0.8mm$ and $r = 12.8mm$ meshes.

Domain	Cells	Faces	Vertices
Background domain	4 802 135	14 330 301	5 054 434
Blade 1	172 888	521 316	192 170
Blade 2	172 888	521 316	192 170
Blade 3	172 888	521 316	192 170
Blade 4	172 888	521 316	192 170
Blade 5	172 888	521 316	192 170

Table A.4: Meshing parameters of the domain.

Part	Surface Remeshing	Prism Layer	Minimum Surface Size
Domain: Top Surface	`Disabled`	`Disabled`	100 %
Domain: Side Surfaces	`Disabled`	`Disabled`	100 %
Domain: Inlet Surface	`Disabled`	`Disabled`	100 %

Table A.5: Meshing parameters refinements (background): mesh control on a surface.

Part	Surface Remeshing: Target Surface Size	Prism Layer Total Thickness	Minimum Surface Size
Quay Wall	6.25 %	0.22744383591640185 m	6.25 %
Seabed	6.25 %	0.22744383591640185 m	6.25 %
Ship: Hull Side	12.5 %	`Default`	12.5 %
Ship: Hull Bottom	12.5 %	`Default`	12.5 %
Ship: Bow	1.5625 %	`Disabled`	0.78125 %
Ship: Skeg Bottom	3.125 %	`Default`	1.5625 %
Ship: Skeg Front	1.5625 %	`Default`	0.78125 %
Ship: Skeg Sides	3.125 %	`Default`	1.5625 %

Table A.6: Meshing parameters refinements (blades): mesh control on a surface.

Part	Surface Remeshing: Target Surface Size	Prism Layer Total Thickness	Minimum Surface Size
Blade	25 %	`Default`	25 %
Area around the top of the blade	`Default`	`Default`	`Default`
Area around the top of the blade with prism layers	3200%	0.11194275029503913 m	3200%
Interface Casing Rotor-Blades	100 %	`Disabled`	100 %

Table A.7: Meshing parameters refinements (blades): mesh control inside a closed volume.

Part	Trimmer: Customize Isotropic Size	Prism Layer Total Thickness
Blade: Leading Edge	12.5 %	0.010625645177781421 m
Blade: Tip	12.5 %	0.010625645177781421 m
Blade: Trailing Edge	12.5 %	0.010625645177781421 m

A.1.2 Lodi ferry, model scale

Table A.8: Background domain mesh, default controls.

Base Size	0.0905096679918781 m
Target Surface Size	100% of Base Size
Minimum Cell Size	100% of Base Size
Number of Prism Layers	1
Prism Layers Stretching	1.3
Prism Layer Total Thickness	0.0011195253130712585 m
Default/Surface Growth Rate	2 Growth Layers
Maximum Cell Size	100% of Base Size

Table A.9: Blades mesh, default controls.

Base Size	0.0028284271247461905 m
Target Surface Size	100% of Base Size
Minimum Cell Size	100% of Base Size
Number of Prism Layers	1
Prism Layers Stretching	1.3
Prism Layer Total Thickness	8.025984222314245E-4 m
Default/Surface Growth Rate	2 Growth Layers
Maximum Cell Size	100% of Base Size

Table A.10: Number of cells, faces and vertices for blades meshes.

Domain	Cells	Faces	Vertices
Blade 1	170 174	515 168	199 059
Blade 2	170 174	515 168	199 059
Blade 3	170 174	515 168	199 059
Blade 4	170 174	515 168	199 059
Blade 5	170 174	515 168	199 059

Table A.11: Number of cells, faces and vertices for the background meshes of each case.

Case	Cells	Faces	Vertices
No restrictions	11 360 202	34 135 030	11 677 268
$x_{qu} = 6D_L$, $h_p = 0.9D_L$	4 949 687	14 796 693	5 304 209
$x_{qu} = 8D_L$, $h_p = 0.9D_L$	7 133 862	21 308 716	7 589 808
$x_{qu} = 11D_L$, $h_p = 0.9D_L$	10 397 119	31 062 406	10 946 830
$x_{qu} = 6D_L$, $h_p = 1.8D_L$	7 318 857	21 914 982	7 769 844
$x_{qu} = 6D_L$, $h_p = 2.7D_L$	9 765 344	29 268 414	10 258 572

Table A.12: Meshing parameters of the domain.

Part	Surface Remeshing	Prism Layer	Minimum Surface Size
Domain: Top Surface	`Disabled`	`Disabled`	100 %
Domain: Side Surfaces	`Disabled`	`Disabled`	100 %
Domain: Inlet Surface	`Disabled`	`Disabled`	100 %

Table A.13: Meshing parameters refinements (background): mesh control on a surface.

Part	Surface Remeshing: Target Surface Size	Prism Layer Total Thickness	Minimum Surface Size
Quay Wall	6.25 %	0.0038561524 m	6.25 %
Seabed	6.25 %	0.0038561524 m	6.25 %
Ship: Hull Side	12.5 %	`Default`	12.5 %
Ship: Hull Bottom	12.5 %	`Default`	12.5 %
Ship: Bow	1.5625 %	`Disabled`	0.78125 %
Ship: Skeg Bottom	3.125 %	`Default`	1.5625 %
Ship: Skeg Front	1.5625 %	`Default`	0.78125 %
Ship: Skeg Sides	3.125 %	`Default`	1.5625 %

Table A.14: Meshing parameters refinements (background): mesh control inside a closed volume.

Part	Trimmer: Customize Isotropic Size
Rotor Casing Vicinity	3.125 %
Wake Refinement	3.125 %

Table A.15: Meshing parameters refinements (blades): mesh control on a surface.

Part	Surface Remeshing: Target Surface Size	Prism Layer Total Thickness	Minimum Surface Size
Blade	25 %	`Default`	25 %
Area around the top of the blade	`Default` %	`Default`	`Default` %
Area around the top of the blade with prism layers	3200%	1.11952531E-3 m	3200%
Interface Casing Rotor-Blades	100 %	`Disabled`	100 %

Table A.16: Meshing parameters refinements (blades): mesh control inside a closed volume.

Part	Trimmer: Customize Isotropic Size	Prism Layer Total Thickness
Blade: Leading Edge	12.5 %	8.0259842E-4 m
Blade: Tip	12.5 %	8.0259842E-4 m
Blade: Trailing Edge	12.5 %	8.0259842E-4 m

A.1.3 Wittow ferry, model scale

Table A.17: Background domain mesh, default controls.

Base Size	0.04525483399593905 m
Target Surface Size	100% of Base Size
Minimum Cell Size	100% of Base Size
Number of Prism Layers	1
Prism Layers Stretching	1.3
Prism Layer Total Thickness	0.0010493510834392137 m
Default/Surface Growth Rate	2 Growth Layers
Maximum Cell Size	100% of Base Size

Table A.18: Blades mesh, default controls.

Base Size	0.0014142135623730952 m
Target Surface Size	100% of Base Size
Minimum Surface Size	100% of Base Size
Number of Prism Layers	1
Prism Layers Stretching	1.3
Prism Layer Total Thickness	7.58689639663757E-4 m
Default/Surface Growth Rate	2 Growth Layers
Maximum Cell Size	100% of Base Size

Table A.19: Surface wrapper, default controls.

Base Size	0.01 m
Target Surface Size	100% of Base Size
Minimum Surface Size	10% of Base Size
Volume of Interest	Largest Internal
Smallest Disconnected Surface	Number of Faces: 1000
Feature Angle	30.0

Table A.20: Number of cells, faces and vertices for blades meshes.

Domain	Cells	Faces	Vertices
Blade 1	260 342	786 478	302 738
Blade 2	260 342	786 478	302 738
Blade 3	260 342	786 478	302 738
Blade 4	260 342	786 478	302 738
Blade 5	260 342	786 478	302 738

Table A.21: Number of cells, faces and vertices for the background meshes of each case.

Case	Cells	Faces	Vertices
No restrictions	8 685 500	26 123 768	9 155 340
$x_{qu} = 6D_W$, $h_p = 0.9D_W$	6 977 440	20 819 232	7 549 054
$x_{qu} = 8D_W$, $h_p = 0.9D_W$	10 117 867	30 207 904	10 785 697
$x_{qu} = 11D_W$, $h_p = 0.9D_W$	14 877 495	44 435 949	15 688 863
$x_{qu} = 6D_W$, $h_p = 1.8D_W$	10 328 499	30 915 226	10 986 527
$x_{qu} = 6D_W$, $h_p = 2.7D_W$	13 689 728	41 017 179	14 406 992

Table A.22: Meshing parameters of the domain.

Part	Surface Remeshing	Prism Layer	Minimum Surface Size
Domain: Top Surface	`Disabled`	`Disabled`	100 %
Domain: Side Surfaces	`Disabled`	`Disabled`	100 %
Domain: Inlet Surface	`Disabled`	`Disabled`	100 %

Table A.23: Meshing parameters refinements (background): mesh control on a surface.

Part	Surface Remeshing: Target Surface Size	Prism Layer Total Thickness	Minimum Surface Size
Quay Wall	6.25 %	0.003656880231348557 m	6.25 %
Seabed	6.25 %	0.003656880231348557 m	6.25 %
Ship: Hull Side	12.5 %	`Default`	12.5 %
Ship: Hull Bottom	12.5 %	`Default`	12.5 %
Ship: Hull Mid Bottom	100 %	`Default`	100 %
Ship: Skeg Bottom	3.125 %	`Default`	1.5625 %
Ship: Skeg Sides	3.125 %	`Default`	1.5625 %

Table A.24: Meshing parameters refinements (background): mesh control inside a closed volume.

Part	Trimmer: Customize Isotropic Size
Rotor Casing Vicinity	3.125 %
Wake Refinement	3.125 %

Table A.25: Meshing parameters refinements (blades): mesh control on a surface.

Part	Surface Remeshing: Target Surface Size	Prism Layer Total Thickness	Minimum Surface Size
Blade	25 %	`Default`	25 %
Area around the top of the blade	`Default`	`Default`	`Default`
Area around the top of the blade with prism layers	3200 %	0.0010493510834392137 m	3200 %
Interface Casing Rotor-Blades	100 %	`Disabled`	100 %

Table A.26: Meshing parameters refinements (blades): mesh control inside a closed volume.

Part	Trimmer: Customize Isotropic Size	Prism Layer Total Thickness
Blade: Leading Edge	12.5 %	7.586896E-4 m
Blade: Tip	12.5 %	7.586896E-4 m
Blade: Trailing Edge	12.5 %	7.586896E-4 m

A.2 Physical models

Table A.27: Models used.

- All y+ Wall Treatment
- Detached Eddy Simulation
- Gravity
- Liquid (H2O)
- Turbulence Model: SST (Menter) k - ω
- Three Dimensional
- Constant Density
- Gradients
- Implicit Unsteady
- Segregated Flow
- Solution Interpolation
- Turbulent

Appendix B

Results

B.1 Scaled Model

B.1.1 Lodi

Velocity

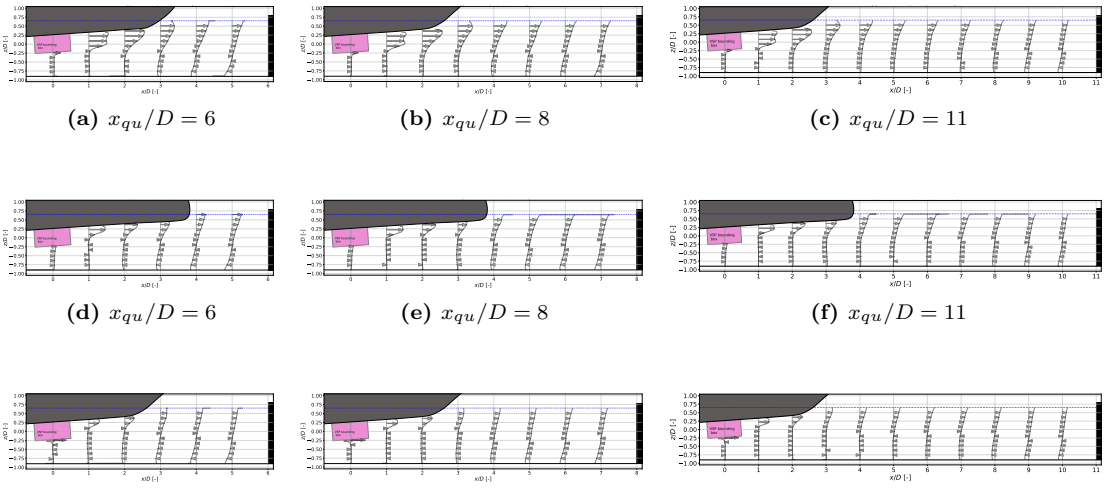

(a) $x_{qu}/D = 6$ **(b)** $x_{qu}/D = 8$ **(c)** $x_{qu}/D = 11$

(d) $x_{qu}/D = 6$ **(e)** $x_{qu}/D = 8$ **(f)** $x_{qu}/D = 11$

(g) $x_{qu}/D = 6$ **(h)** $x_{qu}/D = 8$ **(i)** $x_{qu}/D = 11$

Figure B.1: Velocity profiles of the mean longitudinal velocity for multiple x_{qu}/D positions. The top row corresponds to the section $y/D = -0.5$, the middle one to $y/D = 0$ and the bottom one to $y/D = 0.5$.

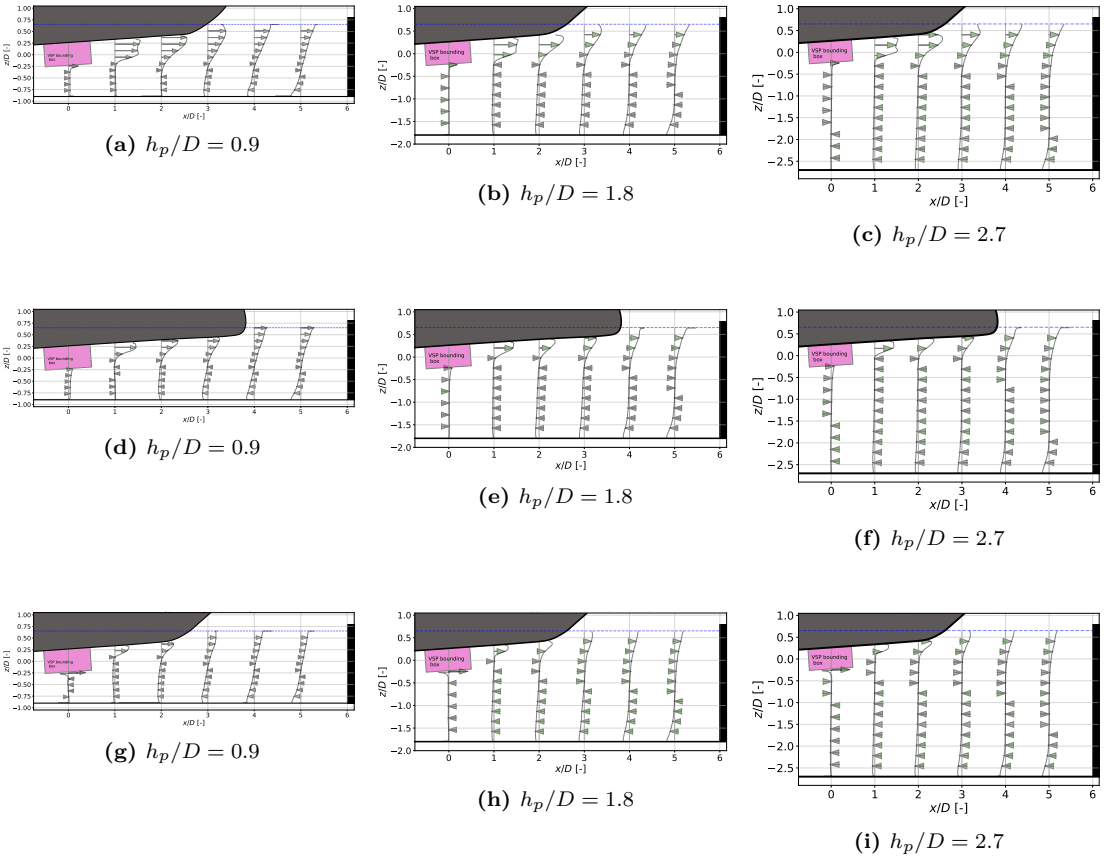

(a) $h_p/D = 0.9$ **(b)** $h_p/D = 1.8$ **(c)** $h_p/D = 2.7$

(d) $h_p/D = 0.9$ **(e)** $h_p/D = 1.8$ **(f)** $h_p/D = 2.7$

(g) $h_p/D = 0.9$ **(h)** $h_p/D = 1.8$ **(i)** $h_p/D = 2.7$

Figure B.2: Velocity profiles of the mean longitudinal velocity for multiple h_p/D positions. The top row corresponds to the section $y/D = -0.5$, the middle one to $y/D = 0$ and the bottom one to $y/D = 0.5$.

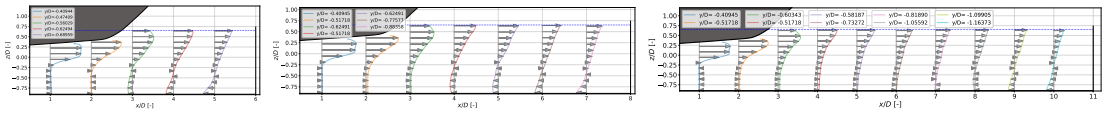

(a) $x_{qu}/D = 6$ **(b)** $x_{qu}/D = 8$ **(c)** $x_{qu}/D = 11$

Figure B.3: Velocity profiles of the mean longitudinal velocity for the cases with $h_p/D = 0.9$ and different x_{qu}/D.

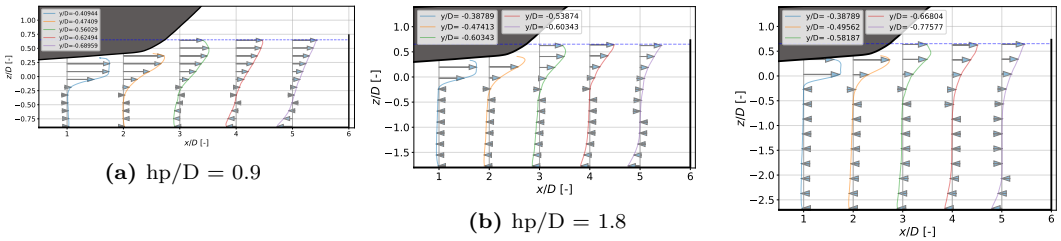

(a) hp/D = 0.9

(b) hp/D = 1.8

(c) hp/D = 2.7

Figure B.4: Velocity profiles of the mean longitudinal velocity for the cases with $x_{qu}/D = 6$ and different h_p/D.

Unrestricted case, section $y/D = 0$

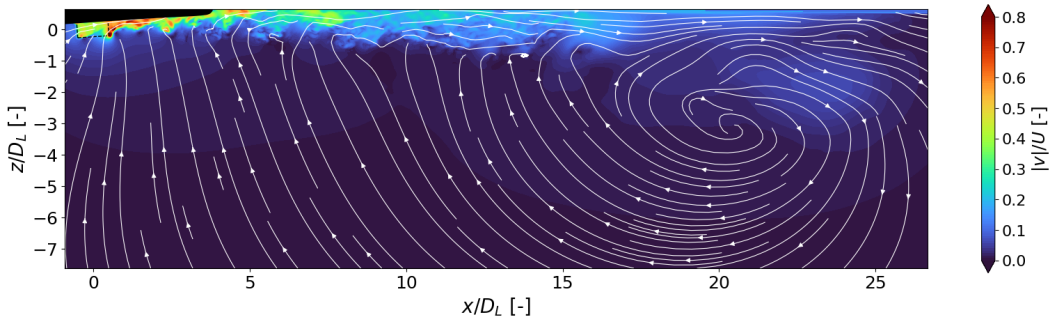

(a) Instantaneous absolute velocity $|v|$ at the last time step

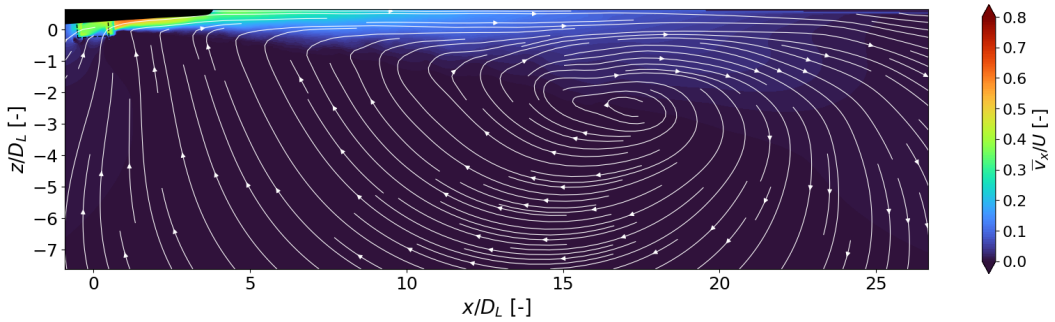

(b) Time mean longitudinal velocity $\bar{v}_x$

Figure B.5: Velocity distribution for the section $y/D = 0$ of the unrestricted case.

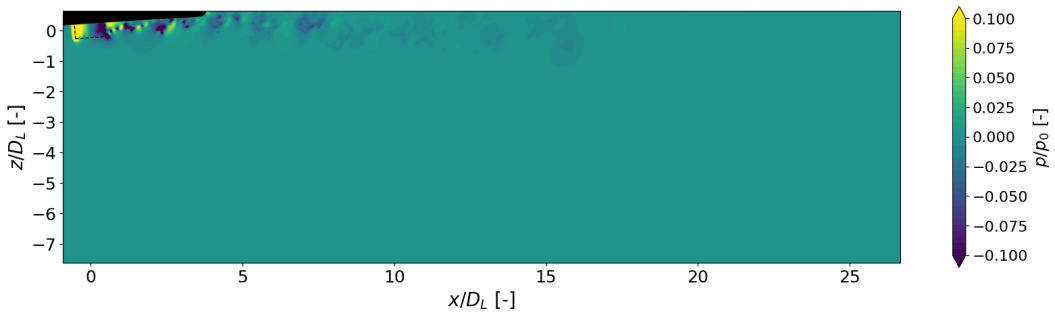

(a) Instantaneous pressure p at the last time step

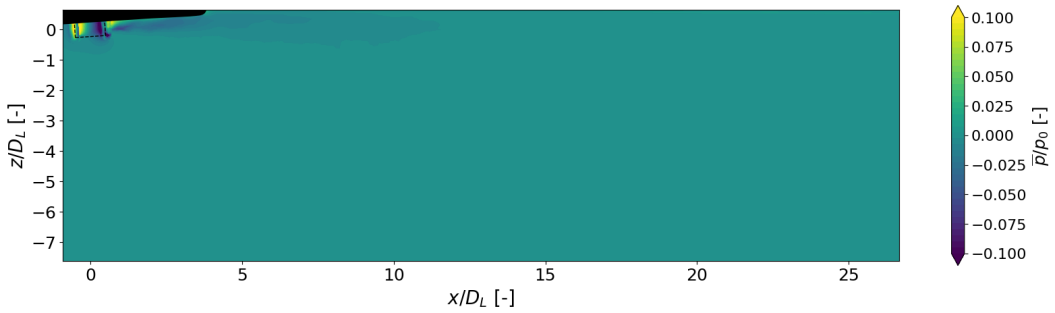

(b) Time mean pressure $\bar{p}$

Figure B.6: Pressure distribution for the section $y/D = 0$ of the unrestricted case.

B.1.2 Wittow

Velocity

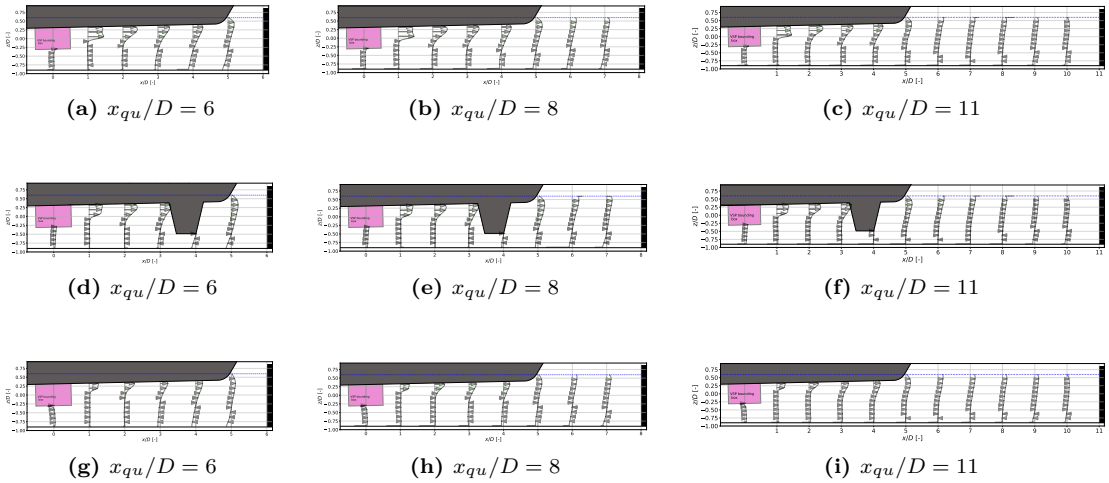

(a) $x_{qu}/D = 6$ **(b)** $x_{qu}/D = 8$ **(c)** $x_{qu}/D = 11$

(d) $x_{qu}/D = 6$ **(e)** $x_{qu}/D = 8$ **(f)** $x_{qu}/D = 11$

(g) $x_{qu}/D = 6$ **(h)** $x_{qu}/D = 8$ **(i)** $x_{qu}/D = 11$

Figure B.7: Velocity profiles of the mean longitudinal velocity for multiple x_{qu}/D positions. The top row corresponds to the section $y/D = 0.5$, the middle one to $y/D = 0$ and the bottom one to $y/D = 0.5$.

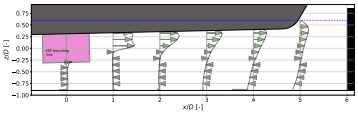

(a) $h_p/D = 0.9$

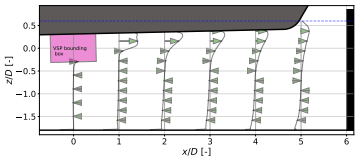

(b) $h_p/D = 1.8$

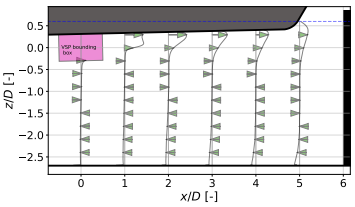

(c) $h_p/D = 2.7$

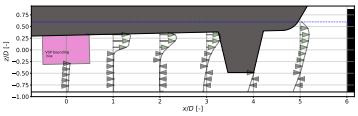

(d) $h_p/D = 0.9$

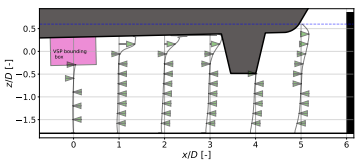

(e) $h_p/D = 1.8$

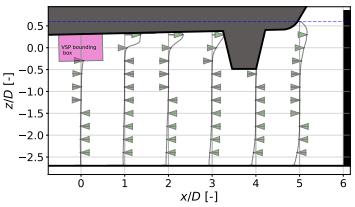

(f) $h_p/D = 2.7$

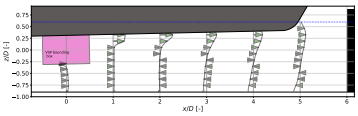

(g) $h_p/D = 0.9$

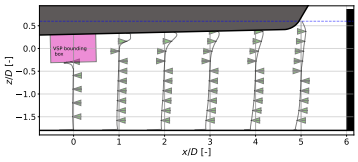

(h) $h_p/D = 1.8$

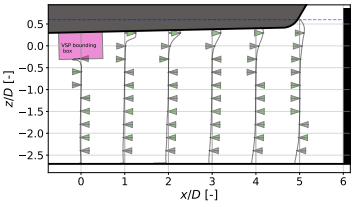

(i) $h_p/D = 2.7$

Figure B.8: Velocity profiles of the mean longitudinal velocity for multiple h_p/D positions. The top row corresponds to the section $y/D = 0.5$, the middle one to $y/D = 0$ and the bottom one to $y/D = 0.5$.

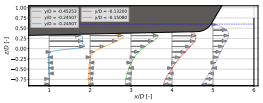

(a) $x_{qu}/D = 6$

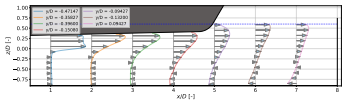

(b) $x_{qu}/D = 8$

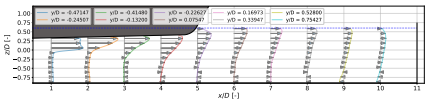

(c) $x_{qu}/D = 11$

Figure B.9: Velocity profiles of the mean longitudinal velocity for the cases with $h_p/D = 0.9$ and different x_{qu}/D.

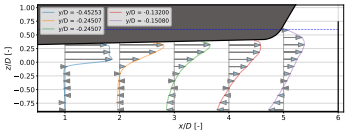

(a) $h_p/D = 0.9$

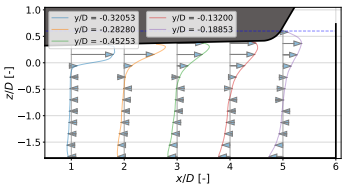

(b) $h_p/D = 1.8$

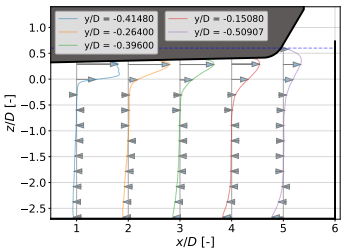

(c) $h_p/D = 2.7$

Figure B.10: Velocity profiles of the mean longitudinal velocity for the cases with $x_{qu}/D = 6$ and different h_p/D.

Unrestricted case, section $y/D = 0$

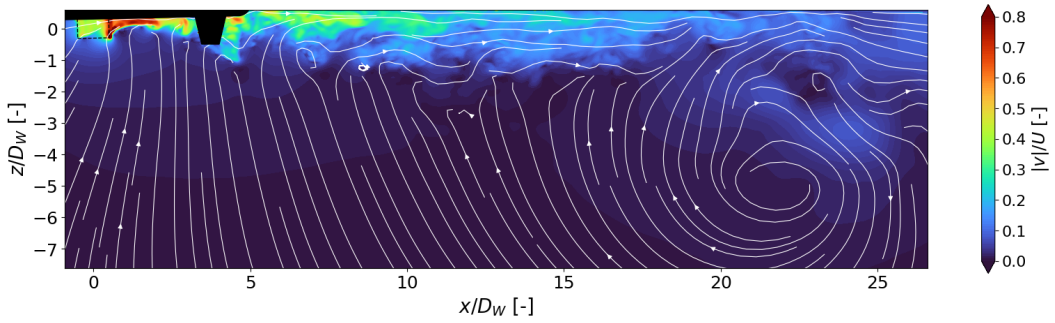

(a) Instantaneous absolute velocity $|v|$ at the last time step

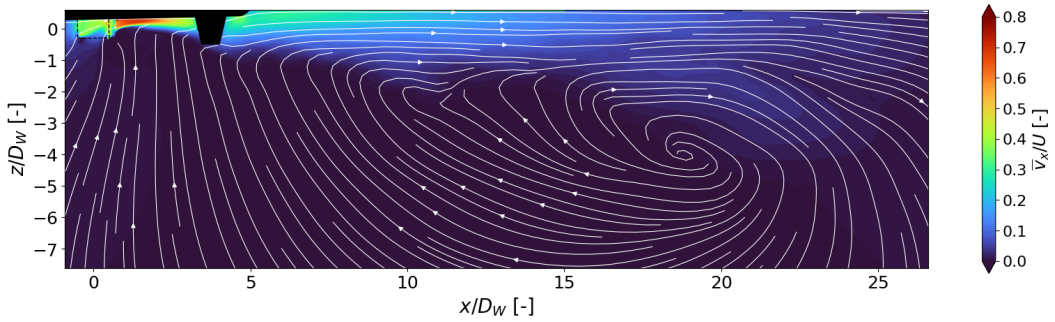

(b) Time mean longitudinal velocity $\bar{v}_x$

Figure B.11: Velocity distribution for the section $y/D = 0$ of the unrestricted case.

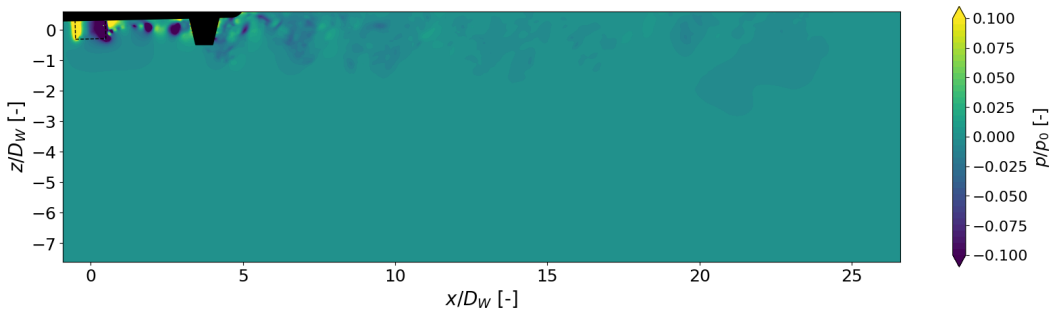

(a) Instantaneous pressure p at the last time step

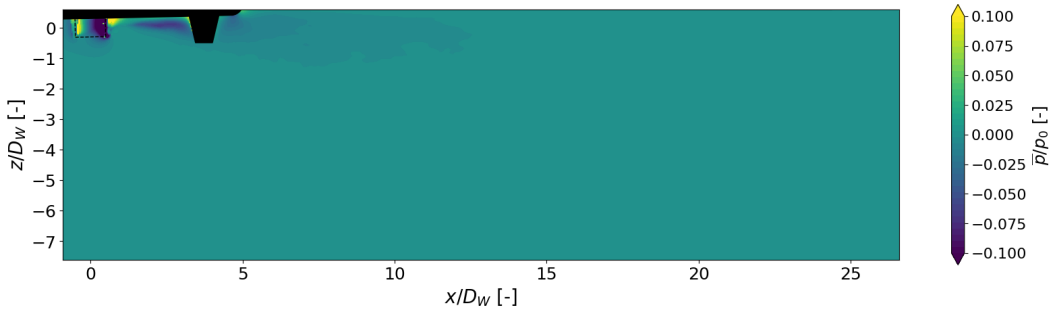

(b) Time mean pressure $\bar{p}$

Figure B.12: Pressure distribution for the section $y/D = 0$ of the unrestricted case.

B.2 Full Scale

Velocity

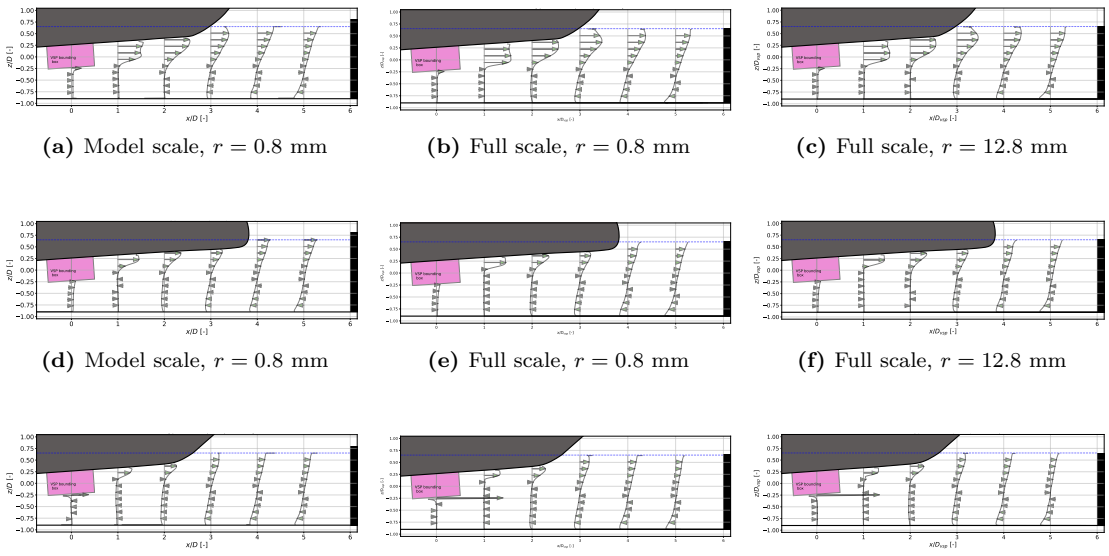

(a) Model scale, $r = 0.8$ mm **(b)** Full scale, $r = 0.8$ mm **(c)** Full scale, $r = 12.8$ mm

(d) Model scale, $r = 0.8$ mm **(e)** Full scale, $r = 0.8$ mm **(f)** Full scale, $r = 12.8$ mm

(g) Model scale, $r = 0.8$ mm **(h)** Full scale, $r = 0.8$ mm **(i)** Full scale, $r = 12.8$ mm

Figure B.13: Velocity profiles of the mean longitudinal velocity. The top row corresponds to the section $y/D = 0.5$, the middle one to $y/D = 0$ and the bottom one to $y/D = 0.5$.

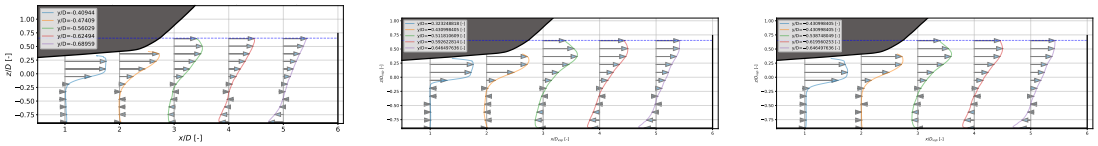

(a) Model scale, $r = 0.8$ mm **(b)** Full scale, $r = 0.8$ mm **(c)** Full scale, $r = 12.8$ mm

Figure B.14: Velocity profiles of the mean longitudinal velocity for different r.

Bibliography

[1] S. Dalley and J. P. Oleson, «Sennacherib, archimedes, and the water screw: The context of invention in the ancient world», *Technology and culture*, vol. 44, no. 1, pp. 1–26, 2003 (cit. on p. 1).

[2] J. Bourne. «A treatise on the screw propeller: With various suggestions of improvement». Naval Marine Archive, accessed 8 March 2026. [Online]. Available: `https://navalmarinearchive.com/research/docs/bourne_treatise_screw_propeller.html` (cit. on p. 2).

[3] J. Bourne, *A Treatise on the Screw Propeller: With Various Suggestions of Improvement*. Longman, Brown, Green, and Longmans, 1855 (cit. on p. 2).

[4] J. Carlton, *Marine propellers and propulsion*. Butterworth-Heinemann, 2018 (cit. on p. 2).

[5] E. C. Smith, *A short history of naval and marine engineering*. Cambridge University Press, 2013 (cit. on p. 2).

[6] G. Farr, *The Steamship Great Britain*. Bristol Historical Association, 1965 (cit. on p. 2).

[7] M. Kirmizi, «Modeling and analysis of an in-line pump jet thruster for swimming robots», Ph.D. dissertation, 2015 (cit. on p. 3).

[8] K. Propeller, «A smart way of using a controllable pitch propeller», *Retrieved from Kanome's website https://www. kamome-propeller. co. jp/en/brochures/pdf/kamome _smart_way_cpp_eng. pdf*, vol. 20, 2019 (cit. on p. 3).

[9] PIANC, «Guidelines for protecting berthing structures from scour caused by ships», *Marcom Rep. 180*, 2015 (cit. on pp. 3, 4, 8).

[10] Brunvoll AS. «Azimuth thruster with push ducted propellers», Brunvoll. [Online]. Available: `https://www.brunvoll.no/products/azimuth-push-ducted-propulsion-system` (cit. on p. 3).

[11] Kongsberg Maritime. «Contaz azimuthing thruster», Kongsberg Maritime. [Online]. Available: `https://www.kongsberg.com/maritime/products/propulsors-and-propulsion-systems/thrusters/contaz-azimuthing-thruster/` (cit. on p. 4).

[12] P. Cao, R. Yue, J. Zhang, X. Liu, G. Wu, and R. Zhu, «Proper orthogonal decomposition based response analysis of inlet distortion on a waterjet pump», *Water*, vol. 16, no. 9, p. 1282, 2024 (cit. on p. 4).

[13] A. Halder, C. Walther, and M. Benedict, «Unsteady hydrodynamic modeling of a cycloidal propeller», in *Fifth International Symposium on Marine Propulsion Smp*, vol. 17, 2017 (cit. on p. 4).

[14] G. Fasse, M. Sacher, F. Hauville, J.-A. Astolfi, and G. Germain, «Multi-objective optimization of cycloidal blade-controlled propeller: An experimental approach», *Ocean Engineering*, vol. 299, p. 117 363, 2024 (cit. on p. 3).

[15] M. Altosole, S. Donnarumma, V. Spagnolo, and S. Vignolo, «Performance simulation of marine cycloidal propellers: A both theoretical and heuristic approach», *Journal of Marine Science and Engineering*, vol. 10, no. 4, p. 505, 2022 (cit. on p. 4).

[16] M. Altosole, S. Donnarumma, V. Spagnolo, and S. Vignolo, «Marine cycloidal propulsion modelling for dp applications», in *MARINE VI: proceedings of the VI International Conference on Computational Methods in Marine Engineering*, CIMNE, 2017, pp. 206–219 (cit. on p. 4).

[17] M. Bakhtiari and H. Ghassemi, «A 2.5 d numerical study on open water hydrodynamic performance of a voith-schneider propeller», *Mechanics & Industry*, vol. 20, no. 6, p. 617, 2019 (cit. on p. 4).

[18] K. F. J. Kirsten, 1922 (cit. on p. 4).

[19] E. L. Schneider, «Blade wheel», 1928 (cit. on p. 4).

[20] Voith GmbH & Co. KGaA. «Ernst schneider: The inventor of the voith schneider propeller». [Online]. Available: `https://www.voith.com/corp-en/ernst-schneider.html` (cit. on p. 4).

[21] *Precise and safe maneuvering: Voith schneider propeller* (cit. on pp. 5–7).

[22] Popular Mechanics, «Sea-going eggbeater», *Popular Mechanics*, Mar. 1950, March issue (cit. on p. 5).

[23] V. Spagnolo, «A cycloidal propeller simulation model and its application to low and high speed ship manoeuvres», 2019 (cit. on p. 5).

[24] E. Esmailian, H. Ghassemi, and S. A. Heidari, «Numerical investigation of the performance of voith schneider propulsion», *American Journal of Marine Science*, vol. 2, no. 3, pp. 58–62, 2014 (cit. on pp. 5–7).

[25] *Types and dimensions: Voith schneider propeller* (cit. on p. 5).

[26] *Voith schneider propeller: Designer manual* (cit. on pp. 5, 6).

[27] Q. Li, Y. Hu, F. Wang, and X. Cao, «Numerical simulation of cycloidal propeller performance based on cfd», in *International Conference on Mechanical Design and Simulation*, Springer, 2024, pp. 617–629 (cit. on p. 6).

[28] A. Guarnieri, S. Saremi, A. Pedroncini, J. H. Jensen, S. Torretta, M. Vaccari, and C. Vincenzi, «Effects of marine traffic on sediment erosion and accumulation in ports: A new model-based methodology», *Ocean Science*, vol. 17, no. 2, pp. 411–430, 2021 (cit. on p. 7).

[29] D. Ryan and G. Hamill, «Determining propeller erosion at the stern of a berthing ship», *Journal of waterway, port, coastal, and ocean engineering*, vol. 139, no. 4, pp. 247–255, 2013 (cit. on p. 7).

[30] Y. Yuksel, R. I. Tan, and Y. Celikoglu, «Determining propeller scour near a quay wall», *Ocean Engineering*, vol. 188, p. 106 331, 2019 (cit. on pp. 7, 22, 54).

[31] M. Wei, Y.-M. Chiew, and N.-S. Cheng, «Recent advances in understanding propeller jet flow and its impact on scour», *Physics of Fluids*, vol. 32, no. 10, 2020 (cit. on p. 7).

[32] R. I. Tan and Y. Yüksel, «Seabed scour induced by a propeller jet», *Ocean Engineering*, vol. 160, pp. 132–142, 2018 (cit. on p. 7).

[33] D. V. (Rijkswaterstaat, «Onderzoek naar mogelijke erosie door de waterbeweging rond de dubbeldeks veerboot m.s. "molengat"», *Report Number S80.14*, 1982 (cit. on p. 8).

[34] M. D. F. M. L. Mangani, M. Darwish, et al., *The finite volume method in computational fluid dynamics*, 2016 (cit. on p. 12).

[35] Siemens Digital Industries Software, *Simcenter STAR-CCM+ documentation*, Version 2302, Siemens (cit. on pp. 12, 22, 23, 29).

[36] H. Hadzic, «Development and application of finite volume method for the computation of flows around moving bodies on unstructured, overlapping grids», Ph.D. dissertation, 2006 (cit. on pp. 12, 29).

[37] B. E. Launder and D. B. Spalding, «The numerical computation of turbulent flows», in *Numerical prediction of flow, heat transfer, turbulence and combustion*, Elsevier, 1983, pp. 96–116 (cit. on p. 15).

[38] D. C. Wilcox et al., *Turbulence modeling for CFD*. DCW industries La Canada, CA, 1998, vol. 2 (cit. on p. 16).

[39] F. R. Menter, «Two-equation eddy-viscosity turbulence models for engineering applications», *AIAA journal*, vol. 32, no. 8, pp. 1598–1605, 1994 (cit. on p. 16).

[40] J. Foale, «Simulating extinction and blow-off in kerosene swirl spray flames», Ph.D. dissertation, Oct. 2021. DOI: 10.17863/CAM.82714 (cit. on p. 17).

[41] Stadtwerke Konstanz. «Die flotte der fähre konstanz–meersburg». [Online]. Available: https://www.stadtwerke-konstanz.de/faehre/aktuelles/die-flotte-der-faehre-konstanz-meersburg/ (cit. on p. 19).

[42] all-in.de. «Das ist das längste schiff auf dem bodensee». [Online]. Available: https://www.all-in.de/baden-wuerttemberg/das-ist-das-laengste-schiff-auf-dem-bodensee-26-05-25-109103588 (cit. on p. 19).

[43] FRS World, *Mf "wittow"*, https://www.frs.world/de/frs-flotte/ships/motorfaehre-wittow?utm_source=chatgpt.com, Accessed: 2026-01-31, 2026 (cit. on p. 20).

[44] AroundUs, *Wittow ferry*, https://aroundus.com/p/10925718-wittow-ferry?utm_source=chatgpt.com, Accessed: 2026-01-31, 2025 (cit. on p. 20).

[45] Y. Cui, W. H. Lam, Z. C. Ong, L. Ling, C. L. Siow, D. Robinson, and G. Hamill, «Experimental scours by impinging twin-propeller jets at quay wall», *Journal of Marine Science and Engineering*, vol. 8, no. 11, p. 872, 2020 (cit. on pp. 22, 54).

[46] O. Lancaster, «Review of existing scour protection design guidelines with application to a proposed cruise terminal - what are their limitations?», Apr. 2023 (cit. on p. 22).

[47] A. Kadir, I. Istadi, A. Subagio, W. Waluyo, and A. Muis, «The ship's propeller rotation threshold for coral reef ecosystems based on sediment rate indicators: Literature review with bibliometric analysis and experiments», *Indonesian Journal of Science and Technology*, vol. 9, no. 2, pp. 355–372, 2024 (cit. on p. 22).

[48] J.-H. Hong, Y.-M. Chiew, and N.-S. Cheng, «Scour caused by a propeller jet», *Journal of Hydraulic Engineering*, vol. 139, no. 9, pp. 1003–1012, 2013 (cit. on p. 22).

[49] T. Zhao, H. Iacovides, and T. Craft, «Evaluation of reynolds-averaged navier–stokes models for simulating vortex-induced vibration in high reynolds number flow», *Physics of Fluids*, vol. 37, no. 12, 2025 (cit. on p. 25).

[50] J. Devlin, D. Chandar, and N. J. Quinlan, «Direct flux via virtual faces (dfvf-overset): Interpolation-free, conservative, overset cfd using a generalised finite volume method», *Computers & Fluids*, vol. 267, p. 106 072, 2023 (cit. on p. 26).

[51] J. H. Ferziger and M. Perić, *Computational methods for fluid dynamics*. Springer, 2002, vol. 586 (cit. on p. 29).

[52] F. M. White, *Fluid mechanics*, 1999 (cit. on p. 29).

[53] S. B. Pope, «Turbulent flows», *Measurement Science and Technology*, vol. 12, no. 11, pp. 2020–2021, 2001 (cit. on p. 29).

[54] B. R. Munson, D. F. Young, and T. H. Okiishi, «Fundamentals of fluid mechanics», *Oceanographic Literature Review*, vol. 10, no. 42, p. 831, 1995 (cit. on p. 29).

[55] M. S. Gritskevich, A. V. Garbaruk, and F. R. Menter, «Fine-tuning of ddes and iddes formulations to the k-ω shear stress transport model», *Progress in Flight Physics*, vol. 5, pp. 23–42, 2013 (cit. on p. 29).

[56] A. Quarteroni, *Numerical models for differential problems*. Springer, 2009 (cit. on p. 29).

[57] H. Versteeg and W. Malalasekera, «Computational fluid dynamics», *The finite volume method*, pp. 1–26, 1995 (cit. on p. 29).

[58] L. Davidson, «An introduction to turbulence models», Chalmers University of Technology, Gothenburg, Tech. Rep., 2022 (cit. on p. 29).

[59] H. Martinsson and J. Varosy, «Cfd simulation of the wakejet flow», 2017 (cit. on p. 29).

[60] P. A. Lakshmynarayanana, «Application of 3d-cfd modelling for dynamic behaviour of ship in waves», Ph.D. dissertation, University of Southampton, 2017 (cit. on p. 29).

[61] M. Wei and Y.-M. Chiew, «Impingement of propeller jet on a vertical quay wall», *Ocean Engineering*, vol. 183, pp. 73–86, 2019 (cit. on p. 48).

[62] A. Nazeer, N. B. Khan, E. Uddin, M. Jameel, O. Al-Abbasi, Q. Wu, A. Munir, and H. Shahid, «Hydrodynamic and hydro acoustic analysis of marine propeller in off design flow conditions», *Plos one*, vol. 20, no. 3, 2025 (cit. on p. 48).

[63] X. Feng and J. Lu, «Effects of balanced skew and biased skew on the cavitation characteristics and pressure fluctuations of the marine propeller», *Ocean Engineering*, vol. 184, pp. 184–192, 2019 (cit. on p. 48).

[64] G. Hamill, H. Johnston, and D. Stewart, «Propeller wash scour near quay walls», *Journal of waterway, port, coastal, and ocean engineering*, vol. 125, no. 4, pp. 170–175, 1999 (cit. on p. 54).